

Syracuse University

SURFACE at Syracuse University

Dissertations - ALL

SURFACE at Syracuse University

5-14-2023

Geometric confinement of thin films: From crumple formation to curvature-induced propulsion

Raj De

Syracuse University

Follow this and additional works at: <https://surface.syr.edu/etd>

Recommended Citation

De, Raj, "Geometric confinement of thin films: From crumple formation to curvature-induced propulsion" (2023). *Dissertations - ALL*. 1678.
<https://surface.syr.edu/etd/1678>

This Dissertation is brought to you for free and open access by the SURFACE at Syracuse University at SURFACE at Syracuse University. It has been accepted for inclusion in Dissertations - ALL by an authorized administrator of SURFACE at Syracuse University. For more information, please contact surface@syr.edu.

Abstract

Thin films can undergo large amplitude nonlinear deformation even under a small applied force which makes predicting their behavior rather challenging. This dissertation focuses on two phenomena in thin films: the morphological transition from sharp to smooth microstructures in geometrically-confined sheets, and a novel locomotion behavior of a thin floating film placed on an interface with a curvature gradient.

In the first portion of the thesis, we use inflated membranes as model system to understand morphological transitions in confined films. We have developed methods to make air-tight membranes out of sheets of materials with varying Young's modulus and thickness. We have observed that increasing the internal pressure in the membranes causes some sharp-edged diamond-like structures called crumples to form. On further increase in pressure, these crumples transition to smooth periodic wrinkles. We have measured this transition pressure across a wide range of materials and geometries. We collect our data, as well as data from other experiments on interfacial polymer films, in an empirical phase diagram for the transition from wrinkles to crumples. We further study the topography of the crumpling pattern on the surface of the membrane and its relation to d-cones.

Small-scale structures like wrinkles and crumples can enable macroscopic shape change of an entire sheet. In the second part of this thesis, we explore how shape changes of a film (through small-scale wrinkling) can enable a film to feel body forces when placed on a liquid with a non-uniform curvature. This study is motivated by examples from nature: arthropod species that exploit the surface tension of water for aquatic locomotion. Current literature addresses stiff or finitely bendable materials that retain their shape on liquid meniscus where the fluid adjusts its interface to accommodate them via an interplay of surface tension and buoyancy or gravity. We introduce an unexplored setting where thin monotonous film that can easily deform by capillary forces is placed on a positively curved liquid meniscus. A thin film can conform to a curved meniscus by forming small-amplitude wrinkles. Once released, it sets in motion towards the flat center while returning to its symmetrical state. We are able

to identify the complex mechanics of propulsion experienced by thin film through numerical simulations using Surface Evolver. Our results give a closer look at the velocity of thin film and energetics of the system and its dependence on the position of the sheet on the interface. Our finding curiously shows that an unstretchable film progresses 10 times faster than the same film with finite stretching indicating the importance of elasticity in such systems.

Geometric confinement of thin films: From crumple formation to curvature-induced propulsion

by Raj De

B.Sc., University of Calcutta, 2014

M.S., Indian Institute of Technology (ISM), 2016

Dissertation

Submitted in partial fulfillment of the requirements for the degree of
Doctor of Philosophy in Physics.

Syracuse University

May 2023

Copyright ©Raj De 2023

All Rights Reserved

Acknowledgments

I remember when I first walked in the lab with Joey, he asked me if I thought blowing balloons for research sounds fun. And my immediate response was “YES”! I am grateful for the opportunity to work under his guidance, helping me not only understand intricate science at ease but also helping me hone my soft skills with asking the right questions in research. He struck a perfect balance between guidance along with autonomy in research that showed his care for my holistic development.

I will also take this opportunity to thank all my committee members Teng Zhang, G. Scott Watson, Jennifer Ross, Jennifer Schwartz and Chris Santangelo who took time out of their busy schedules to review my dissertation work.

I have been grateful to have worked alongside some amazing researchers who have motivated me to work harder and inspired me about new research. I have to thank my collaborators and lab mates Monica Ripp, Menfei Hei, Yousra Timonay, Pan Dong, Jikai Wang, Zachariah Schrechegost, Seif Heijazine, Emily Veru, Jessica Stelzel and many others for stimulating conversations and promoting a harmonious lab setting. I will also thank the physics main office staff - Yudy, Patty, Cassandra, Kristine and many others that has always been kind and helpful and made all the paperwork hassle free.

I have been blessed with some wonderful people in my life that have made this work much easier to complete. I definitely looked forward to the dinner drop-offs from my partner Michael who made sure that I didn't get “hangry” when I worked late hours in the lab. I am grateful for his constant support and lending sympathetic ears to all my research problems. I have an amazing group of friends Asad, Anand, Deepjyoti, Preeti, Sarthak, Sumon and many others in Syracuse who made my life outside school fun.

I can't imagine doing this without the constant support of my mom and dad who always believed in me and even 1000 miles between us didn't deter them showing me their love and care every day. Finally, my brother who have always been my mentor giving me the “technical” advices along with a dose of brotherly love that have guided my academic path.

Contents

| | | |
|----------|---|-----------|
| 1 | Introduction | 1 |
| 1.0.1 | What is "Wrinkling"? | 2 |
| 1.0.2 | From smooth wrinkles to sharp "crumples" | 4 |
| 1.1 | Interfacial films | 8 |
| 1.1.1 | Capillarity | 8 |
| 1.1.2 | Sheet on Drop | 9 |
| 1.1.3 | Computational approach to curvature-induced propulsion: | 12 |
| 2 | Stress focusing in inflated membranes | 12 |
| 2.1 | Popular Summary | 13 |
| 2.2 | Introduction | 13 |
| 2.3 | Experimental Systems | 15 |
| 2.4 | Experimental setup | 18 |
| 2.4.1 | Preliminary setup | 18 |
| 2.4.2 | Pressure gauge | 19 |
| 2.4.3 | Final Setup | 20 |
| 2.4.4 | Tensile Testing | 21 |
| 2.4.5 | Membrane Construction | 22 |
| 2.4.6 | 3D Scanner Setup | 24 |
| 2.5 | Theory | 25 |
| 2.5.1 | Föppl-von Kármán equations | 25 |
| 2.5.2 | Sheet on drop case | 28 |
| 2.6 | Parameterization | 30 |
| 2.7 | Measurement and analysis | 31 |
| 2.8 | Results | 32 |

| | | |
|----------|---|-----------|
| 2.8.1 | Crumple Threshold | 32 |
| 2.8.2 | Pressure Threshold | 35 |
| 2.8.3 | Crumple Morphology | 37 |
| 2.9 | Discussion | 40 |
| 3 | Curvature Driven Propulsion of Thin Floating Films | 44 |
| 3.1 | Popular summary | 44 |
| 3.2 | Introduction | 45 |
| 3.3 | Phenomenology from experiment | 47 |
| 3.4 | Concept of theoretical model | 47 |
| 3.5 | Simulation | 48 |
| 3.6 | Energy measurements | 50 |
| 3.6.1 | Drag model | 51 |
| 3.7 | Comparison to experiment | 52 |
| 3.7.1 | Non-Dimensionalization | 52 |
| 3.7.2 | Inextensible limit | 54 |
| 3.7.3 | Finite stretching in films | 55 |
| 3.8 | Measuring the energy scalings | 59 |
| 3.9 | Stretchable vs Unstretchable films on liquid meniscus | 59 |
| 3.9.1 | Energy scaling | 60 |
| 3.9.2 | Stretchable film | 63 |
| 4 | Conclusion | 64 |
| 4.1 | Summary | 64 |
| 4.2 | Future Directions | 66 |
| 4.2.1 | Behavior of d-cones under tensile stresses | 66 |
| 4.2.2 | Universal energy scaling for film on meniscus | 70 |

| | | |
|----------|---|-----------|
| A | Membranes: Fabrications and troubleshooting | 71 |
| A.1 | Varying Shape of the membrane | 71 |
| A.1.1 | Square and Rectangle | 71 |
| A.1.2 | Triangular | 73 |
| A.1.3 | Empanada | 73 |
| A.1.4 | Tetrahedral | 73 |
| A.2 | Preparation of the openings in the membrane | 74 |
| A.3 | Troubleshooting | 75 |
| A.4 | Inflating membrane | 75 |
| A.5 | Measuring Thickness | 76 |
| A.6 | Measuring Young’s Modulus | 76 |
| A.7 | Lighting | 76 |
| A.8 | Camera and Image Analysis | 77 |
| B | A Guide to the 3D Scanning and analysis | 78 |
| B.1 | Data Cleanup and extraction | 79 |
| B.2 | Data Analysis | 79 |
| C | Surface Evolver | 80 |
| C.1 | Wrinkling | 80 |
| C.2 | Choice of Poisson’s ratio | 80 |
| C.3 | Gradient Descent | 81 |
| C.4 | Adding Gravity | 82 |
| C.5 | The Ansatz Problem and Volume iteration (Voliter) | 83 |
| C.6 | Height profile study and comparison with the experiment | 84 |
| D | Curriculum Vitae | 93 |

List of Figures

| | | |
|---|---|----|
| 1 | Pattern formation in thin films (a) Gyrification in a mechanical model of a brain [2]. (b) Wrinkle patterns in deployable weather balloons [3]. (c) A partly bitten off apple left for a day starts wrinkling around the bitten off edge. [4] (d) A crumpled graphene film.[5] | 1 |
| 2 | Wrinkling in various systems (a) Wrinkling occurs in nature in many instances like the ones seen in Shar Pei dogs. [8] (b) Scanning Electron Microscope of wrinkled graphene, compared with wrinkle patterns on a curtain [9]. | 3 |
| 3 | Crumpling in various systems (a) Crumples form on Candy wrappers by twisting a flat sheet around the candy. (b) Crumpling in stainless steel wine tank caused by earthquake. [12] | 5 |
| 4 | Developable cone: An isolated sharp point on a crushed paper can be thought of as a d-cone, constructed by indenting the center of a circular sheet resting on a hoop. | 6 |
| 5 | Cheerios effect: Floating soap bubbles on water tend to clump around the rim of the dish. | 9 |
| 6 | Partly submerged spherical object: The shaded area represents weight of the displaced liquid equivalent to the buoyant force on the object [18]. . . | 10 |

| | | |
|----|---|----|
| 7 | <p>The crumple-to-wrinkle transition is seen in various geometries, boundary conditions, and system sizes. The top row of this figure shows schematics of each setup considered in this study with the Gaussian curvature in the area relevant to the transition marked underneath each schematic. (a) An intrinsically flat circular PS sheet ($E=3.4$ GPa) of with radius $W = 1.5$mm and thickness $t = 77$ nm on a liquid meniscus forms crumples when the droplet is highly curved. (b) a PS sheet floating on a liquid bath forms crumples when indented past a certain threshold depth. This image shows a film with $W = 11$ mm and $t = 436$ nm. (c) The central portion of a rectangular PS sheet with $t = 157$ nm, width $W = 3.3$ mm, and length 9.7 mm on a cylindrical water meniscus compressed uniaxially between two barriers. Wrinkles form whe the curvature is low and crumples form when the curvature is increased along the wrinkles.(d) A square polyethylene bag ($t = 102 \mu\text{m}$, $E = 210$ MPa) forms wrinkles at high internal pressure, P. Crumples appear at lower pressure. The bag is $W = 20$ cm wide when deflated. [19]</p> | 16 |
| 8 | <p>Schematic graph showing the preliminary setup for performing the experiment.</p> | 18 |
| 9 | <p>Pressure gauge calibration: (a) Measuring the pressure through pressure gauge and manometer simultaneously. (b) Graph comparing the pressure data obtained from manometer and the pressure gauge. Schematic graph comparing the pressure data obtained from manometer and the pressure gauge.</p> | 19 |
| 10 | <p>Inflating membrane experiment is recorded using DSLR camera with the corresponding pressure measured using pressure gauge</p> | 20 |
| 11 | <p>Thin film mounted between the clamps of the tensile testing instrument.</p> | 21 |

| | | |
|----|--|----|
| 12 | Determining Young's Modulus: The stress over strain graph for LDPE sheets of 0.006" thick. Multiple film strips were measured for its two orientation. The region between the red lines is used to determine the Young's Modulus of the material. | 22 |
| 13 | (a)Heat impulse sealer. (b)Heat impulse sealer with a heat sealed LDPE membrane. | 24 |
| 14 | Natural rubber square membrane of 0.006" thickness. | 24 |
| 15 | Scanning setup for studying the topography of the membranes. | 25 |
| 16 | Planar axisymmetric stretching of a circular sheet. | 26 |
| 17 | Schematic of a wrinkled rectangular patch, showing σ_{\parallel} and R_{\parallel} . Their values and the total length of the buckled region, l_{\parallel} , are quantified in Table 2 for each setup. | 30 |
| 18 | Schematic diagram for chord. [54] | 32 |
| 19 | Measuring R_{\parallel}: (a)Stencils cut out of stiff board for various radius of curvature. (b)Measurement of radius of curvature using stencils. | 33 |
| 20 | The membrane is inflated gradually. We first observe sharp crumples on the surface followed by transition to smooth wrinkles at a certain pressure. . . . | 33 |

21 **Phase diagram for wrinkles and crumples.** (a) Crumpling threshold measured in the four experimental setups in Fig. 7, including sheet-on-droplet data from King et al. [20] and indentation data from Paulsen et al. [40]. Values of $l_{\parallel}, R_{\parallel}$ and σ_{\parallel}/Y , are either measured or deduced from other measured quantities (see Table 2). The sheet thickness ranges from $40 < t < 630$ nm for the polymer films and $15 < t < 222$ μm for the inflated membranes. Indentation data have $Y = 72$ μm and W shown in the legend. Sheet-on-cylinder data have $W = 3.2$ mm and γ shown in the legend. Parameters for inflated membranes are detailed in Fig. 22(a) and 22(b). The data are reasonably well described by Eq. (28) with $\alpha = \alpha_{cr} = 155$ (dashed line). Inset: Threshold curvature $1/R_{\parallel}$ for crumpling, versus wrinkle length l_{\parallel} , in the sheet-on-cylinder setup at fixed t and γ . Dashed line: Equation (28) with $\alpha_{cr} = 155$. (b) Crumpling threshold versus bendability ϵ^{-1} . The threshold is approximately constant over a wide range of bendability. 34

| | | |
|----|---|----|
| 22 | <p>Pressure threshold for transitioning from sharp crumples to smooth wrinkles in inflated membranes: (a) Experiments using square bags of various thickness ($15 < t < 222$ m), width ($10 < W < 31$ cm), and Young's modulus ($2.0 < E < 1500$ MPa). Open symbols show the transition for decreasing pressure; the rest of the data are obtained by increasing the pressure. The data are well described by Eq. (30) with $\alpha_{cr} = 100$ (dashed line). Inset: l_{\parallel} and R_{\parallel} versus pressure for a square polyethylene bag ($W = 20$ cm, $t = 49$ μm). Both quantities are relatively constant near the threshold pressure (dashed line, P_{cr}). (b) Experiments with different bag shapes, which are shown in the insets prior to inflation. We use a variety of polyethylene ($E \sim 200$ MPa) and rubber ($E \sim 2$ MPa) sheets to vary the Young's modulus and thickness, as denoted in the legend. Here, $9.4 < W < 31$ cm. The crumpling threshold is consistent with the result for square bags, as shown by the gray squares and dashed line that are repeated from (a).</p> | 36 |
| 23 | <p>Crumple morphology: (a) Renderings of three-dimensional scans of an inflated square polyethylene bag ($t = 49$ μm, $E = 297$ MPa, $W = 20$ cm), showing the topography of wrinkles (top) and crumples (bottom). (b) Cross sections through a single buckled feature as a function of the gauge pressure. The profiles are taken along the dashed lines in (a), and the two circles highlight the sharp tips at the two ends of the crumple. (c) Cross sections along a perpendicular direction, which show only a small change in width through the transition [the same scale as (a),(b)].</p> | 37 |
| 24 | <p>Crumple topography: Local Gaussian curvature K for the scans shown in Fig. 23 (a). The wrinkled state (top) shows large positive and negative curvatures along the wrinkle crests and troughs. The crumpled state (bottom) localizes K and, hence, material stresses.</p> | 38 |

| | | |
|----|--|----|
| 25 | Emergent scales in the crumpled phase. (a) Crumple length l_{cr} , measured from optical images in the sheet-on cylinder, indentation, and inflated membrane setups. The sheet thickness and modulus are varied over a wide range by using rubber ($E \sim 2 \text{ MPa}$), polyethylene ($E \sim 200 \text{ MPa}$), and polystyrene ($E = 3.4 \text{ GPa}$) sheets. We also vary the surface tension in the sheet-on-droplet setup (open symbols, 72 mN/m ; closed symbols, 36 mN/m). The data are reasonably described by a simple expression involving l_{\parallel} , R_{\parallel} , and $\sigma_{\parallel} = Y$ [solid line, Eq. 31]. The two images show l_{cr} increasing upon compression; this behavior may account for some of the scatter in the data. Inset: l_{cr} versus R_{\parallel} , which does not collapse the data. | 41 |
| 26 | Water lily beetle can bend its body to create curvature mismatch for locomotion | 46 |
| 27 | Experimental Setup. (a) Side and top view of the experiment, where a thin film is placed on the curved meniscus of an overfilled petri dish. (b) Composite image of a time series when the film is let go. The geometric mismatch between the sheet and the meniscus propels film towards the center. | 48 |
| 28 | Coarse-grained model for wrinkling (a) A thin film forms wrinkles to adopt a doubly-curved shape. (b) We model this wrinkling in Surface Evolver using a triangular mesh where the edges may contract for free. This provides a suitable coarse-grained model of the effect of wrinkling. | 49 |
| 29 | Side and top view of floating sheet system. | 49 |
| 30 | Energy Plots: Simulation results where the sheet is positioned at a distance r from the center of the dish. The system energy is comprised of surface and gravitational energy. The inset show that the total energy has an exponential dependence on the radial position. | 50 |
| 31 | Comparing velocity derived from the inextensible film simulation with the drag law shows discrepancy with experimental results. | 55 |

| | | |
|----|---|----|
| 32 | Simulation results where the finitely stretchable sheet is positioned at a distance r from the center of the dish: The system energy is comprised of surface, gravitational and stretching energy. The inset shows the stretching energy separately to show its exponential growing trend with the radial position from center to the edge. | 56 |
| 33 | The total energy is rescaled by subtracting the total energy with the $U(0) = a + c$, $dU = U - U(0)$ | 57 |
| 34 | Comparing velocity derived from the finitely stretchable film with the drag law shows good agreement with experimental results. The inextensible film simulations are also shown for comparing how much the velocity can decrease on introducing finite stretching. | 58 |
| 35 | Figure showing height dependence | 61 |
| 36 | Height dependence on total energy | 61 |
| 37 | Data collapse across all relevant observables for this phenomenon. | 62 |
| 38 | Energy coefficients from the equation $U(r) = A \exp Br$ are plotted against the stretching modulus Y . This shows that both A and B becomes constant on reaching a threshold Y | 64 |
| 39 | Data Collapse for all observable relevant to this phenomenon. | 65 |
| 40 | Introducing the crescent radius R_c that is being measured in this system to compare its scaling with a typical d-cone. | 68 |
| 41 | Cresecent radius R_c versus Pressure P | 68 |
| 42 | Scaled cresecent radius $\frac{R_c}{D}$ versus scaled pressure $\left(\frac{PR_{\parallel}}{Et}\right) \left(\frac{\ell_{cr}}{D}\right)$ | 69 |
| 43 | Cartoon showing the rectangular membrane construction out of a sheet. The dotted lines on the membrane denotes the seals. The red line denotes the surface used for conducting our experiments (a) Rectangular and square membrane construction (b) Triangular membrane construction. | 71 |

| | | |
|----|---|----|
| 44 | Cartoon showing the empanada shaped membrane construction out of a sheet. The dotted lines on the membrane denotes the seals. The red line denotes the surface used for conducting our experiments. | 73 |
| 45 | Cartoon showing the tetrahedral shaped membrane construction out of a sheet. The dotted lines on the membrane denotes the seals. The red line denotes the surface used for conducting our experiments. | 74 |
| 46 | Tensile testing samples: (a)Prepared samples of various materials. You can notice how the sample on the left curls on itself making it difficult to mount (b) Sample is placed between glass slides to prevent creases and help in the mounting process. | 77 |
| 47 | Scanner Calibration: Cylindrical post used as a sample object for calibration along with its scanned output | 78 |
| 48 | Systematic check: Comparing gravitational energy of systems with varying sheet size. The sheet is located on the central flat portion of the liquid, so that it should not change the height profile of the liquid as we vary its radius, and the gravitational energy should not change. The results validate this check. | 82 |
| 49 | Height Profile Matching: Simulating the model with the non-dimensionalized parameters from the experiment and superimposing it on the liquid drop to test qualitative profile matching. | 84 |
| 50 | Height Profile reflection: The left side of the height profile is reflected on the right side.(a) Height profile when the film is at 1.1 from center. (b) Height profile when the film is at 2.5 from center. | 85 |

List of Tables

| | | |
|---|--|----|
| 1 | Materials used to construct membranes | 23 |
| 2 | Physical scales near the wrinkle-to-crumple transition. Expressions for the buckled length (ℓ_{\parallel}), curvature along the wrinkles (R_{\parallel}), and tensile stress along the wrinkles (σ_{\parallel}), which are pictured schematically in figure 17. Values for the sheet-on-droplet setup are based on Ref. [20]. In this setup, R_{\parallel} and σ_{\parallel} vary spatially: we show their values at the location $r = W$, where the curvature is largest. Values for the indentation are based on the height profile $\zeta(r)$ in the relevant regime where wrinkles cover the sheet. In that case, $\zeta(r) = \delta Ai(r/\ell_{curv})/Ai(0)$, where $Ai(x)$ is the Airy function and $\ell_{curv} = W^{1/3}\ell_c^{2/3}$ with $\ell_c = \sqrt{\gamma/\rho g}$ being the capillary length [38, 40]. The curvature $R_{\parallel}^{-1}(r) = \zeta''(r)$ is nearly maximal at $r = \ell_{curv}$, so we take R_{\parallel} and σ_{\parallel} there. For the inflated membranes, $\sigma_{\parallel} \approx PR_{\parallel}$ comes from force balance on the small cylindrical patch, R_{\parallel} is measured using a set of paper stencils of circular arcs, and ℓ_{\parallel} is measured by laying a string along the buckled region. Reproduced from Timounay <i>et al.</i> [19] | 31 |
| 3 | Non-dimensionalization of experimental parameters for use in the simulations. | 53 |

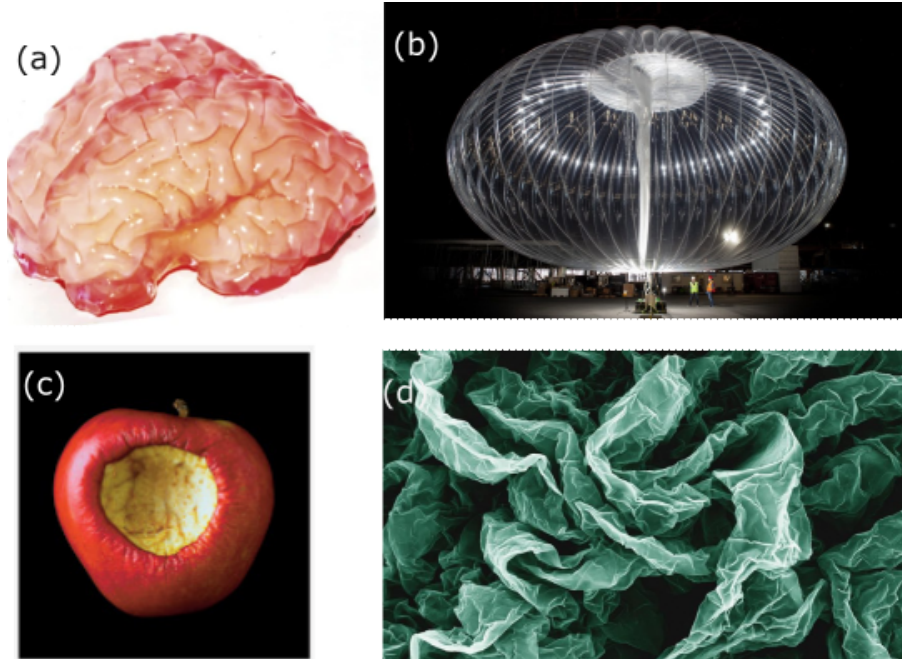


Figure 1: **Pattern formation in thin films** (a) Gyrification in a mechanical model of a brain [2]. (b) Wrinkle patterns in deployable weather balloons [3]. (c) A partly bitten off apple left for a day starts wrinkling around the bitten off edge. [4] (d) A crumpled graphene film.[5]

1 Introduction

A wide variety of surfaces in nature are wrinkled, crumpled, or folded (Figure 1). These patterns can have far-reaching effects: folds or ridges in the brain [1, 2] can increase the neuron density, and wrinkles in leaves can change their wetting properties. The variety of morphologies of a compressed film is quite large: they can be smooth and undulating, sharp and focused, and this buckling can occur on small or large scales.

When we hold a piece of paper at one of its corner, we can see that it flops down instead of remaining in the same plane. What if we now roll the paper and then hold it at the same edge? We will see that that the paper now remains stiff and in plane. This is because the paper has used up its free energy by folding. Further out of plane bending will need the paper to stretch or compress which the paper think is costly, as bending in two orthogonal directions must cause in-plane strains. This qualitatively shows that paper

(thin film) prefers to bend rather than stretch as the latter costs significantly more energy. Such bending deformations can lead to large-amplitude buckled shapes, even under a small applied forces, which can make predicting their behavior challenging.

Thin films have shown several applications over the last decade in solar panels [6] for energy generation to drug delivery[7]. Sharp, localized deformations create points of weakness that can cause thin structures to fail. Understanding defects on thin films and predicting their occurrences can not only prevent accidents but also help in developing more cost-effective and long- lasting designs. On the flip side, buckling can also be beneficial for you. These features can be used to effortlessly create texture over large surfaces. Studies have shown that rough microstructures on (biomimetic) implant surface can promote biocompatibility by promoting ingrowth of tissues.

Here we will study how membranes transition from sharp localized structures to smooth undulations, when they are confined in various geometries and subjected to tensile stresses. Then, we will study how a thin film floating on an interface responds to a mismatch in geometries between the sheet and the surface. We will explore both its dynamic and static characteristics in this setting.

1.0.1 What is "Wrinkling"?

Wrinkling is a mechanical instability that can be seen in a wide range of materials, from a half eaten apple (see Figure 1c), to hanging curtains, to suspended graphene sheets [9]. They are just one example of a type of complex deformation whose behavior is governed by a set of nonlinear partial differential equations, known as the Föppl–von Karman equations.

When a thin stiff film resting on a soft substrate is compressed, wrinkles occur. The film would prefer a large wavelength buckling mode to minimize the elastic cost of bending. But, the substrate under the film would prefer small-wavelength deformations, to minimize its energy (for a solid foundation, its elastic energy; for a liquid substrate, its gravitational potential energy). Thus, a balance needs to be found between these two extremes so that

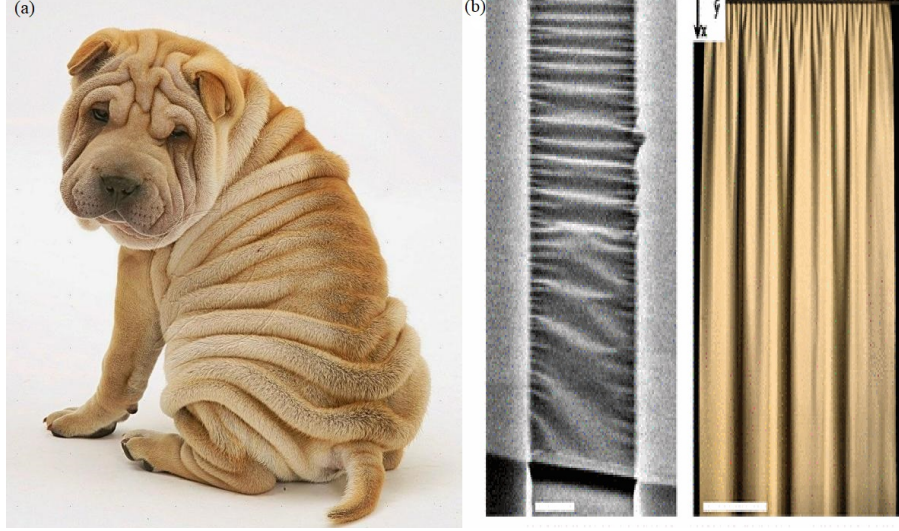


Figure 2: **Wrinkling in various systems** (a) Wrinkling occurs in nature in many instances like the ones seen in Shar Pei dogs. [8] (b) Scanning Electron Microscope of wrinkled graphene, compared with wrinkle patterns on a curtain [9].

the total energy is minimized. First we denote the height of the film as the given function:

$$h(x) = A \sin\left(\frac{2\pi x}{\lambda}\right) \quad (1)$$

Where, A is the amplitude and λ is the wavelength of the undulations.

The gravitation and bending energy can be denoted by:

$$U_g = \frac{1}{2}K \int_{-\infty}^{\infty} h^2(x)dx \int_0^w dy \quad (2)$$

$$U_b = \frac{1}{2}B \int_{-\infty}^{\infty} \left(\frac{\partial^2}{\partial x^2}h(x)\right)^2 dx \int_0^w dy \quad (3)$$

where K denotes substrate stiffness and B corresponds to the bending modulus. Here w denotes the width of the film.

On substituting the height function in the above integral we obtain,

$$U_g = \frac{1}{2}KA^2w \int_{-\infty}^{\infty} \sin^2\left(\frac{2\pi x}{\lambda}\right) dx \quad (4)$$

$$U_b = \frac{1}{2}BA^2w \left(\frac{2\pi}{\lambda}\right)^4 \int_{-\infty}^{\infty} \sin^2\left(\frac{2\pi x}{\lambda}\right) dx \quad (5)$$

Thus the total energy is given by,

$$U = U_g + U_b = \frac{1}{2}KA^2wI + \frac{1}{2}BA^2wI \left(\frac{2\pi}{\lambda}\right)^4 \quad (6)$$

Where, I is the integral.

Here we will assume that the amplitude is a dependent variable and is directly proportional to the wavelength of the film. ($A = C\lambda$) The balance between the substrate stiffness and bending energies leads to the selection of wrinkles of an intermediate wavelength λ [10]. Thus in order to minimize the energy we take the partial derivative of eqn. 6 with respect to λ

$$\frac{\partial}{\partial \lambda} U = \frac{\partial}{\partial \lambda} \left(\frac{1}{2}KC^2\lambda^2wI + \frac{1}{2}BC^2\lambda^2wI \left(\frac{2\pi}{\lambda}\right)^4 \right) = 0 \quad (7)$$

Thus computing the above equation gives,

$$\lambda = 2\pi \left(\frac{B}{k}\right)^{\frac{1}{4}} \quad (8)$$

1.0.2 From smooth wrinkles to sharp “crumples”

Unwrapping a candy wrapper or unravelling a crushed piece of paper reveals a vibrant and complex surface with infinite configurations of disorder. These complex systems primarily focus elastic energy at a point called d-cones or along a line called ridge. Such stress focusing singularities can occur in systems spanning a wide range of length-scales: One can find such structures on 2D graphene sheets to factory based wine tanks. Depending on the circumstance they appear they can be blessing or nuisance. Crumpling in graphene sheet promotes increase in surface area, high conductivity as well as stability against graphitization [11] in comparison to its smooth counterpart. However, crumpling in the body of crashed car or on wine tanks after earthquake [12] can reduce its longevity and become the origin of



Figure 3: **Crumpling in various systems** (a) Crumples form on Candy wrappers by twisting a flat sheet around the candy. (b) Crumpling in stainless steel wine tank caused by earthquake. [12]

wear and tear. Thus, understanding them can be very beneficial to create or prevent them.

Unlike wrinkles, crumples are sharp structures that are localized over a small portion of the surface. They are not periodic like wrinkles. These kinds of non-linear deformations are still not very well understood.

1.0.2.1 D-cones

A developable cone (or d-cone) is a cone-like surface that is isometric to a plane almost everywhere, except the tip of the cone where a region of high curvature exists. This high-curvature region has a large elastic energy density and large curvatures and strains. Experimentally, the size of this “core” has been found to grow with the thickness of the material.

D-cones can be easily constructed by taking a circular sheet [13] that is forced axially into a rigid cylindrical hoop of diameter smaller than the sheet. Figure 6 shows the formation of d-cone.

The energy of the d-cone is composed of two parts: A bending contribution in the outer region of the d-cone and stretching and bending region around the tip. [14] The bending



Figure 4: **Developable cone:** An isolated sharp point on a crushed paper can be thought of as a d-cone, constructed by indenting the center of a circular sheet resting on a hoop.

energy of the outer region is given by,

$$U_b \sim \int_{r_c}^R E_b \kappa^2 \rho d\rho ,$$

where B is the bending modulus given by

$$E_b = \frac{Eh^3}{12(1 - \nu^2)} ,$$

and $\kappa \sim \epsilon/\rho$ is the mean curvature of the cone. Substituting the above in bending energy equation gives,

$$U_b \sim \epsilon^2 E_b \log \frac{R}{r_c}$$

where r_c is the cutoff radius.

The energy for the outer region of the cone [15] is given in polar coordinate terms as,

$$E_\kappa = \frac{K}{2} \int_{-\pi}^{\pi} \frac{(\phi + \phi'')^2}{R^2} R \sqrt{\cos^2 \phi + \phi'^2} d\theta$$

where the radius of curvature $\kappa = \frac{(\phi+\phi'')}{R}$. There are other similar energy estimation for the region apart from the core, one of which uses the theory of elasticity [13]. The Lagrange functional is given by,

$$L(\psi) = U_b + \lambda \int_{-\pi}^{\pi} \left[1 - \frac{(1 + \psi^2 + \psi'^2)^{\frac{1}{2}}}{1 + \psi'^2} \right] d\theta + \int_{-\pi}^{\pi} b(\theta)(\epsilon - \psi) d\theta$$

Here $\psi(\theta)$ is the tangent between the generator of the surface and the horizontal. Here the bending energy is given by,

$$U_b = (E_b/2) \ln(R_p/R_c) \int_{-\pi}^{\pi} \frac{(\psi + \psi'')^2 (1 + \psi'^2)^2}{(1 + \psi^2 + \psi'^2)^{\frac{5}{2}}} d\theta$$

where R_p is the radius of the sheet, R_c is the core size radius and E_b is the bending stiffness. The second term corresponds to the inextensibility constraint and λ corresponds to the hoop stress. The third term enforces the requirement that the deformed sheet lies in a perfect cone $z = \rho\epsilon$ and $\epsilon = \frac{d}{R}$. When this functional is numerically computed it yields a solution everywhere except for the tip of the cone. The figure 1 shows the numerically computed ideal conical dislocation. They also estimates the size of the core R_c which is a balance between the bending and stretching energy. If the core area is given by ΔS , the stretching energy in the core is given by,

$$U_b \approx E_b \kappa^2 \Delta S$$

and the stretching energy is given by,

$$U_s \approx E_s \gamma^2 \Delta S$$

where γ is the in-plane strain and E_s is the stretching stiffness. Balancing the energy yields a scaling law,

$$R_c \approx \left(\frac{E_b}{E_s} \right)^{\frac{1}{6}} \epsilon^{-p} R^{2/3}; \quad (9)$$

where $p = 1/3$ when $\epsilon \ll 1$ and $p = 1/2$ for $\epsilon \approx O(1)$

Here κ [14] is the mean curvature of the core. In core, there are two regions where the effect of plasticity and stretching needs to be considered. The first region is the long scar and the second part is near the tip. They find that the energy due to stretching is given by,

$$U_s \sim Eh\epsilon^4 r_c^2.$$

Minimizing the total energy gives a scaling for the core size as $r_c \sim h/\epsilon$.

Liang et al. [16] the numerical analysis of the core yields scaling for the core radius to be,

$$R_c \approx h^{\frac{1}{3}} R^{\frac{2}{3}}$$

Their numerical test corroborates the prediction made by Cerda et al. [14]. In the coming sections, I will explore the stress-focused structures in my inflated membrane system with the scaling parameter of the core of the d-cone to investigate its commonality at large confinement.

1.1 Interfacial films

Thin films when placed on a liquid interface can show various interesting features. The geometry of the film along with the applied stress induces it to form wrinkles, fold or buckle into sharp crumples depending on the more energetically favourable state.

1.1.1 Capillarity

Capillarity [17] is a category of liquid phenomena at small scales, where surface tension plays a major role. We have noticed how liquid meniscus takes various shape depending on the adhesion between the surface around the liquid and the liquid itself. Surface tension also plays a very important factor in these interactions.

Similarly, we can overfill a dish with any liquid and it is held together by the dominance



Figure 5: **Cheerios effect:** Floating soap bubbles on water tend to clump around the rim of the dish.

of surface tension until a certain volume. This liquid typically has convex sides extending to the center up to a certain capillary length depending on the interplay of surface tension and gravity. The center of such liquid drop is typically flat.

1.1.2 Sheet on Drop

One interesting phenomenon that we observe on interface system is when we float a few light objects on water, they tend to collect at the center. We can see this kind of reflection in our day to day life. When we leave last few pieces of Cheerios in our milk bowl, they tend

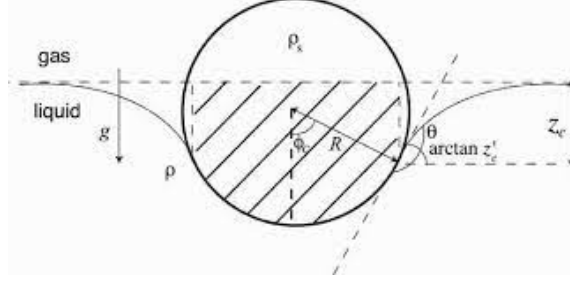


Figure 6: **Partly submerged spherical object:** The shaded area represents weight of the displaced liquid equivalent to the buoyant force on the object [18].

to clump up instead of being dispersed in the liquid. This is a surface phenomenon and is called Cheerios effect.

When heavy objects like coins are placed on a liquid interface, they would like to break the surface and fall through the liquid, but the surface tension of water can sometimes prevent them from breaking the surface. Hence the coins remain afloat. However, the weight of coins still creates a dip around the surface of the coin. These dips have heights lower than the surface. So all the coins tend to conglomerate to essentially find the lowest heights on the liquid surface. Similarly air bubble tend to rise up to the meniscus to escape the surface since buoyant force forces the bubbles to leave the surface whereas surface tension prevent the surface from breaking.

The interface and the interfacial slope can be defined by the equation $h(r)$ and z'_c respectively and can be calculated through the vertical force balance of an isolated floating sphere as seen in Figure 6.

The angle ϕ_c can be written in terms of the slope of the interfacial slope z'_c as:

$$\phi_c = \pi - \theta + \arctan z'_c$$

In order to stay afloat, the weight of the sphere ($\frac{4}{3}\pi\rho_s g R^3$) needs to counterbalanced by the buoyant force of the displaced liquid (shown in Fig 6) and the vertical component of the surface tension along the contact region acting upward. The vertical surface tension (S_{\perp}) is

given by,

$$S_{\perp} = 2\pi R \sin \phi_c \gamma \sin (\arctan z'_c)$$

$$\arctan z'_c = \frac{z'_c}{(1 + z'_c)^{\frac{1}{2}}}$$

Simplifying,

$$S_{\perp} = 2\pi R \sin \phi_c \gamma \sin \frac{z'_c}{(1 + z'_c)^{\frac{1}{2}}}$$

The buoyant force (F_B) is given by,

$$F_B = \pi \rho g R^3 \left(\frac{z_c}{R} \sin \phi_c + \frac{2}{3} - \cos \phi_c + \frac{1}{3} \cos^3 \phi_c \right)$$

Balancing the weight (W) of the floating object with S_{\perp} and F_B gives,

$$W = S_{\perp} + F_B$$

$$\frac{4}{3} \pi \rho_s g R^3 = 2\pi R \sin \phi_c \gamma \sin \frac{z'_c}{(1 + z'_c)^{\frac{1}{2}}} + \pi \rho g R^3 \left(\frac{z_c}{R} \sin \phi_c + \frac{2}{3} - \cos \phi_c + \frac{1}{3} \cos^3 \phi_c \right)$$

Substituting $\phi_c = \pi - \theta + \arctan z'_c$, and keeping the linear terms to z'_c ,

$$z'_c \sin \phi_c = B \left(\frac{2D - 1}{3} - \frac{1}{2} \cos \theta + \frac{1}{6} \cos^3 \theta \right) \equiv B \Sigma \quad (10)$$

where B is Bond number, D is interfacial density ratio. $B \equiv \frac{R^2}{L_c^2}$ and $D = \frac{\rho_s}{\rho}$

While the Cheerios effect in stiff objects is well studied, there are no physical framework to understand how a thin film will react under same setting. Thin films are highly bendable yet unstretchable materials. When thin film is typically placed on geometrically mismatched liquid interface, they tend to acclimate with the surface by forming smooth undulating features called wrinkles to relieve the stress from being on curvature mismatched surface since it has very low bending cost unlike a stiff object placed on a interface that pulls up liquid to conform with the surface since it is energetically more costly to bend. This system

can be studied using the overfilled petri dish as explained in [1.1.3](#).

1.1.3 Computational approach to curvature-induced propulsion:

To investigate this phenomenon in depth, we desire a computational method that can calculate the energy of the system in its different configurations. A simulation of the equilibrium shape of a wrinkled sheet on a droplet can give us access to system energies that are not readily measured in experiments. Furthermore, a simulation can allow us to change all the relevant parameters in the problem, including surface tension, liquid density, and geometric parameters such as the size of the sheet, size of the dish, and volume of water in the dish.

To perform such simulations, we use Surface Evolver, which is a C based software that examine liquid surfaces created as simplicial complex that is governed by surface energy and gravitational energy. It can also model some thin elastic objects through the incorporation of elastic stretching energies. It uses optimization technique called gradient descent to optimize the total energy of the system. In order to optimize a system through Surface Evolver, we create a file containing the initial vertices, edges and body of the system along with the iteration steps and constraints that needs to be applied to the system.

2 Stress focusing in inflated membranes

*This chapter is based on a paper published in **Physical Review X** 10, 021008(2020) with coauthors Y. Timounay, J. Stelzel, Z. Schrecengost, M. Ripp, and J. Paulsen [19]. My contribution was developing the inflated membrane system that helped us generalize the wrinkle-to-crumple transition to a broader range of settings. I measured the morphology of the crumpled phase in this system, and the threshold parameters for crumple formation. I was also a direct mentor to coauthor J. Stelzel (REU student in summer 2018).*

2.1 Popular Summary

As our birthday approaches, don't we start panicking about that one new wrinkle that has popped up on our forehead? Aging and wrinkling are inevitable. Now, what about the crumpled piece of paper you tossed in the trash? Are those crumples the same as the wrinkles on your skin? You might be tempted to answer that these features are not very similar and probably dependent on the material. But what if I told you that my research shows how to morph sharp crumples into smooth wrinkles and back, demonstrating that these patterns are far more universal than ever thought before. The inspiration for my experiment came from what we usually find in our birthday parties- Mylar balloons. In the lab, we take a plastic sheet and make balloon out of them by heat sealing the sides. When we slowly inflate them with air, we observe that at high pressure, the bag tucks extra material into smooth undulations, called "wrinkles", whereas at a particular lower internal pressure, these regions transition into sharper "crumples". But why are we excited about this phenomenon? To answer this, let's back up 10 years, to the first time the wrinkle-to-crumple transition was witnessed in the lab [20, 21]. Researchers saw this transition in an experiment where a thin film was placed on a spherical water droplet. But it was not clear how general the wrinkle-to-crumple transition could be. For instance, could it occur if the sheet was draped in a saddle shape, or formed into a cylinder? Could it occur on larger-scale objects, much larger than a droplet of water? Could it occur in soft materials like rubber, as well as stiff materials like mylar? These questions had remained open for years, until my results gave a resounding 'yes'. In other words, I can now claim that the wrinkles on our skin and the sharp ridges in a crushed wad of paper are fundamentally linked.

2.2 Introduction

When unrolling plastic wrap, handling a large flimsy poster, or watching a fluttering flag, we witness a multitude of deformations available to thin sheets. In some cases, the shapes

are smooth and diffuse like the undulating edge of a flower [22, 23, 24], while in others they are sharp and localized like the ridges and corners in a crumpled piece of paper [25, 26, 27, 28]. Although much progress has been made to describe a wide range of deformations and patterns, a general understanding of the transition from smooth to sharp topographies under featureless confinement remains a major challenge. Such an understanding promises broad practical implications from controlling surface patterning through buckling [29, 30] to anticipating material degradation due to the focusing of stresses at elastic singularities [31, 32, 33].

Many of these rich and complex morphologies stem from a basic consideration: A sufficiently thin sheet prefers to minimize costly stretching deformations in favor of low-energy bending. For sheets constrained to planar or gently curved topographies, wrinkles are an effective method for relaxing compressive stresses while minimizing out-of-plane displacements [34, 10, 35, 36]. Wrinkles can even allow an initially planar sheet to hug the contour of a doubly-curved geometry, such as a sphere or saddle, with negligible stretching [37, 38, 39, 40, 41, 42]. Yet, under sufficiently strong confinement, a sheet may concentrate strain energy along localized ridges or singular vertices to lower the total elastic energy [43, 26, 44]. In this article we study the transition from smooth to sharp deformations in general geometries, and we find a common response whereby wrinkles are replaced at large imposed curvatures by a generic buckling motif, termed “crumples”.

The realization that both wrinkles and crumples can form sequentially under gradual confinement was the outcome of recent work by King *et al.* [20, 21]. In their experiments, an initially-flat circular sheet is placed on a spherical water meniscus. As the curvature of the interface is gradually increased, a wrinkled state gives way to a different deformation mode with a finite number of stress-focusing patterns (Figure 7a). This progression reveals two distinct symmetry-breaking transformations: First, wrinkles break the axial symmetry of the deformation field, and crumples subsequently break the axial symmetry of the stress field [20]. Yet, despite the practical importance and fundamental nature of the crumpling

transition, a predictive understanding has remained out of reach.

Here we study the wrinkle-to-crumple transition in a set of model experiments on macroscopic inflated membranes. To provide a broader context for my experiments, I also report some of the experimental results by my coauthors on ultrathin polymer films. First, we show that this transition appears to be generic: We observe a strikingly similar morphological transition in hyperbolic and cylindrical geometries. Moreover, by isolating the wrinkle-to-crumple transition in a membrane inflated with gas, we show that the phenomenon is scale-free, and we identify robust morphological features of the crumpled phase that are shared across a diverse range of setups.

We then characterize the crumpling threshold. We cross this transition by varying the curvature along the wrinkle crests in the interfacial films, and by modifying the tensile stresses along wrinkles in the inflated membranes. We generalize an empirical threshold from previous work [20] to give an approximate criteria for the transition, and we show that a full account of the crumpling threshold must also include the fractional in-plane compression.

Wrinkles, folds, creases, ridges, blisters, and other buckled microstructures have been studied extensively in recent years [45, 46, 47, 48, 49, 29, 30]. Crumple formation and evolution have not been documented to a similar extent and are still poorly understood. Our experimental measurements and phenomenological description provide a foothold for a theoretical understanding of this ubiquitous transition.

2.3 Experimental Systems

The wrinkle-to-crumple transition was first reported in a setup where a thin circular sheet rests on a spherical water droplet. Two other systems were developed by Monica Ripp and Yousra Timounay, in geometries that differ from the spherical setup were studied. Polymer films of thickness $40 < t < 630$ nm and Young's modulus $E = 3.4$ GPa by spin-coating solutions of polystyrene ($M_n = 99000$, $M_w = 105500$, Polymer Source) in toluene (99.9 %, Fisher Scientific) onto glass substrates, following Ref. [50]. The films were cut into various

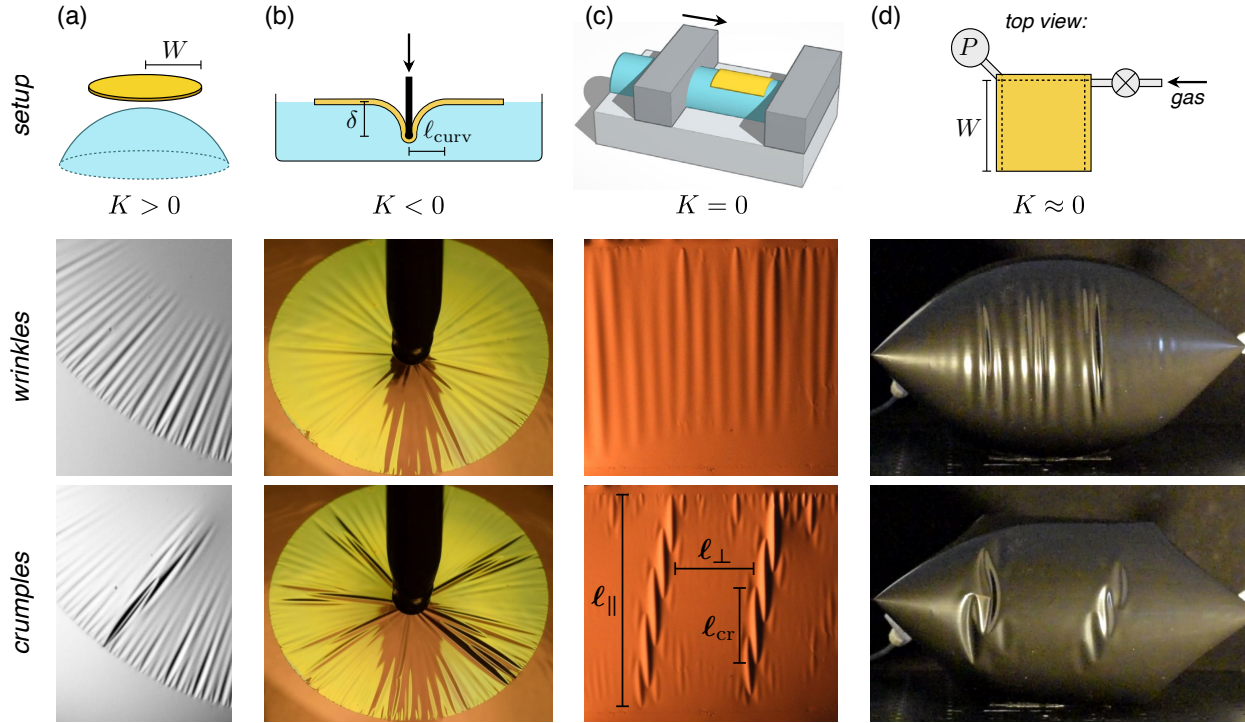


Figure 7: **The crumple-to-wrinkle transition is seen in various geometries, boundary conditions, and system sizes.** The top row of this figure shows schematics of each setup considered in this study with the Gaussian curvature in the area relevant to the transition marked underneath each schematic. (a) An intrinsically flat circular PS sheet ($E=3.4$ GPa) of with radius $W = 1.5\text{mm}$ and thickness $t = 77$ nm on a liquid meniscus forms crumples when the droplet is highly curved. (b) a PS sheet floating on a liquid bath forms crumples when indented past a certain threshold depth. This image shows a film with $W = 11$ mm and $t = 436$ nm. (c) The central portion of a rectangular PS sheet with $t = 157$ nm, width $W = 3.3$ mm, and length 9.7 mm on a cylindrical water meniscus compressed uniaxially between two barriers. Wrinkles form when the curvature is low and crumples form when the curvature is increased along the wrinkles. (d) A square polyethylene bag ($t = 102$ μm , $E = 210$ MPa) forms wrinkles at high internal pressure, P . Crumples appear at lower pressure. The bag is $W = 20$ cm wide when deflated. [19]

shapes and float them onto deionized water with surface tension $\gamma = 72$ mN/m. These experiments fall in a regime characterized by weak tension, $\gamma/Y < 10^{-3}$, and negligible bending stiffness, characterized by large “bendability” [35], $\epsilon^1 = \gamma W^2/B > 10^4$, where $Y = Et$ and $B = Et^3/[12(1 - \Lambda^2)]$ are the stretching and bending moduli, respectively, with Λ the Poisson’s ratio. Such films can withstand only vanishingly small levels of in-plane compression before they buckle out of plane. They indented a circular film of radius $11 < W < 44$ mm by a vertical distance δ using a spherical probe. At a threshold δ , wrinkles form within a narrow annulus due to the azimuthal compression that would have been induced by the contraction of circles. The wrinkled region grows with increasing δ until it covers the sheet [51]. Beyond another threshold, some wrinkles increase in amplitude and develop into crumples, while the amplitude in the intervening regions decreases. The transition resembles the response in Figure 7(a), despite the markedly different geometry and loading.

Figures 7(a) and 7(b) leave open the possibility that geometric incompatibility plays an important role in crumple formation. However, a crumpling transition can also be observed in a cylindrical geometry, where the Gaussian curvature of the gross shape is conserved while a principal curvature is made to vary. The buckled sheet forms parallel wrinkles that transition into crumples beyond a threshold meniscus curvature [Figure 7(c)].

To probe the generality of this transition further, we perform experiments where we quasistatically inflate sealed plastic membranes while measuring their internal pressure [Figure 7(d)]. Square membranes of width $10 < W < 31$ cm and thickness $15 < t < 222$ μ m are made by folding a rectangular sheet in half and sealing the three open sides. We use a variety of materials, including low-density polyethylene, perfluoroalkoxy alkane (PFA), polyolefin shrink film (SYTEC MVP), aluminized Mylar, and natural rubber, in order to vary the Young’s modulus over a wide range ($2.0 < E < 1500$ MPa), which we measure using a tensile tester (TestResources Model 100P). This system and its findings will be elucidated in the following sections.

2.4 Experimental setup

2.4.1 Preliminary setup

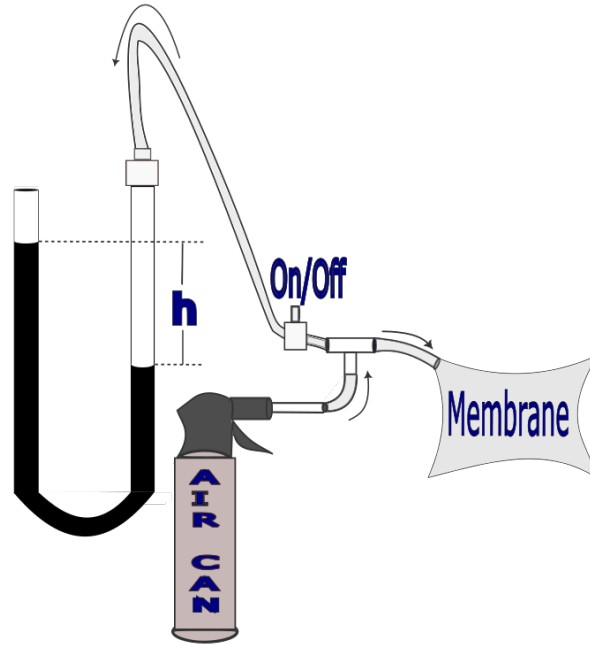


Figure 8: Schematic graph showing the preliminary setup for performing the experiment.

In the nascent stage of the inflated membrane experiment, we had constructed a setup with the membrane connected to the manometer which is a fluid filled U-tube that measures the pressure using the liquid displaced from its original position. The other junction of this valve was connected to the air inflow using a pressurized air can. However, this setup had its drawbacks: first, recording the data for pressure in the membrane could have some discrepancy as the pressure that was being recorded could be the pressure of the in-flowing air from the can rather than the membranes, second, even though manometer itself gives quite accurate measurement, the scale which measured the water displacement had 1 mm as its smallest division making it difficult to record the smallest changes in pressure and finally, there were chances of water overflow, if the membrane was not inflated slowly and carefully. Hence the measurements had room for improvement. Therefore, we decided to take a different approach using pressure gauge for higher accuracy in measurement.

2.4.2 Pressure gauge

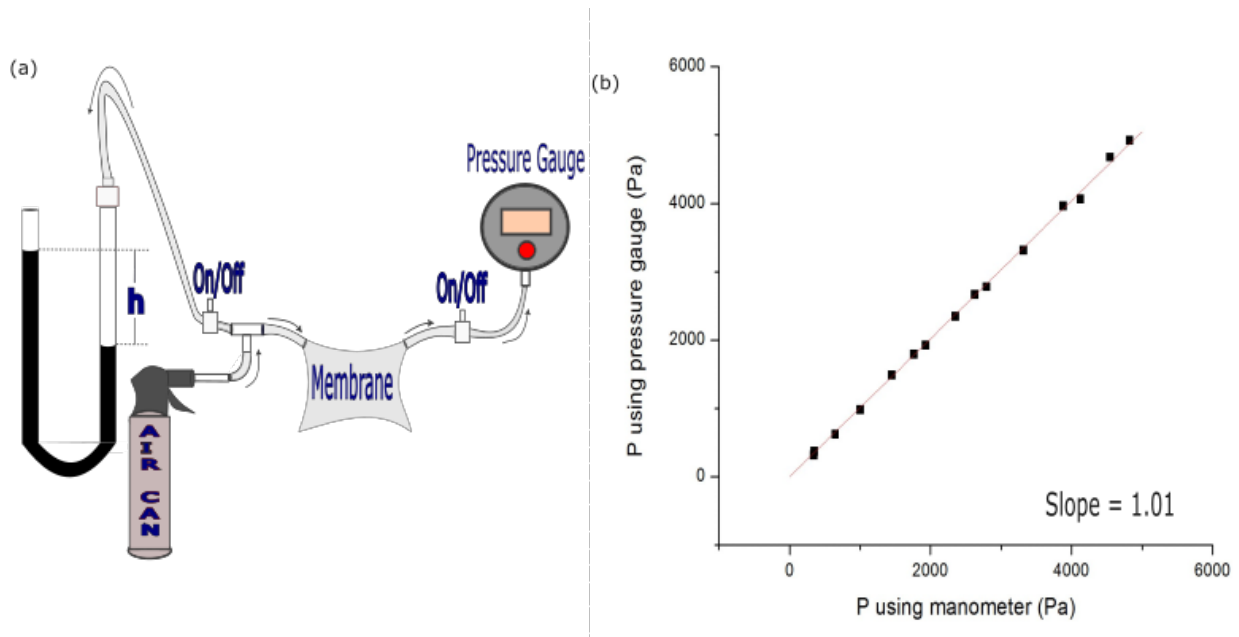


Figure 9: **Pressure gauge calibration:** (a) Measuring the pressure through pressure gauge and manometer simultaneously. (b) Graph comparing the pressure data obtained from manometer and the pressure gauge. Schematic graph comparing the pressure data obtained from manometer and the pressure gauge.

Pressure gauge measure the force a fluid (liquid or gas) exerts per unit area. Pressure gauges can be much more precise in it's measurement in addition to being digital. Thus we remodelled our setup with pressure gauge instead of manometer. But, before we start discussing the final setup we need to verify if the pressure gauge used for this experiment is giving us accurate results. We had previously developed a manometer setup to measure the pressure. In order to verify the credibility of the pressure gauge data, we connected both the manomemeter and pressure gauge to the plastic membrane and record the pressure. We plot these data in x-y axis respectively (Figure 9). The slope obtained from the graph is 1.01. Thus, the two methods give consistent results.



Figure 10: Inflating membrane experiment is recorded using DSLR camera with the corresponding pressure measured using pressure gauge

2.4.3 Final Setup

We construct a membrane with myriads of materials (discussed in table 1) with two openings. One of the opening is connected to the pressurized air cans supplying a colourless gas to inflate the bag. The other opening is connected to the pressure gauge measuring instantaneous pressure of the inflating membrane. However, the pressure gauge is separated from the rest of the setup so that the video can capture the transition in the bags as well as the pressure corresponding to those changes. The camera is mounted on a tripod in front of this setup.

We record a video of this setup from the point the bag starts inflating. These membranes on inflating show crumples that transition to wrinkles. We study the crumples observed on the side of the bag with non-sealing boundary. On inflating the membrane further, at certain pressure these crumples transition to smooth periodic wrinkles.

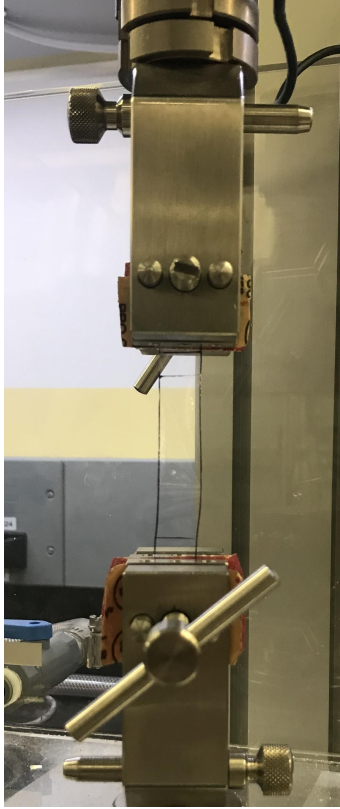


Figure 11: Thin film mounted between the clamps of the tensile testing instrument.

2.4.4 Tensile Testing

Tensile tester is an electromechanical machine that is implemented to determine material strength and deformation behaviour until break. It is controlled by testing software in which we input the machine settings and the parameters of the sample. Once we have the system ready, we start recording the force applied and elongation of the specimen. We are measuring the Young's Modulus of the materials used for our system.

The materials used for constructing the membranes for our experiment has been carefully studied for their Young's modulus through tensile testing machine since it is an important parameter for our experiment. At first, we prepare the samples by cutting rectangular strips of respective materials of dimension $3'' \times 0.5''$ with excess $0.5''$ marked on either side of the strip such that those demarcations can serve as guidelines for mounting the strip between the clamps of tensile testing machine. We have collected samples by cutting rectangular

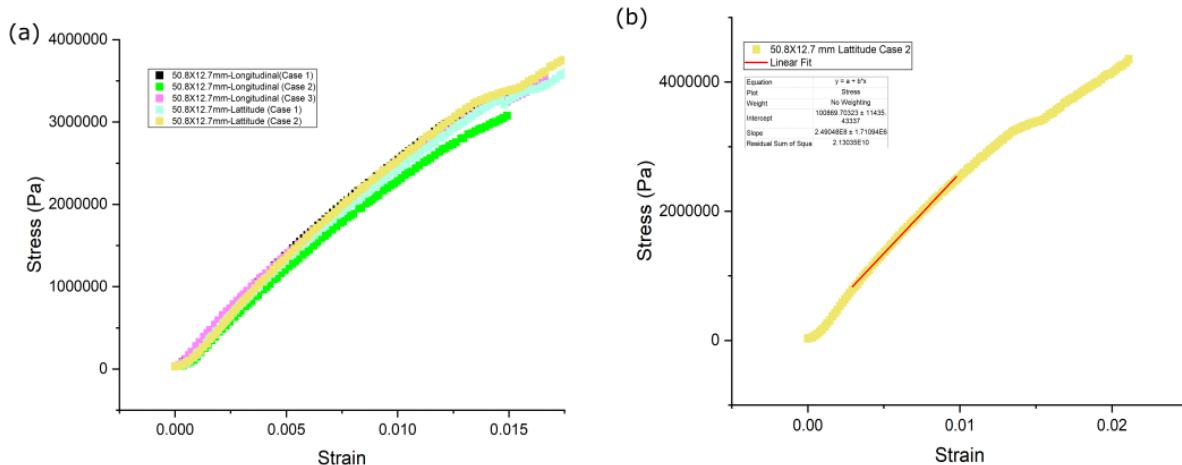


Figure 12: **Determining Young’s Modulus:** The stress over strain graph for LDPE sheets of 0.006" thick. Multiple film strips were measured for its two orientation. The region between the red lines is used to determine the Young’s Modulus of the material.

strip in both lateral and perpendicular orientation from the roll such that we can verify if the sheets have any bi-axial material properties. We have repeated this experiment for all the materials that have been used to construct the membranes. The stress and strain data for each materials are plotted. For precise value of Young’s modulus, we also measured the thickness of the sheets using screw gauge with least count 0.0001".

Since the Young’s modulus is only relevant in Hookean regime, we have calculated Young’s modulus in the region where stress is proportional to strain as shown in Figure 12 (within the red line). The Young’s modulus and the thickness of all the measured films are shown in Table 1.

2.4.5 Membrane Construction

The materials in Table 1 come as sheets. These sheets are then used to carefully develop membranes of specific sizes using various methods. The primary method that has been used especially to make LDPE bags of varying thickness is, using heat impulse sealer shown in figure 13.

Heat impulse sealer sends a pulse of electricity that provides high level of heat for a

| Material | Young's modulus(MPa) | Thickness(μm) |
|---------------------------------------|----------------------|----------------------------|
| Low Density Polyethylene(Transparent) | 152 | 52.4 |
| Low Density Polyethylene(Transparent) | 183 | 103 |
| Low Density Polyethylene(Transparent) | 237 | 157 |
| Low Density Polyethylene(Black) | 297 | 49 |
| Low Density Polyethylene(Black) | 208 | 102 |
| Mylar | 1500 | 24.1 |
| Perfluoroalkoxy | 391 | 27.4 |
| Polyolefin | 164 | 15.6 |
| Polyolefin | 170 | 18.1 |
| Natural Rubber | 2.05 | 163 |
| Natural Rubber | 2.18 | 222 |

Table 1: Materials used to construct membranes

few seconds when the handle is pressed down. The heat can be adjusted by the knob on it. We found that keeping it at 5 while making LDPE membranes seal them optimally and give them clean seams. However, for the Perfluoroalkoxy(CHTP) membranes even after heat sealing the seams, typically have some leaks. Hence, the seams are reinforced by applying the epoxy glue and hot glue gun mixture. However, for materials like natural rubber we need a different approach since the heat sealer has no effect on the sheet due to high melting point of natural rubber. The membranes from natural rubber are developed by sealing the edges with duct tape. If it shows any leak under inspection they are sealed with a hot glue gun. The bags also need to have two openings- one for inflowing air in the bags and the other for connecting it to the pressure gauge to measure the instantaneous pressure.

For the LDPE membranes, these openings can be sealed with hot glue gun. However for the CHTP bags this need to glue with epoxy glue as well as a hot glue gun, due to the surface properties of these sheets.

The membrane size for all these materials varies between 10 and 50 cm. The shape of the membranes were also varied. We developed square, rectangle, tetrahedral, turnover and empanada shaped membranes.



Figure 13: (a)Heat impulse sealer. (b)Heat impulse sealer with a heat sealed LDPE membrane.



Figure 14: Natural rubber square membrane of 0.006" thickness.

2.4.6 3D Scanner Setup

We used Next Engine 3D scanner to scan the surface of the membranes while under stress. The 3D scanner can capture an object with multi-laser precision. The acute precision in capturing the surface is very important for our system since we are looking closely at the geometric frustrations on the membrane surface. Studying the topography of these mi-

crostructure can reveal the physics behind these deformations. But before we talk about our setup we had to make sure that the result from 3D scanner is precise. Hence, we first scanned a known sample (see Appendix B for further details).

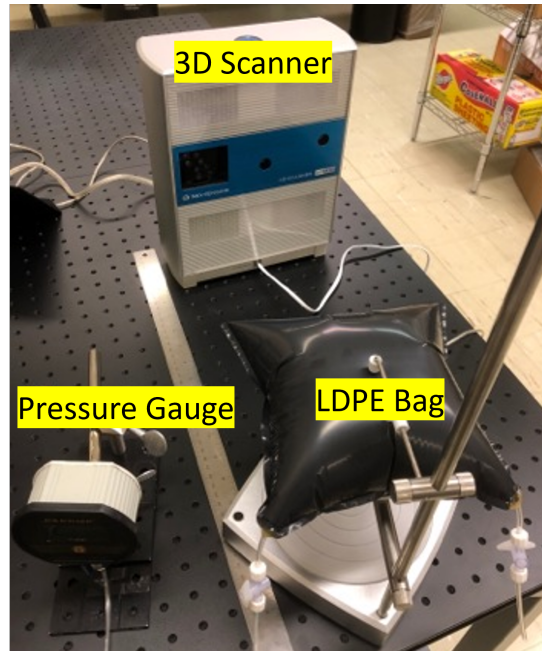


Figure 15: Scanning setup for studying the topography of the membranes.

The setup for our experiment is shown in figure 15. It has the membrane set on rotary sample holder. The membrane is inflated to a certain pressure recorded by the pressure gauge. The 3D scanner is placed about 9.5 inches away from the sample for a bracket scan. The sample membrane is scanned at three angles and the three images are manually stitched together to get the final scanned image. The coordinates of this image is extracted for further analysis that will be discussed later.

2.5 Theory

2.5.1 Föppl-von Kármán equations

Here we discuss the Föppl-von Kármán equations in axial geometry that will form the basis of our theoretical analysis and obtaining the confinement parameter α . This calculation is

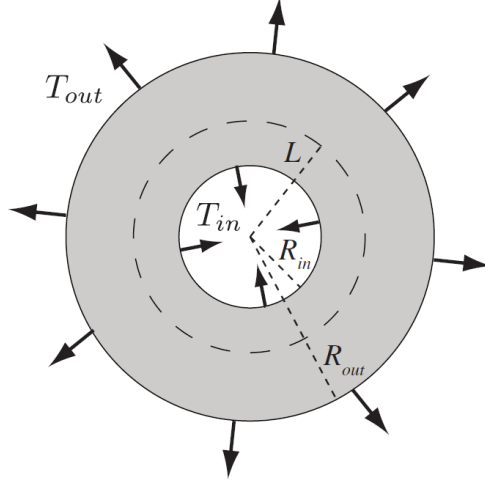


Figure 16: Planar axisymmetric stretching of a circular sheet.

taken from the thesis of H. King [21], where this calculation was done for their sheet on droplet system. At mechanical equilibrium, there is no net force acting on the sheet and the force balance equations are given by:

$$\nabla \cdot \sigma = 0 \quad (11)$$

σ is the in-plane stress tensor.

$$B\nabla^2 Tr(\kappa) + \sigma \cdot \kappa = F_N \quad (12)$$

$B = Et^3/12(1 - \Lambda^2)$, Bending modulus of the sheet, E is the Young's modulus, t is the thickness of the sheet, Λ is the Poisson ratio, κ is the Curvature tensor, $Tr(\kappa)$ is the mean curvature, F_N is the Applied normal force.

This system has axisymmetric stretching applied on it. The in-plane displacement is given by: $u(r, \theta) = u_r(r, \theta)\hat{r} + u_\theta(r, \theta)\hat{\theta}$ and normal displacement $\zeta(r, \theta)$. The strain tensor

is given by:

$$\bar{\bar{E}} = \begin{bmatrix} \epsilon_{rr} & \epsilon_{r\theta} & \epsilon_{r\phi} \\ \epsilon_{\theta r} & \epsilon_{\theta\theta} & \epsilon_{\theta\phi} \\ \epsilon_{\phi r} & \epsilon_{\phi\theta} & \epsilon_{\phi\phi} \end{bmatrix} \quad (13)$$

Since our system is axisymmetric with no out of plane strain, the shear strain and out of plane stress is zero. The strains are given by:

$$\epsilon_{rr} = \frac{\partial u_r}{\partial r} + \frac{1}{2} \left(\frac{\partial \zeta}{\partial r} \right)^2 \quad (14a)$$

$$\epsilon_{\theta\theta} = \frac{1}{r} \frac{\partial u_\theta}{\partial \theta} + \frac{1}{r} u_r + \frac{1}{2r^2} \left(\frac{\partial \zeta}{\partial \theta} \right)^2 \quad (14b)$$

The tension tensor is :

$$\bar{\bar{T}} = \begin{bmatrix} \sigma_{rr} & \sigma_{r\theta} & \sigma_{r\phi} \\ \sigma_{\theta r} & \sigma_{\theta\theta} & \sigma_{\theta\phi} \\ \sigma_{\phi r} & \sigma_{\phi\theta} & \sigma_{\phi\phi} \end{bmatrix} = \begin{bmatrix} \sigma_{rr} & 0 & 0 \\ 0 & \sigma_{\theta\theta} & 0 \\ 0 & 0 & 0 \end{bmatrix} \quad (15)$$

We know stress can be written in terms of strain as Hooke's Law:

$$\sigma = E\epsilon \quad (16)$$

The radial and tangential strain component in terms of stress is given by:

$$\epsilon_{rr} = \frac{1}{Y} (\sigma_{rr} - \Lambda \sigma_{\theta\theta}) \quad (17a)$$

$$\epsilon_{\theta\theta} = \frac{1}{Y} (\sigma_{\theta\theta} - \Lambda \sigma_{rr}) \quad (17b)$$

$Y = Et$, is the Stretching Modulus, E is the Young's modulus, Λ is the Poisson ratio. Therefore, rearranging the above the equations, we find the tensorial form of stresses in

terms of strain:

$$\sigma_{rr} = \frac{Y}{(1 - \Lambda^2)}(\epsilon_{rr} + \Lambda\epsilon_{\theta\theta}) \quad (18a)$$

$$\sigma_{\theta\theta} = \frac{Y}{(1 - \Lambda^2)}(\epsilon_{\theta\theta} + \Lambda\epsilon_{rr}) \quad (18b)$$

Rewriting the Föppl-von Kármán equation 11 using 17 (a) and (b):

$$\hat{r} : \frac{\partial\sigma_{rr}}{\partial r} + \frac{1}{r}(\sigma_{rr} - \sigma_{\theta\theta}) = 0 \quad (19a)$$

$$\hat{\theta} : \frac{1}{r} \left(\frac{\partial\sigma_{\theta\theta}}{\partial\theta} \right) = 0 \quad (19b)$$

Again rewriting the Föppl-von Kármán equation 12 using 17 (a) and (b) and obtaining the normal force balance:

$$B\Delta^2\zeta_0 - \sigma_{rr}\frac{\partial^2\zeta}{\partial r^2} - \frac{1}{r}\sigma_{\theta\theta}\zeta'_0 - \frac{1}{r^2}\sigma_{\theta\theta} \left(\frac{\partial^2\zeta}{\partial\theta^2} + r\frac{\partial\zeta}{\partial r} \right) = F_N \quad (20)$$

2.5.2 Sheet on drop case

Now we are considering Figure 7 (a) setup with a circular sheet placed on a liquid droplet. It is an axisymmetric state system hence all the azimuthal derivative vanishes. However, there is a normal deformation of $\zeta(r)$. Therefore, we can rewrite equation 19 (a) and 20 as:

$$\hat{r} : \left(\frac{\partial}{\partial r} + \frac{1}{r} \right) \sigma_{rr} = \frac{1}{r} (\sigma_{\theta\theta}) \quad (21)$$

$$\hat{z} : B\Delta^2\zeta_0 - \sigma_{rr}\zeta''_0 - \frac{1}{r}\sigma_{\theta\theta}\zeta'_0 = P \quad (22)$$

$P = 2\gamma/R$ is the Laplace Pressure, γ is the Surface tension, R is the radius of curvature. The strain tensors from equation (14) are now:

$$\epsilon_{rr} = \frac{\partial u_r}{\partial r} + \frac{1}{2} \left(\frac{\partial \zeta_0}{\partial r} \right)^2 \quad (23a)$$

$$\epsilon_{\theta\theta} = \frac{1}{r} u_r \quad (23b)$$

Further, we also assume the cost for bending of thin films over liquid drop is negligible. The FvK equations require that the slope on the sheet to be small. The slope ($\zeta'(r) \ll 1$) is given by the ratio of the sheet size W and radius of curvature R . The boundary conditions for these system are:

$$\zeta'_0(0) = 0 \quad (24a)$$

$$\sigma_{rr}(0) = \sigma_{\theta\theta}(0) \quad (24b)$$

$$\sigma_{rr}(W) = \gamma \quad (24c)$$

Substituting $\sigma_{\theta\theta}$ from equation 21 to 22 and integrating it once and using the boundary condition 24(a), we obtain the slope:

$$\zeta'_0(r) = -Pr/\sigma_{rr}(r) \quad (25)$$

Finally, it reduces to first order ODE for stress profile,

$$\frac{\partial \tilde{\sigma}_{rr}}{\partial \tilde{r}} = \frac{1}{\tilde{r}} (-\tilde{\sigma}_{rr} + \tilde{\sigma}_{\theta\theta}) \quad (26a)$$

$$\frac{\partial \tilde{\sigma}_{\theta\theta}}{\partial \tilde{r}} = \frac{1}{\tilde{r}} (\tilde{\sigma}_{rr} - \tilde{\sigma}_{\theta\theta}) - \alpha \tilde{r} \tilde{\sigma}_{rr}^2 \quad (26b)$$

Where $\hat{\sigma}_{rr} = \sigma_{rr}/r$ and $\hat{r} = r/W$.

Solving equation (26) will give us radial and hoop stress as function of the confinement

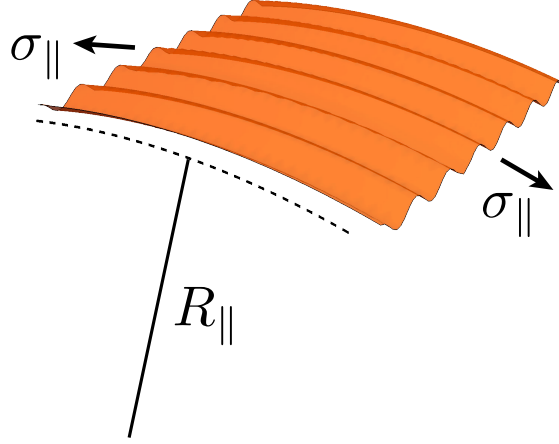


Figure 17: Schematic of a wrinkled rectangular patch, showing σ_{\parallel} and R_{\parallel} . Their values and the total length of the buckled region, l_{\parallel} , are quantified in Table 2 for each setup.

parameter α ,

$$\alpha = \frac{YW^2}{2\gamma R^2}, \quad (27)$$

which may be seen as a ratio of geometric strain ($\sim W^2/R^2$) to mechanical strain (γ/Y). For the experiment in Figure 19(a), King et al. [20] predict the appearance of wrinkles when $\alpha = \alpha_{wr} \approx 5.16$, consistent with their experiments, and they observe a theoretically unanticipated crumpling transition when $\alpha = \alpha_{cr} \approx 155$.

2.6 Parameterization

To generalize this empirical threshold, so that it may be compared with other setups, we replace γ , R , and W with the general set of variables introduced in Table 2. Thus,

$$\alpha \equiv \frac{Y\ell_{\parallel}^2}{2\sigma_{\parallel}R_{\parallel}^2} \quad (28)$$

For the case of a thin circular sheet on a droplet, King et al. [20] identify a basic dimensionless group governing the morphological transitions seen in experiment, given by $\alpha \equiv YW^2/(2\gamma R^2)$, where R is the radius of curvature of the droplet [20]. We show, the crumpling transition in these four experimental setups may be gathered in a single empirical

| Setup | Control Parameter | ℓ_{\parallel} | R_{\parallel} | σ_{\parallel} |
|-------------------|--------------------------------------|---------------------|-------------------------------|--------------------------|
| Sheet on drop | Droplet radius (R) | W/2 (at transition) | R/2 | γ |
| Indentation | Indentation depth (δ) | W | $2.62 \ell_{curv}^2 / \delta$ | $\gamma W / \ell_{curv}$ |
| Sheet on Cylinder | Radius (R), Compression (Δ) | W | R | γ |
| Inflated Membrane | Pressure (P) | Measured | Measured | PR_{\parallel} |

Table 2: Physical scales near the wrinkle-to-crumple transition. Expressions for the buckled length (ℓ_{\parallel}), curvature along the wrinkles (R_{\parallel}), and tensile stress along the wrinkles (σ_{\parallel}), which are pictured schematically in figure 17. Values for the sheet-on-droplet setup are based on Ref. [20]. In this setup, R_{\parallel} and σ_{\parallel} vary spatially: we show their values at the location $r = W$, where the curvature is largest. Values for the indentation are based on the height profile $\zeta(r)$ in the relevant regime where wrinkles cover the sheet. In that case, $\zeta(r) = \delta Ai(r/\ell_{curv})/Ai(0)$, where $Ai(x)$ is the Airy function and $\ell_{curv} = W^{1/3} \ell_c^{2/3}$ with $\ell_c = \sqrt{\gamma/\rho g}$ being the capillary length [38, 40]. The curvature $R_{\parallel}^{-1}(r) = \zeta''(r)$ is nearly maximal at $r = \ell_{curv}$, so we take R_{\parallel} and σ_{\parallel} there. For the inflated membranes, $\sigma_{\parallel} \approx PR_{\parallel}$ comes from force balance on the small cylindrical patch, R_{\parallel} is measured using a set of paper stencils of circular arcs, and ℓ_{\parallel} is measured by laying a string along the buckled region. Reproduced from Timounay *et al.* [19]

phase diagram. In order to draw quantitative comparisons between these four setups, we define a general set of variables for the region of the sheet that is wrinkled or crumpled. We denote the length of this region by l_{\parallel} , as drawn in Figure 19(c), which corresponds to the length of wrinkles when they are present. An individual ‘‘crumple’’ has a length $l_{cr} < l_{\parallel}$ [also indicated in Figure 7(c)]. We denote the radius of curvature and stress along the tensile direction by R_{\parallel} and σ_{\parallel} , respectively, as pictured in Figure 17. Table 2 shows estimates for these variables in each setup. We use these variables to quantify the threshold for crumple formation in Sec. 2.8.1. In Sec. 2.8.3, we clarify the morphology of the crumpled state and how it evolves with increasing confinement.

2.7 Measurement and analysis

We find the transition point from crumples to wrinkles, by analyzing the video of the experiment. We take a snapshot of the image from the video and analyze this image using the ImageJ [52, 53] to obtain the length of the chord (a), the radius of curvature of the bag (R). For the radius of curvature (R), we approximated that the height of the bag should be the

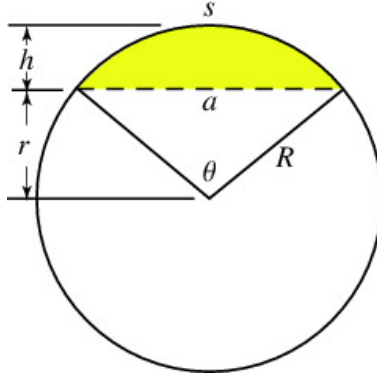


Figure 18: Schematic diagram for chord. [54]

diameter of the curved wrinkled surface. The length of the wrinkle is measured using the following way:

We can assume the wrinkles to be the chords of the circle whose radius of curvature is R . Thus from the figure 18 it is clear that we can measure the wrinkle length if we know the length of the chord a and the radius of curvature R . The equation is:

$$W = 2R \sin^{-1} \frac{a}{2R} \quad (29)$$

We later found an alternative method of measuring R which gave better results. We measure the R by using stencils of various radius which are customized and fitted on the inflated bags at the transition pressure and their corresponding radius of curvature is determined.

2.8 Results

2.8.1 Crumple Threshold

As the membrane is inflated, geometric constraints lead to buckling in four regions along the perimeter. We image the buckled zone on the side of the membrane without a seal while measuring the internal pressure with a digital pressure gauge. At low gauge pressures, crumples are visible in this region; at a higher pressure, they transition into smooth wrinkles [Figure 20]. Observing crumples in this setting without a liquid suggests that they are general

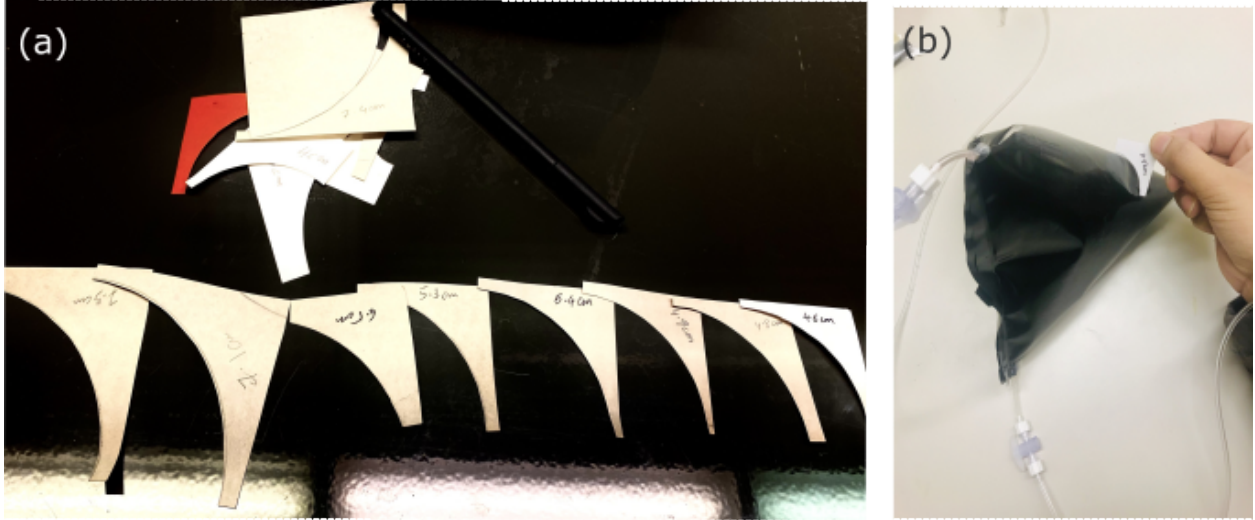


Figure 19: **Measuring R_{\parallel}** : (a) Stencils cut out of stiff board for various radius of curvature. (b) Measurement of radius of curvature using stencils.

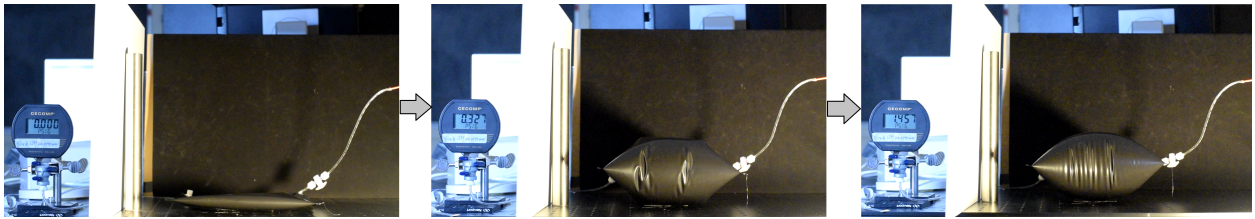


Figure 20: The membrane is inflated gradually. We first observe sharp crumples on the surface followed by transition to smooth wrinkles at a certain pressure.

features that arise out of a minimization of elastic energies in the sheet plus a substrate energy that helps impose the gross shape. . Figure 21(a) shows the crumpling thresholds measured in the four setups, plotted as a function of $l_{\parallel}/R_{\parallel}$ and σ_{\parallel}/Y , which characterize the magnitude of the imposed curvature and tensile strains, respectively. (The right most points indicate that the bags may undergo macroscopic strains of the order of 3% at the transition; the polymer films experience significantly smaller strains.) For the experiments using floating films, the threshold is traversed vertically by varying the imposed curvature $1/R_{\parallel}$. For the inflated membranes, the threshold is crossed horizontally, as changing the internal pressure causes k to vary, while $l_{\parallel}, R_{\parallel}$ remains approximately constant [see the inset in Fig. 21(a)]. The dashed line shows $\alpha_{cr} = 155$. Although there is significant scatter (corresponding to α_{cr} ranging from 23 to 700), this simple scaling organizes the data into a single phase diagram,

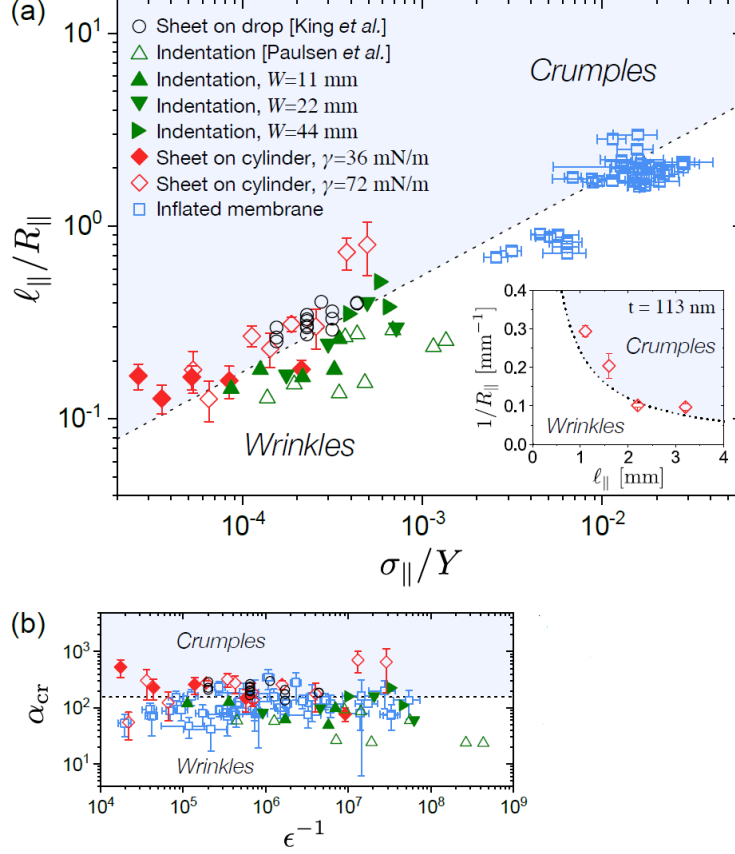


Figure 21: **Phase diagram for wrinkles and crumples.** (a) Crumpling threshold measured in the four experimental setups in Fig. 7, including sheet-on-droplet data from King et al. [20] and indentation data from Paulsen et al. [40]. Values of $l_{||}, R_{||}$ and $\sigma_{||}/Y$, are either measured or deduced from other measured quantities (see Table 2). The sheet thickness ranges from $40 < t < 630$ nm for the polymer films and $15 < t < 222$ μm for the inflated membranes. Indentation data have $Y = 72$ μm and W shown in the legend. Sheet-on-cylinder data have $W = 3.2$ mm and shown in the legend. Parameters for inflated membranes are detailed in Fig. 22(a) and 22(b). The data are reasonably well described by Eq. (28) with $\alpha = \alpha_{cr} = 155$ (dashed line). Inset: Threshold curvature $1/R_{||}$ for crumpling, versus wrinkle length $l_{||}$, in the sheet-on-cylinder setup at fixed t and γ . Dashed line: Equation (28) with $\alpha_{cr} = 155$. (b) Crumpling threshold versus bendability ϵ^{-1} . The threshold is approximately constant over a wide range of bendability.

covering a wide range of experimental setups with different sheet geometries and confinement protocols.

2.8.2 Pressure Threshold

The threshold confinement α_{cr} for inflated membranes may be recast as a threshold pressure. Plugging $\sigma_{\parallel} \approx PR_{\parallel}$ into Eq. (28), we obtain

$$P_{cr} \approx \frac{1}{\alpha_{cr}} \frac{YL_{\parallel}^2}{R_{\parallel}^3} \quad (30)$$

In principle, the threshold α_{cr} may depend on the shape of the bag, but a good estimate should be given by the value measured in the sheet-on-droplet experiments. Figure 22(a) shows the measured threshold pressure in experiments where we gradually increase the internal pressure. We vary the stretching modulus Y over 2 orders of magnitude by constructing bags from different polymer or rubber sheets. The data are captured by Eq. (30), and we obtain $\alpha_{cr} = 100 \pm 30$ by fitting for the numerical prefactor. We also measure the transition upon decreasing the internal pressure in one bag of each material. The open symbols in Fig. 22(a) show these measurements, which are systematically lower than the points for increasing pressure. By cycling the pressure within each bag, we measure a ratio of transition pressures of 0.55 for the polyethylene bag and a ratio between 0.71 and 0.76 for the other four materials. We do not observe such a strong hysteresis in the sheet-on cylinder setup [19]. One possible interpretation is that the larger strains imposed on the bags (estimated by the range of σ_{\parallel}/Y shown in Fig. 21) could lead to larger plastic deformations in both the wrinkled and crumpled phases, thereby biasing the deformation pattern toward what is already there. . We now move to test the generality of Eq. (30) by constructing bags of different shapes, as pictured in Fig. 22(b). Predicting the inflated shape of the bag or the locations of the buckled regions are both nontrivial tasks [55, 56, 57, 58, 59]. Nevertheless, we may simply measure l_{\parallel} and R_{\parallel} at the crumpling transition. Plugging these measurements

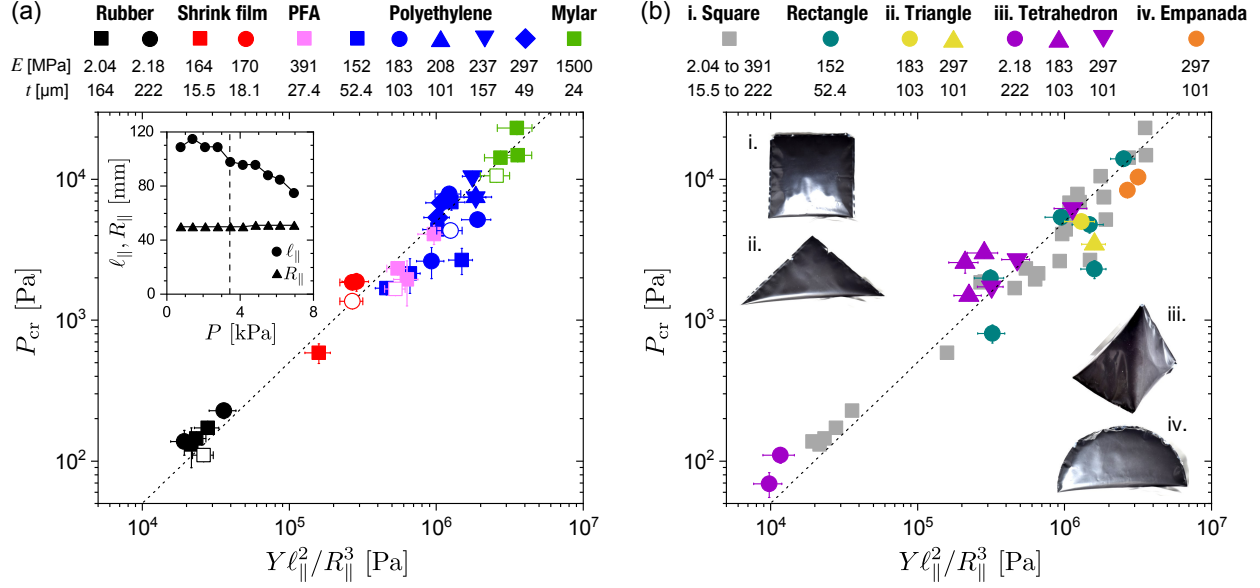


Figure 22: **Pressure threshold for transitioning from sharp crumples to smooth wrinkles in inflated membranes:** (a) Experiments using square bags of various thickness ($15 < t < 222$ m), width ($10 < W < 31$ cm), and Young’s modulus ($2.0 < E < 1500$ MPa). Open symbols show the transition for decreasing pressure; the rest of the data are obtained by increasing the pressure. The data are well described by Eq. (30) with $\alpha_{cr} = 100$ (dashed line). Inset: l_{\parallel} and R_{\parallel} versus pressure for a square polyethylene bag ($W = 20$ cm, $t = 49$ μm). Both quantities are relatively constant near the threshold pressure (dashed line, P_{cr}). (b) Experiments with different bag shapes, which are shown in the insets prior to inflation. We use a variety of polyethylene ($E \sim 200$ MPa) and rubber ($E \sim 2$ MPa) sheets to vary the Young’s modulus and thickness, as denoted in the legend. Here, $9.4 < W < 31$ cm. The crumpling threshold is consistent with the result for square bags, as shown by the gray squares and dashed line that are repeated from (a).

into Eq. (30) gives a good estimate of the threshold pressure P_{cr} for each bag shape, size, material, and thickness, as shown in Fig. 22(b). Moreover, our experiments show that l_{\parallel} and R_{\parallel} do not vary significantly as a function of the pressure, as shown in the inset in Fig. 22(a) for a square polyethylene bag. Thus, one may obtain a basic estimate of the minimum pressure P_{cr} required to replace sharp crumples with smooth wrinkles by measuring l_{\parallel} and R_{\parallel} at lower pressures.

These results suggest that the bag geometry affects the crumpling threshold through a straightforward mechanism, i.e., by creating a compressive zone and selecting l_{\parallel} and R_{\parallel} there. However, as we found from experiments in the sheet-on-cylinder setup that the crumpling

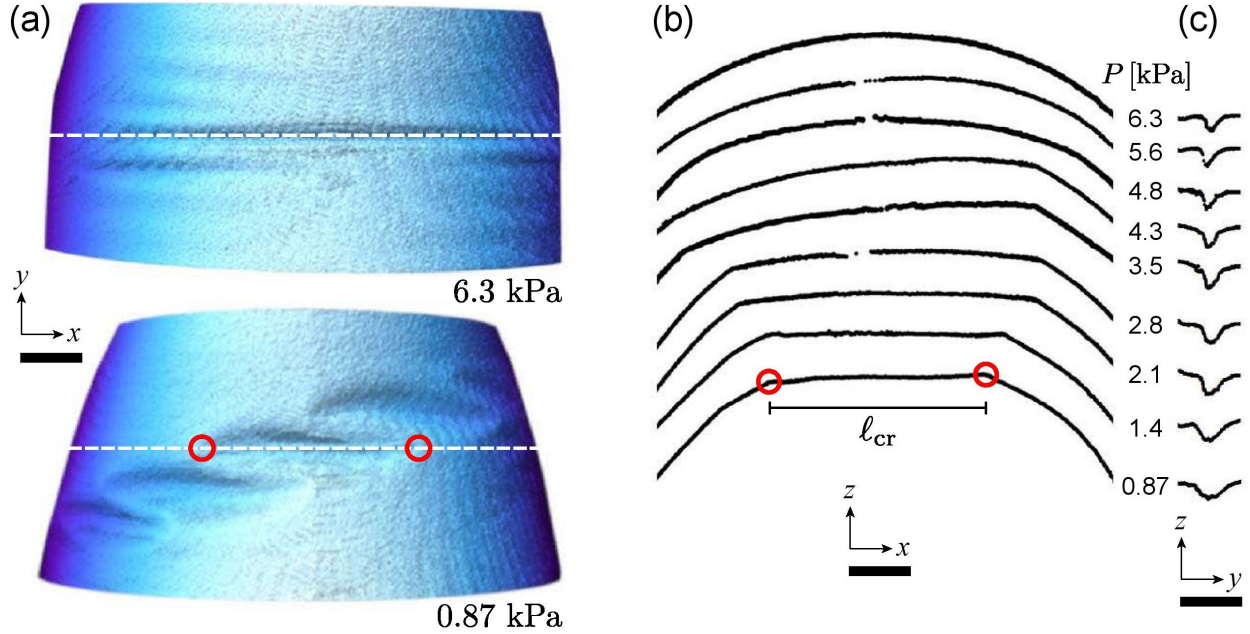


Figure 23: **Crumple morphology:** (a) Renderings of three-dimensional scans of an inflated square polyethylene bag ($t = 49 \mu\text{m}$, $E = 297 \text{ MPa}$, $W = 20 \text{ cm}$), showing the topography of wrinkles (top) and crumples (bottom). (b) Cross sections through a single buckled feature as a function of the gauge pressure. The profiles are taken along the dashed lines in (a), and the two circles highlight the sharp tips at the two ends of the crumple. (c) Cross sections along a perpendicular direction, which show only a small change in width through the transition [the same scale as (a),(b)].

threshold depends also on the compression Δ , which for the inflated membranes depends on the bag geometry and the internal pressure. This additional consideration implies a more nuanced coupling of the bag geometry to the crumpling transition, although it could still be consistent with Eq. (30) with a threshold α_{cr} that depends on the compression, i.e., $\alpha_{cr} = \alpha_{cr}(\Delta)$.

2.8.3 Crumple Morphology

2.8.3.1 Crumple Topography

To define the difference between wrinkles and crumples more precisely, we use a laser scanner to map the three-dimensional topography of a portion of an inflated membrane at several internal pressures. Figure 23(a) shows renderings of the reconstructions at $P = 6.3 \text{ kPa}$,

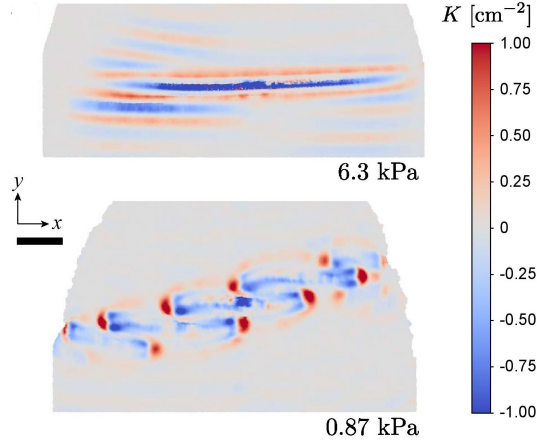


Figure 24: **Crumple topography:** Local Gaussian curvature K for the scans shown in Fig. 23 (a). The wrinkled state (top) shows large positive and negative curvatures along the wrinkle crests and troughs. The crumpled state (bottom) localizes K and, hence, material stresses.

where the sheet is wrinkled, and $P = 0.87$ kPa, where there are crumples, with P being the gauge pressure. Figure 23(b) shows cross sections taken along the central trough, which we track through a series of pressures during a single inflation. At low pressures, the crumple trough is approximately flat and terminates at two localized regions of high curvature [red circles in Figs. 23 (a) and 23(b)]. As the internal pressure increases, these kinks gradually become smoother, while the crumple gets longer until it spans the length of the buckled region; the crumple thereby converts into a smooth wrinkle.

Figure 23 (c) shows the evolution of the same buckled feature along a perpendicular cross section, taken halfway between the crumple tips. This undulation is present through the transition, and it serves to collect excess material due to lateral compression.

2.8.3.2 Gaussian Curvature

The observed wrinkle and crumple morphologies are linked to the distribution of stresses in the sheet via Gauss's theorem egregium. To gain insight into the stress field, we measure the local Gaussian curvature [60] of the scans by fitting small regions to a quadratic polynomial and extracting the principal curvatures from the coefficients of the fit, following Ref. [61].

Figure 24 shows the measured curvature maps for the scans in Fig. 23(a). The wrinkled morphology shows finite Gaussian curvatures in stripes of alternating sign. This result is due to the nearly constant curvature along the x axis and the alternating positive and negative curvature of the wrinkled profile along the y axis, which together imply finite strains and stresses that are spatially extended. In contrast, the curvature map of the crumpled morphology suggests that the material stresses are reduced throughout much of the sheet, at the expense of higher stresses around the boundary of the individual crumples, most notably at their tips. These data support a picture where crumples lower the total elastic energy by condensing stresses to small regions in the sheet.

2.8.3.3 Crumple Length

Focusing now on a single crumple, we examine the cross sections in Fig. 23(b) once again. One can see the crumple length l_{cr} in these profiles at low pressures by noting the distance between the pair of sharp kinks. The mechanism selecting this crumple length is not yet known, and our first task is to identify the parameters that affect it. The cross sections in Fig. 23(b) show that l_{cr} grows as the pressure increases, suggesting that l_{cr} depends on the tensile stress σ_{\parallel} . Optical images of the sheet-on-cylinder and indentation setups show that l_{cr} also depends on the radius of curvature along the wrinkles, R_{\parallel} .

In order to build an empirical scaling relation for the crumple length, we gather images in the indentation, sheet on- cylinder, and inflated membrane setups. Because these systems span multiple scales, we are sensitive to any dependence on the length of the buckled region, l_{\parallel} . We record the longest crumple in each image, since smaller crumples may be associated with boundary effects. In the sheet-on-cylinder setup, we also perform experiments with $\sigma_{\parallel} = \gamma = 36$ mN/m by using a surfactant (sodium dodecyl sulfate). Possible scaling relations for l_{cr} are constrained by dimensional analysis and an observation from our experiments: At the crumpling transition, the crumple length is comparable to the wrinkle length, i.e., $l_{cr} \approx l_{\parallel}$. Based on the crumpling threshold presented in the following section [Eq. (28)], we therefore

expect that $l_{cr} \approx l_{\parallel}^{(1-2\beta)} R_{\parallel}^{2\beta} (\sigma_{\parallel}/Y)^{\beta}$ for some β . Our measurements over two decades in l_{cr} are reasonably described by

$$l_{cr} = 5.6 l_{\parallel}^{0.4} R_{\parallel}^{0.6} \left(\frac{\sigma_{\parallel}}{Y} \right)^{0.3} \quad (31)$$

as shown in Fig. 25(a), which corresponds to $\beta = 0.3$. Notably, the numerical prefactor in Eq. (27) is set by the above arguments, so that is the only parameter we fit to arrive at this result. Our data could also be consistent with β ranging from 0.2 and 0.4. We are not able to produce a significantly better collapse by fitting the three exponents separately.

The above scaling relation does not have any explicit dependence on the lateral compression applied to the sheet, which may explain some of the scatter in the data. Indeed, the images in Fig. 25 show a chain of crumples evolving under increasing compression, which causes l_{cr} to grow. Thus, Eq. (27) is only approximate and should be modified to include a dependence on the compression. Nevertheless, the ability of Eq. (27) to capture our results from three very different systems supports our approach of describing the data using the general set of variables in Table 2.

2.9 Discussion

We have shown that wrinkles are unstable to another buckled morphology at large curvatures, namely, sharp localized crumples. Although this transition was observed in previous experiments on circular polymer films in a spherical geometry [20, 21], we have shown that this symmetry-breaking event appears to be a generic phenomenon by isolating and characterizing the transition in a wide range of experimental setups across multiple length scales. These varied experimental geometries show that crumple formation is not unique to a particular overall Gaussian curvature; rather, crumples are sufficiently robust to form in spherical, hyperbolic, and cylindrical settings. By showing that a quantitatively similar transition occurs for both interfacial films and inflated membranes, our work suggests that a competition of elastic energies along with a suitable substrate energy is enough to give this rich

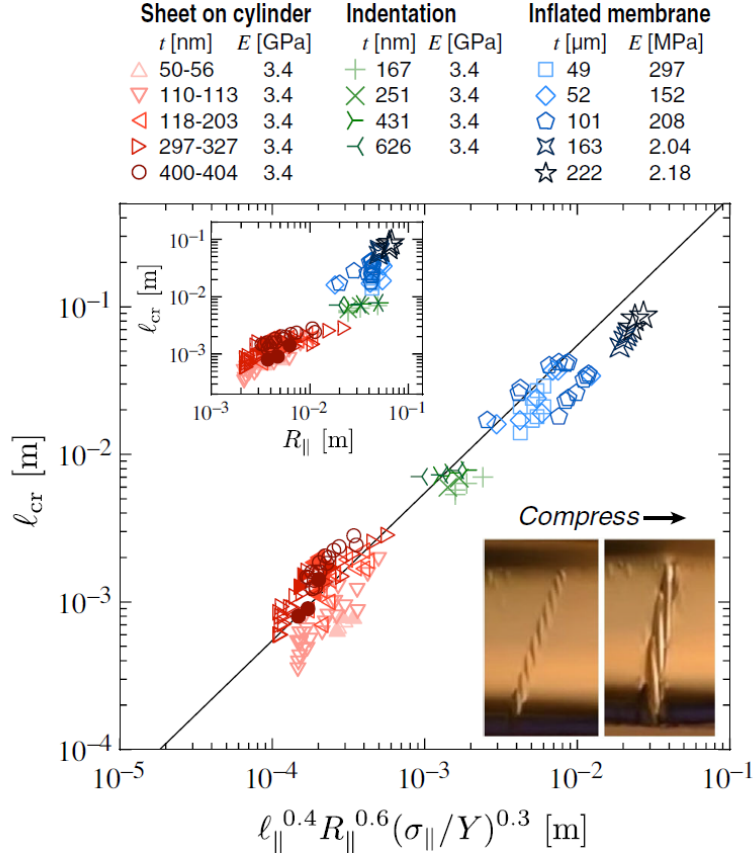


Figure 25: **Emergent scales in the crumpled phase.** (a) Crumple length l_{cr} , measured from optical images in the sheet-on-cylinder, indentation, and inflated membrane setups. The sheet thickness and modulus are varied over a wide range by using rubber ($E \sim 2 \text{ MPa}$), polyethylene ($E \sim 200 \text{ MPa}$), and polystyrene ($E = 3.4 \text{ GPa}$) sheets. We also vary the surface tension in the sheet-on-droplet setup (open symbols, 72 mN/m ; closed symbols, 36 mN/m). The data are reasonably described by a simple expression involving l_{\parallel} , R_{\parallel} , and $\sigma_{\parallel} = Y$ [solid line, Eq. 31]. The two images show l_{cr} increasing upon compression; this behavior may account for some of the scatter in the data. Inset: l_{cr} versus R_{\parallel} , which does not collapse the data.

behavior. This view is plausible given the basic observation that wrinkle crests must traverse a longer arclength than wrinkle troughs in curved topographies, implying costly stretching [40]. Crumples may offer a lower-energy solution by condensing stresses to smaller regions on the sheet. Indeed, our topographic measurements suggest that, at high confinement, a portion of a crumple trough may be nearly developable (i.e., isometric to the original planar sheet). In contrast, the region near a crumple tip has significant localized stretching. Whether this region is well approximated by a d-cone [25, 33, 62, 63, 64], as suggested by King et al. [20, 21], remains to be elucidated. Accounting for the elastic cost of these structures, in a manner that is consistent with various geometric constraints, could give insight into this transition. Another foothold for theoretical study comes from our results in the sheet-on-cylinder setup at large α , which suggest a transition directly from a cylinder to a crumpled state, without an intervening wrinkled state. These experiments open up the possibility that, at a sufficiently large curvature, crumples might be modeled through an expansion around a smooth cylinder in analogy to what has been achieved for wrinkling in the far-from-threshold approach [35, 37, 38, 41]. In contrast to the shell buckling of an axially loaded hollow cylinder [63, 65, 66], the distinctive crumple morphology studied here relies on hoop tension. Cylinders subjected to static circumferential tension are common in industrial settings, for instance, in liquid storage tanks. We note a striking visual similarity between crumples in the sheet-on-cylinder setup [Fig. 7(c)] and the localized buckling patterns that were observed on stainless-steel wine tanks due to an earthquake [12]. Crumples appear to be highly adaptable to a variety of geometries, as shown by the range of experimental setups explored here, and also the variety of membrane shapes. Qualitatively similar features have also been observed in pressurized spherical shells [67] and rapidly crushed conical shells [68], which raise questions about how intrinsic curvature and dynamics could influence stress focusing of the kind studied here. Many of the results presented in this article are suggestive of a local view of crumpling—that is, a description of crumpling in terms of the local values of a small set of variables. In particular, we have shown how the crumpling threshold depends on

the curvature and system size via $l_{\parallel}/R_{\parallel}$, the in-plane tensile strain via σ_{\parallel}/Y . We have also presented a picture wherein the local value of the compression is key to understanding the coexistence of wrinkles and crumples. Despite this promising local view that may capture important aspects of the transition, nonlocal effects may matter as well. In the axisymmetric setups studied here, the curvature and compression vary with the radial coordinate, but we observe chains of crumples appearing along radial lines all at once rather than starting at a location of high curvature and growing in extent with increasing confinement. There are also hints of organization at intermediate scales in the crumpled phase: Chains of crumples seem to have a well-defined spacing between them [l_{\perp} in Fig. 7(c) and θ_{min} [19]]. Although there are fluctuations in this spacing, it appears to have a reproducible minimum value, which is smaller for thinner sheets. These observations are suggestive of a domain structure [69, 70] where chains of crumples are separated by regions of smaller amplitude deformations as a repeated motif. This structure stands in contrast to the space-filling buckling patterns that are observed when a thin cylinder is axially compressed around a mandrel of slightly smaller diameter [71, 72, 73]. Understanding the origin of this emergent mesoscopic length scale, and why it arises for a fluid substrate but not for a solid mandrel, could allow one to control these patterns with a suitably engineered substrate or sheet. On the microscale, wrinkles have been used for metrologies of films [74], for making smart surfaces with tunable wetting and adhesion [75, 76], and to conduct surface microfluidics [77]. Our results expand the vocabulary of film deformations for advanced materials and illustrate how buckled microstructures may change their nature in curved topographies. Discovering the mechanism of this symmetry-breaking instability remains an open challenge that should be the subject of future work.

3 Curvature Driven Propulsion of Thin Floating Films

The research in this chapter is currently being written up for publication in a peer-reviewed journal. The work involves both experiments and simulations. My contribution was developing and conducting Surface Evolver simulations for this system, to measure the potential energy of the system as a function of the position of the film and how it depends on the system parameters. I discovered the dependence of the phenomena on the stretching modulus of the film. I also mentored E. Vieru (Student in summer 2022) who I have supervised as a part of this project.

3.1 Popular summary

Have you ever come across a water strider on one of your fishing or boating trips? Its hypnotizing and fun to watch them gliding on the sparkling water. They make it look so easy. You know it isn't if you have ever tried water gliding! Even then we need some kind of force giving us the push we need to move around the water on a board while maintaining balance. What is the mystery behind such elegant self-propelled gliding motion?

Have you wondered why the foam that spreads over the surface of your freshly poured beer gradually dissipates with remaining bubbles adhering to the edge of the mug? Both of these events might look disparate but if we look closely, water striders and the long-lasting bubbles in foam are both leveraging the surface tensions on liquids to get to their preferred position. They are able to achieve that through a subtle dance in balancing the surface tension of the liquid with the body weight of these objects. But what if we added another layer of freedom to this problem? Unlike bubbles that don't freely bend with interface, lets consider a film that can bend freely like denatured milk protein called "milk skin". What if we take a milk skin and place it on a liquid surface with a different curvature?

Based on my simulations, I can conclude that the film will prefer to be at the matching curvature and propel itself towards the matching curvature while relieving its wrinkles.

Moreover, the simulations predict the system energy for both stretchable and inextensible films. Using a model for the drag on the film, we found the dependence of the velocity on all the relevant factors like size of the film, the meniscus height, and the capillary length of the liquid. This is an interesting result and can have far reaching applications on how drugs [7] are administered in our body to handling oil spills in the ocean.

3.2 Introduction

We have observed cheerios in breakfast bowls clump together when left alone. Cheerios effect [18] is a well studied phenomenon where the effect of the surface dents created by cheerios or any floating object breaks the surface symmetry of the fluid and helps them conglomerate at an interface. Floating objects can create both positive or negative curvatures and attract the same sign curvatures and repel reverse curvatures. Studies have shown the “cheerios effect” with or without buoyant force. Light particles like air bubbles can aggregate as much as heavy particles like quarter coins. Light particles balance themselves on the interface with buoyant force pushing them out while surface tension prevents them from escaping the liquid creating a positive curvature interface. Denser particles on the other hand balances themselves by the gravitational energy pulling the particles down while surface tension prevents the particle from breaking the interface thereby creating a negative curvature interface.

Nature has ample examples of water walking insects to terrestrial insects [78] [79] that exploit the surface tension of water when they need to travel over water surface. Beetle larvae intuitively bend their torso to generate curvature mismatch to generate energy that can propel them towards the meniscus. Mimicking this phenomena, cargo shuttling [79] and meniscus climbing gel robot [80] has been studied in a lab setting.

The objects studied under cheerios effect are usually materials that retain their shape and the fluid adjusts its interface to accommodate these materials. We introduce an unexplored setting where thin films like milk skin that are easily deformable by capillary forces are placed in a positively curved liquid surface. Thin film pinned to a curved liquid surface

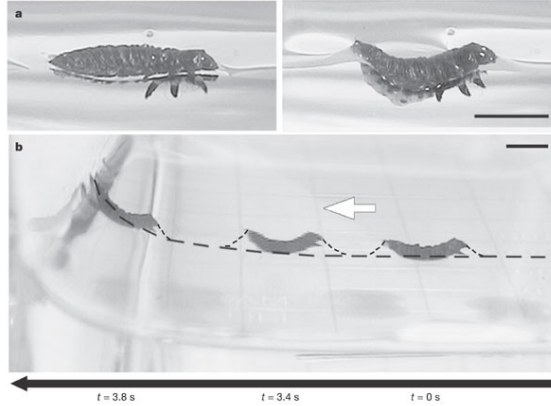


Figure 26: Water lily beetle can bend its body to create curvature mismatch for locomotion. It can bend its body to create curvature mismatch for locomotion. When it is free to move it propels itself towards the flat center. Directional transport of materials over fluid by curvature variance can be an effective way to transport and administer thin film drugs [7] to a known curvature surface in our body.

We use thin highly bendable films to study the effect of mismatched curvature. Thin films are highly bendable but have high cost for stretching. Thin films have shown complex microstructures when constrained to a surface [19]. When a thin film with no curvature is placed on a meniscus, it can bend and relieve its stress by forming smooth undulating wrinkles and wrapping the curved fluid surface [81]. Stiff materials typically pull the interface in a positive or negative curvature whereas thin films create small wrinkles to create an uniform stress field and adjust to the geometry of the fluid surface. The interface geometry is a balance between liquid pulled up by the wrinkled thin film to conform to the fluid interface and the surface tension preventing the deformation of the interface. We explore the behavior of a bendable yet highly inextensible thin film on fluid with a mismatched curvature.

We are able to identify the complex mechanics of propulsion experienced by thin film through model experiments and numerical simulations. Our results give a closer look at the velocity of thin film and energetics of the system and its dependence on the position of the sheet on the interface. Our finding curiously shows that an unstretchable film progresses 10

times faster than the same film with finite stretching indicating the importance of elasticity in such systems.

3.3 Phenomenology from experiment

Recent experiments in the Paulsen lab by Monica Ripp investigated a model setup where a thin polymer film of radius W floating on a water bath with non-constant curvature, accomplished by overfilling (to height h) a circular petri dish of radius L with water so that the central region is flat while the outer boundary is doubly-curved (positive Gaussian curvature) (Fig. 27 a). The liquid has surface tension $\gamma = 0.072$ N/m and density $\rho = 1000$ kg/m³.

The films are highly flexible (characterized by the bendability [20] $\epsilon^{-1} = \gamma W^2/B > 10^3$) yet they resist in-plane stretching (characterized by the ratio γ/Y , which is of order 10^{-3} or smaller). The experiment begins by dragging the film (using a small metal probe) onto the curved meniscus; to accommodate the geometric incompatibility, the film forms many small-amplitude short-wavelength wrinkles around its edge. When the metal probe is lifted, the sheet propels itself away from the meniscus towards the center of the dish. Once the film has relocated to the flat central region of the bath, the wrinkles disappear and the sheet gradually comes to rest.

3.4 Concept of theoretical model

Under the action of surface tension and gravity, thin interfacial solids can easily bend or wrinkle under minute compressive stresses while strongly resisting in-plane stretching. It is appealing to model these thin solids as inextensible, and this limit has been shown to be sufficient to explain the wrapping of a droplet in a thin polymer film [82] or monolayer graphene sheet [83], and the folding of an annular sheet submitted to different inner and outer surface tensions [84]. This approach is motivated by the weak lateral tension and negligible bending stiffness of these films ($\gamma/Y \rightarrow 0$ and $\epsilon \rightarrow 0$). In this asymptotic regime,

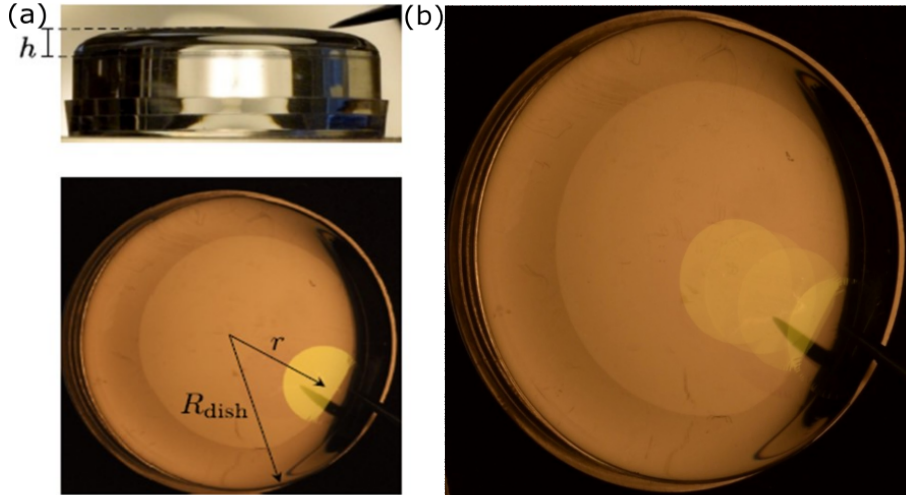


Figure 27: **Experimental Setup.** (a) Side and top view of the experiment, where a thin film is placed on the curved meniscus of an overfilled petri dish. (b) Composite image of a time series when the film is let go. The geometric mismatch between the sheet and the meniscus propels film towards the center.

the only relevant energies are due to gravity and surface tension:

$$U = U_{\text{gravity}} + \gamma A_{\text{free}} . \quad (32)$$

In this limit, the role of wrinkling is to allow the film to adopt an overall “gross shape” that may be doubly curved.

3.5 Simulation

Here we study this model numerically for general geometries using SURFACE EVOLVER [85]. In our simulations, the sheet and liquid are discretized with triangular meshes using the package *meshpy*, with a mesh length of 0.1. We pin a liquid meniscus on a circle of radius L with surface tension γ and density ρ . We control its volume V to change the height of the meniscus, h . The sheet is a disc of radius W , which is given zero bending modulus and a stretching modulus Y . Mesh edges in the sheet are allowed to contract with no energy cost, representing a coarse-grained description of small-scale wrinkling). We set $Y/\gamma = 10^{12}$

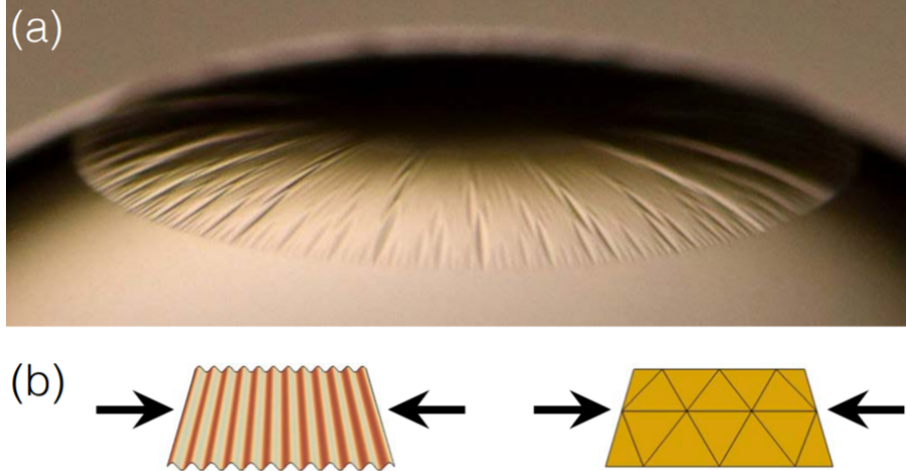


Figure 28: **Coarse-grained model for wrinkling** (a) A thin film forms wrinkles to adopt a doubly-curved shape. (b) We model this wrinkling in Surface Evolver using a triangular mesh where the edges may contract for free. This provides a suitable coarse-grained model of the effect of wrinkling.

to produce approximately inextensible behavior [82]. The Poisson's ratio of the film is:

$$\nu_{xz} = \nu_{yz} = 0, \nu_{xy} = \nu_{yx} = 0.8.$$

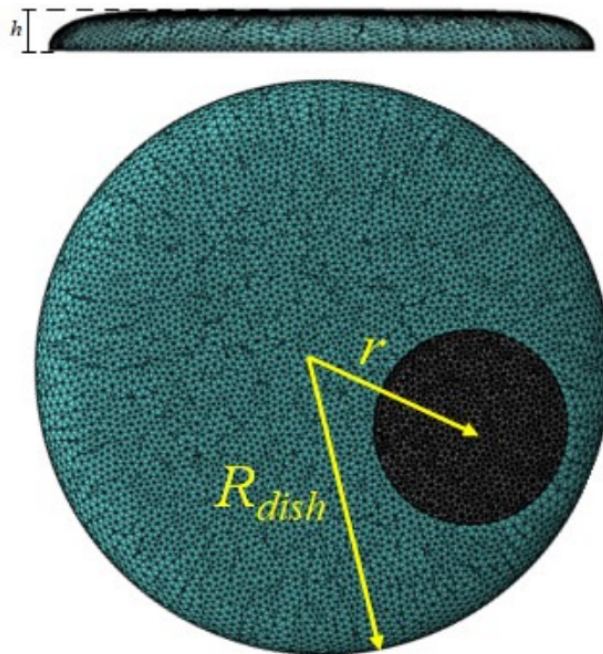


Figure 29: Side and top view of floating sheet system.

Our goal is to understand how curvature gradients on a liquid surface can drive the spontaneous motion of a thin solid across it. Thus, we perform a series of simulations where

the center of the sheet is held at a particular radial distance r from the center of the dish, and the system energy is allowed to relax to search for the global energy minimum.

3.6 Energy measurements

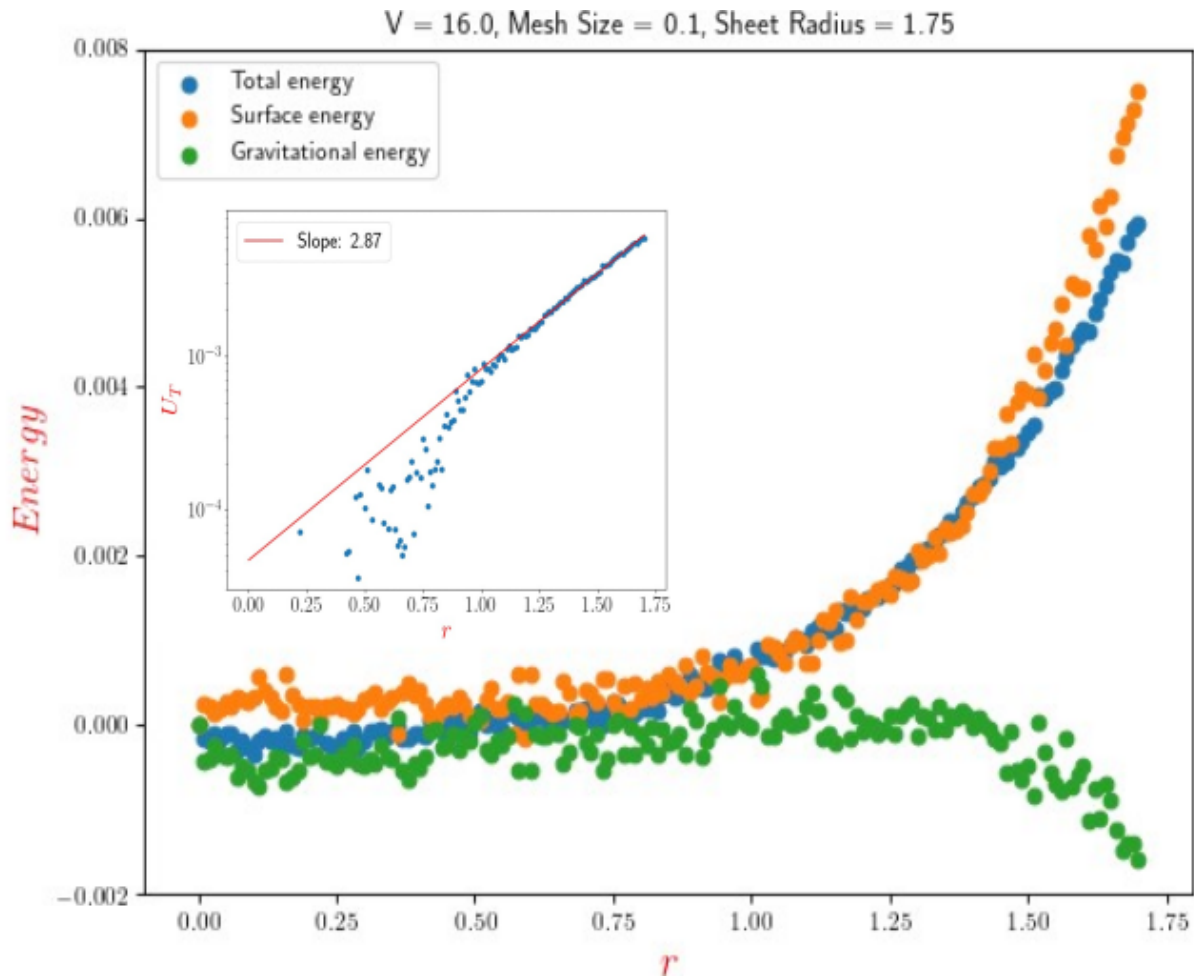


Figure 30: **Energy Plots:** Simulation results where the sheet is positioned at a distance r from the center of the dish. The system energy is comprised of surface and gravitational energy. The inset show that the total energy has an exponential dependence on the radial position.

Figure 30 shows the components of total energy. It consists of two components: the surface energy of the uncovered liquid and the gravitational energy of the liquid. At the curved edge where the sheet bends to wrap the curved surface of the liquid. The surface energy decreases as the sheet moves towards the center. However, the gravitational energy

decreases as we recede from the edge of liquid drop. The dominating energy is the surface energy and the gravitational energy and the total energy follows a similar trend and decreases exponentially as the circular sheet moves farther from the edge of the liquid drop, demonstrating the energetically favorable position for the sheet is at the center.

When U_{total} versus r is replotted in log-linear axis, we get a clear exponential trend. It is important to note that, this is an empirical finding and is not based on any developed theory. But it is worth noting that a liquid meniscus has an exponential height profile in the limit of small slopes, for a 1D problem, so it is natural to use ℓ_c as the length scale to compare $L - W - r$ with. We can fit the change in total energy with an exponential curve given by, $dU = A \exp^{-bx}$.

This represents the total energy of the system, which varies with the position of the sheet. Thus, we may convert it to a force on the sheet, by taking a derivative with respect to the position coordinate:

$$F_{drive} = \frac{\partial U}{\partial x}. \quad (33)$$

For large fluid viscosities, this driving force will be in balance with a drag force due to the shearing motion of the fluid, which we discuss now.

3.6.1 Drag model

In order to match our simulation velocity with the experiment, we are required to find a drag model relevant to our system. We will discuss only the viscous regime cases here. The drag experienced by the sheet while moving across an infinite viscous liquid, is given by Stokes drag [86],

$$F = \frac{16}{3} \mu W u. \quad (34)$$

This result is for a system with no boundaries; Ref. [87] used experiments to determine an empirical correction to this law, in the form of a multiplicative factor. In the situation where

there is a flat wall a distance H away from the film:

$$F = \frac{16}{3}\mu W u \left(1 + 0.81 \left(\frac{W}{H} \right)^{1.074} \right). \quad (35)$$

3.7 Comparison to experiment

3.7.1 Non-Dimensionalization

In order to compare the simulation results to the experiments, we need to identify the correct parameters that non-dimensionalize the physical system. In this section, primed parameters indicate parameters for our simulation, while unprimed parameters were taken directly from the experiment. We maintain the ratio of sheet/dish radius, as well as the capillary length value to nondimensionalize other simulation parameters. The dish radius for all experiments was 18.5mm, and we pick the $W = 4.76$ mm to equal a $W' = 1$ non-dimensional units.

The capillary length is given by

$$l_c = \sqrt{\frac{\gamma}{\rho g}} \quad (36)$$

Dividing it by the sheet radius W we get,

$$\frac{l_c}{W} = \frac{l'_c}{W'} = \frac{1}{W'} \sqrt{\left(\frac{\gamma'}{\rho' g'} \right)} \quad (37)$$

We set surface tension γ' and liquid density ρ' to be 1. From here, we can calculate the simulation value for g , the gravity constant.

$$0.146 = \frac{1}{3.887} \sqrt{\left(\frac{1}{g'} \right)}$$

$$0.567 = \sqrt{\frac{1}{g'}}$$

Finally,

$$g' = 3.108$$

We also non-dimensionalize the liquid volume using the sheet radius, W . For example, to non-dimensionalize the experiment where the liquid volume $V = 2.807$ we do the following:

$$\frac{V}{W^3} = \frac{V'}{W'^3} \quad (38)$$

Thus,

$$V' = 26.03$$

We also can find the capillary length for our simulation l'_c from equation 1. Substituting gravity, density and surface tension for our simulation we get,

$$l'_c = \sqrt{\frac{1}{3.28}}$$

Therefore,

$$l'_c = 0.55.$$

Thus tabling these parameters,

| | Experiment | Simulation | Non-dimensionalized by: |
|------------------------------|-------------------------|------------|-------------------------|
| Sheet Radius (W) | 4.76 mm | 1 | W |
| Dish Radius (L_D) | 18.5 mm | 3.886 | W |
| Drop Volume (V) | 2.80725 cm ³ | 26.029 | W |
| Surface tension (γ) | 73 mN/m | 1 | γ |
| Liquid Density (ρ) | 0.997 kg/m ³ | 1 | ρ |
| Gravity (g) | 9.81 m/s ² | 3.108 | W, γ, ρ |
| Capillary Length (l_c) | 2.7 mm | 0.567 | W, γ, ρ |

Table 3: Non-dimensionalization of experimental parameters for use in the simulations.

3.7.2 Inextensible limit

In order to do compute velocity comparable to the experimental velocity, we have non-dimensionalized the physical parameters and used them in our simulation. We did this at first for viscosity $\mu = 48cp$. Then we get the energy dU vs the $(l - r)/l_c$. From that we obtain,

$$U(x) = ce^{m\frac{(L-x)}{l_c}}. \quad (39)$$

$$F_{drive} = \frac{\delta U}{\delta x} \quad (40)$$

But,

$$F_{drive} = F_{drag}$$

The latest drag force is given by eqn. 35. Calculating the velocity,

$$u(x) = \frac{3}{16}mc \frac{1}{\mu W l_c (1 + 0.81(\frac{W}{H})^{1.074})} \exp \frac{m(L-x)}{l_c} \quad (41)$$

However, in order to match the velocity obtained from fitting the simulation energy with the experimental velocity data, we need to multiply equation 41 with a ratio:

$$u(x) = \frac{3}{16}mc \frac{\gamma_{exp} W_{exp}^2}{\gamma_{sim} W_{sim}^2} \frac{1}{\mu W l_c (1 + 0.81(\frac{W}{H})^{1.074})} \exp \frac{m(L-x)}{l_c} \quad (42)$$

To calculate the ratio, let's plug in the parameters: $\gamma_{sim} = 0.88$, $W_{sim} = 1$, $\gamma_{exp} = 0.0659$ N/m, $W_{exp} = 0.00442$ m, $\rho_{sim} = 1$, $\rho_{exp} = 1209 \frac{kg}{m^3}$, $g_{sim} = 3.095$, $g_{exp} = 9.81 \frac{m}{s^2}$.

Plugging in this values in equation 17,

$$u(x) = (1.463 \times 10^{-6}) \frac{3}{16}mc \frac{1}{\mu W l_c (1 + 0.81(\frac{W}{H})^{1.074})} \exp \frac{m(L-x)}{l_c} \quad (43)$$

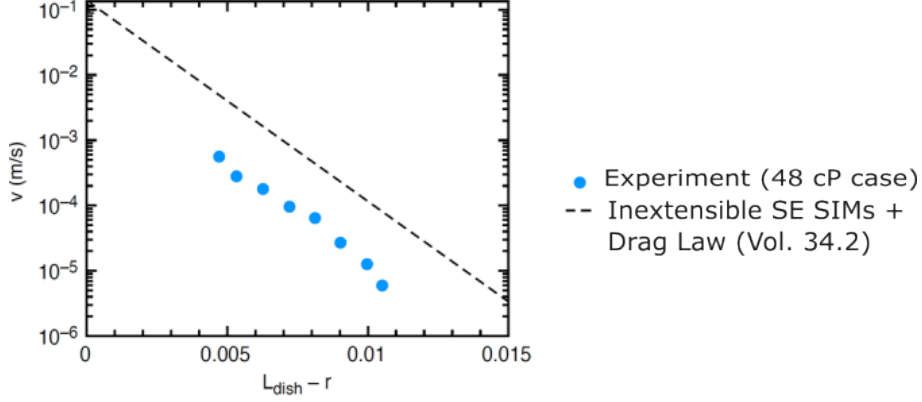


Figure 31: Comparing velocity derived from the inextensible film simulation with the drag law shows discrepancy with experimental results.

Now the other unit conversion,

$$u(x) = \frac{3}{16} mc \frac{\rho_{exp} g_{sim} W_{exp}^4}{\rho_{sim} g_{sim} W_{sim}^4} \frac{1}{\mu W l_c (1 + 0.81 (\frac{W}{H})^{1.074})} \exp \frac{m(L-x)}{l_c} \quad (44)$$

Plugging in the values,

$$u(x) = (1.463 \times 10^{-6}) \frac{3}{16} mc \frac{1}{\mu W (1 + 0.81 (\frac{W}{H})^{1.074})} \exp \frac{m(L-x)}{l_c} \quad (45)$$

Figure 31 shows that the simulation does not capture the experimental data. As we will show next, the small but finite stretching of the sheet in the experiments makes a large difference on the dynamics of the sheet. In the next section, we update our model to include the stretching of the film.

3.7.3 Finite stretching in films

The same simulation approach allows us to use a finite Y , and now we measure $U_{total} = U_{grav} + U_{surface} + U_{stretch}$:

Nevertheless, even small in-plane strains can be important when the imposed curvature of the liquid is similarly small. Indeed, when a circular polymer film is placed on a curved

Volume = 20.0, Meshsize = 0.1, SheetRadius = 1.0

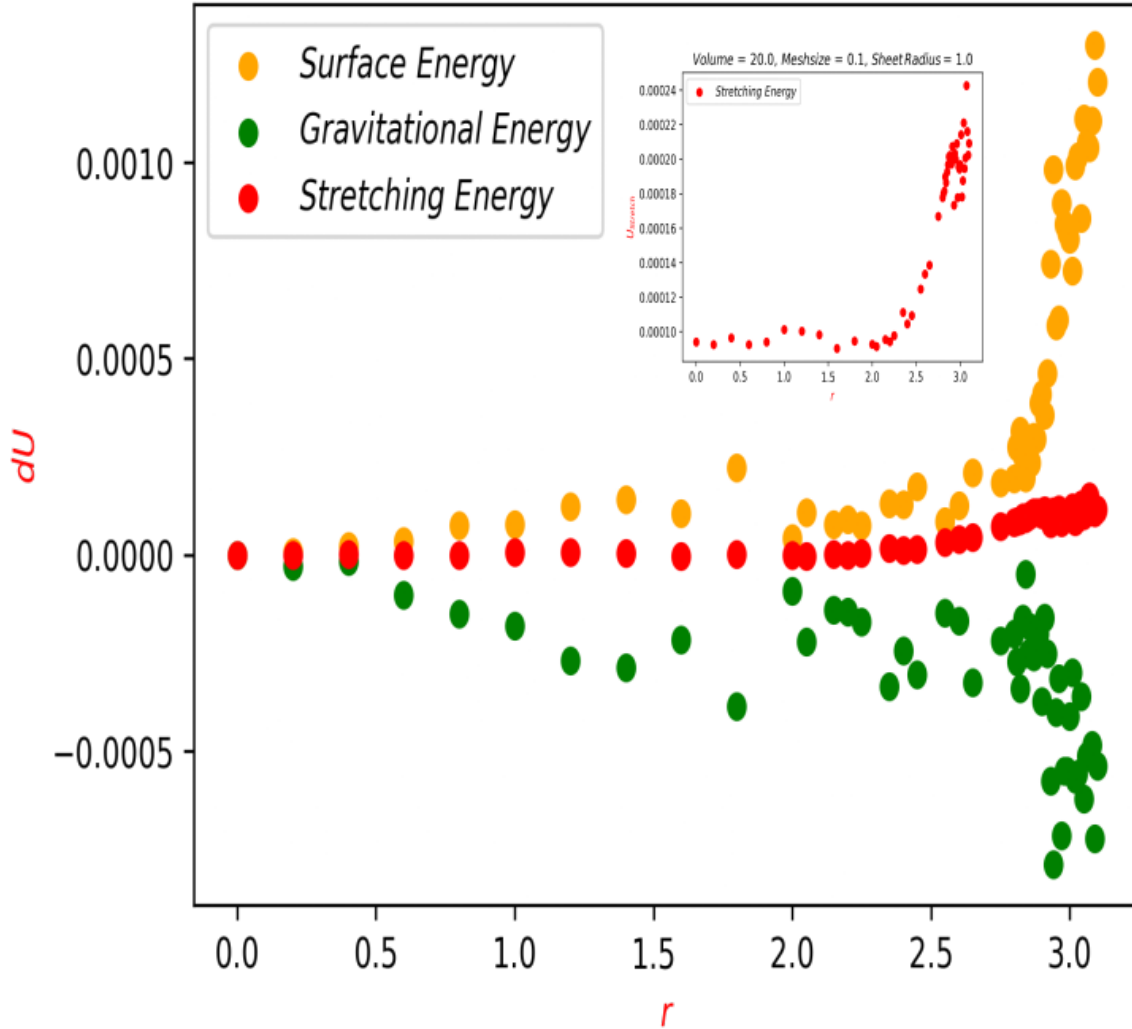


Figure 32: **Simulation results where the finitely stretchable sheet is positioned at a distance r from the center of the dish:** The system energy is comprised of surface, gravitational and stretching energy. The inset shows the stretching energy separately to show its exponential growing trend with the radial position from center to the edge.

liquid interface, radial wrinkles develop around the boundary of the film to accommodate the imposed Gaussian curvature, while an inner “core” of the film is unwrinkled [20]. The existence of positive Gaussian curvature in this core, in the absence of wrinkling, signals a small but finite stretching of the film. We show that this finite stretching plays a significant

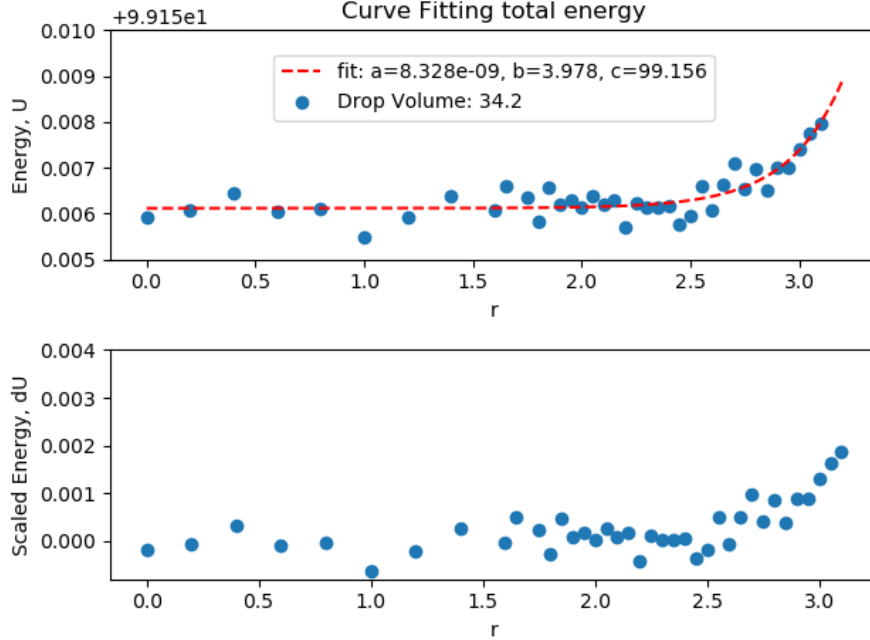


Figure 33: The total energy is rescaled by subtracting the total energy with the $U(0) = a + c$, $dU = U - U(0)$

role in determining the energy of the system. In this case, the system energy is given by:

$$U = U_{\text{gravity}} + \gamma A_{\text{free}} + U_{\text{stretch}} , \quad (46)$$

where U_{stretch} is the elastic stretching energy stored in the sheet.

3.7.3.1 Scaling the total energy and velocity comparison

In order to simulate a sheet with finite stretching modulus, we must select an appropriately scaled stretching modulus for our films. The stretching modulus, Y , is non-dimensionalized by the surface tension, γ . Thus, we seek to match:

$$\frac{Y}{\gamma} = \frac{Y'}{\gamma'} , \quad (47)$$

where in the experiments, $Y = Et$. (In contrast, there is no concept of thickness in the simulations, so the value Y' is the only relevant variable there.)

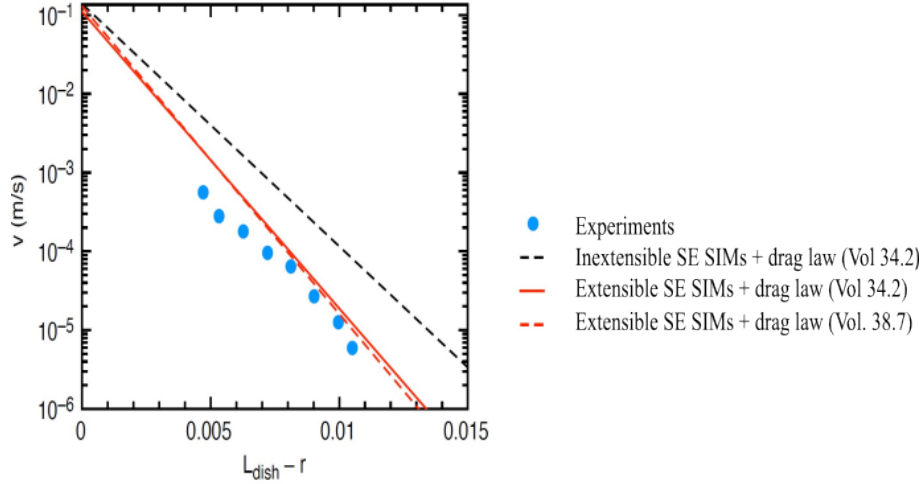


Figure 34: Comparing velocity derived from the finitely stretchable film with the drag law shows good agreement with experimental results. The inextensible film simulations are also shown for comparing how much the velocity can decrease on introducing finite stretching.

Given $E = 3.4$ GPa, $t = 120$ nm, $\gamma = 0.06375$ N/m and $\gamma' = 1$ (from section 3.7.1), we find the stretching modulus to run our simulation as $Y' = 6400$. This is considerably smaller than the value used to probe the inextensible limit in the previous section ($Y' = 10^{10}$).

The formalism to derive the velocity as shown in section 3.7.2 is repeated and the predicted velocity is shown here. On examining the plot in figure 34, we see the finely stretched film velocity conforms well with the experimental result. Also, we observe the inextensible films are faster than the finitely stretchable film indicating ability of inextensible film can store more energy when pinned at a geometrically mismatched curvature. This confirms that the film has finite stretching and even a small stretching energy can drastically reduce the velocity of thin film. Since the parameters are extracted from the experiment, there were some concerns about the range of error in the volume measurement. Therefore, we plug in the highest and lowest volume measurement data from the same experiment and derive the corresponding simulation parameters. Figure 34 shows the range within which the volume is expected to vary and we see the velocity varies negligibly thereby reaffirming the agreement between the experiment and simulation.

3.8 Measuring the energy scalings

We seek an understanding of how the energy of the system depends quantitatively on the properties of the liquid and the sheet. The liquid has a surface tension γ and gravitational stiffness ρg that give rise to the capillary length $\ell_c = \sqrt{\gamma/(\rho g)}$. The liquid is pinned at a circular contact line of radius L and its height at the center is h . The sheet has a stretching modulus Y and radius W .

As we will show, our central result is an empirical scaling for the total energy of the system as a function of the radial position of the center of the film, r :

$$U(r) = f_1(\alpha) \frac{\gamma}{\sqrt{\ell_c}} \frac{h^{1.5} W^{1.75}}{L^{0.75}} \exp(-f_2(\alpha)(L - W - r)/\ell_c), \quad (48)$$

where $\alpha = \frac{Y}{\gamma} \frac{\sqrt{h}}{\ell_c^3} L^\delta W^\beta$ is a dimensionless ‘‘confinement’’ parameter that represents the ratio of geometric strain $\frac{\sqrt{h}}{\ell_c^3} L^\delta W^\beta$ and mechanically-induced strain $\frac{\gamma}{Y}$, and $f_1(\alpha)$, $f_2(\alpha)$ are functions that represent the form of the collapsed data. Notably, above a threshold stretching modulus, they both approach constant values so that $f_1(\alpha) = c_1$ and $f_2(\alpha) = c_2$ in the inextensible limit.

3.9 Stretchable vs Unstretchable films on liquid meniscus

From the previous section, it is clear that the velocity of the system varies with the film stretchability indicating this to be one of the factors affecting this geometry driven propulsion.

In this section, we will delve into all the different parameters that are used in our simulation and study their effect on the phenomena. To simplify this investigation, we divide this in two parts: First we study only the unstretchable films. We further delve into all the parameters varied for it: liquid volume, sheet radius, dish radius, surface tension of the liquid, density of the liquid and gravity.

3.9.1 Energy scaling

Our dominant energy values consist of two terms, gravitational and the surface tension:

$$U_T = U_{grav} + U_{surface} \quad (49)$$

Assuming some constant configuration of the system,

$$U_{grav} \propto \rho g \int_V z dV \quad (50)$$

and

$$U_{surface} \propto \gamma \int_{surface} dS \quad (51)$$

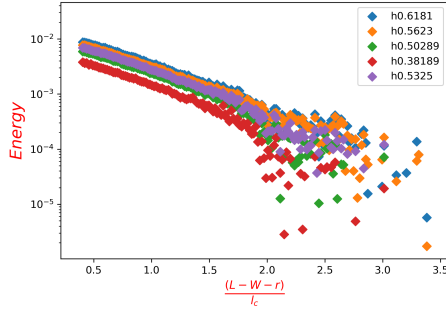
These integrals are of units m^4 and m^2 respectively.

We can construct the units for the energy separately for each in this way, or we can construct it in one product between the two energy coefficients raised to different powers. An example follows:

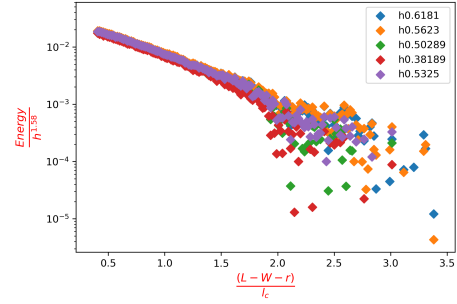
$$\begin{aligned} [U] &= \frac{kgm^2}{s^2} = [\gamma]^\alpha [\rho g]^\beta [\ell]^\delta \\ &= \left(\frac{N}{M}\right)^\alpha \left(\frac{kg}{m^2s^2}\right)^\beta (m)^\delta \\ &= \left(\frac{kg}{s^2}\right)^\alpha \left(\frac{kg}{m^2s^2}\right)^\beta (m)^\delta \end{aligned}$$

From this we can find two conditions that must be met, namely: $\alpha + \beta + \delta = -3$ and $\alpha + \beta = -1$. This necessitates that $\alpha = 3$ and $\delta = -2$. Then we have:

$$\begin{aligned} &= \left(\frac{kg}{s^2}\right)^3 \left(\frac{kg}{m^2s^2}\right)^{-4} (m)^{-2} \\ &= \frac{kg m^2 s^2}{s kg} = \frac{kgm^2}{s^2} \end{aligned}$$



(a) Plot showing overfill height variation



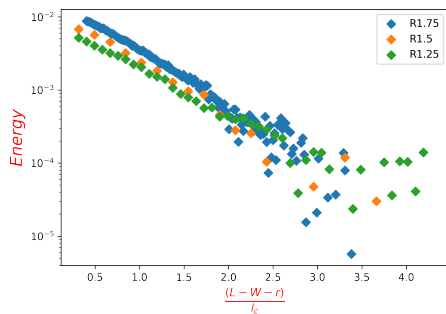
(b) Collapse figure for height variation

Figure 35: Figure showing height dependence

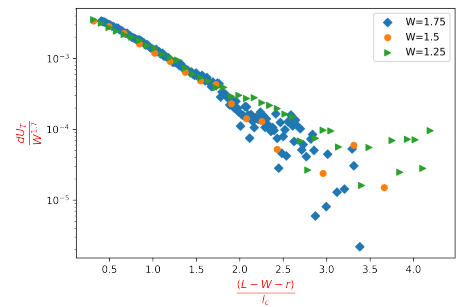
To find this equation that gives the total energy, we investigate all the physical variables in our model and study their dependence on total energy.

To investigate the contribution of overfill height to the total energy, we vary the volume of the liquid for this system and calculate the energy dependence of the system with the radial position of the sheet. While the volume is varied, we keep all the other parameters constant through different runs to isolate the dependency on volume. From figure 36, we can not only confirm that overfill height plays a part in energy of this model, but also give a quantitative exponent for the same.

Next the sheet radius of the film is varied while keeping all other observables constant. We found that larger sheets produce larger energy trends. We suspect this is because sheets covering more surface area produce larger curvature mismatch. Secondly, we found total energy also scales with W . The figure 36 shows the radius variation. While this scaling



(a) Plot showing sheet radius variation



(b) Collapse figure for Sheet radius variation W

Figure 36: Height dependence on total energy

exponents can be obtained through trial and error, we obtained this exponents through linear regression and compared it with manual fit to confirm the accuracy of the result.

After scaling both h and W component and finding their dependence, we explore all the other components by varying them in our model. We have four other exponents that were important parameters for our system. We deploy a multivariate linear regression model to calculate the exponents for all the parameters. The final plot is shown in figure 37 where all the energies are scaled by the calculated exponents along Y-axis and the X-axis is scaled by the capillary length, l_c .

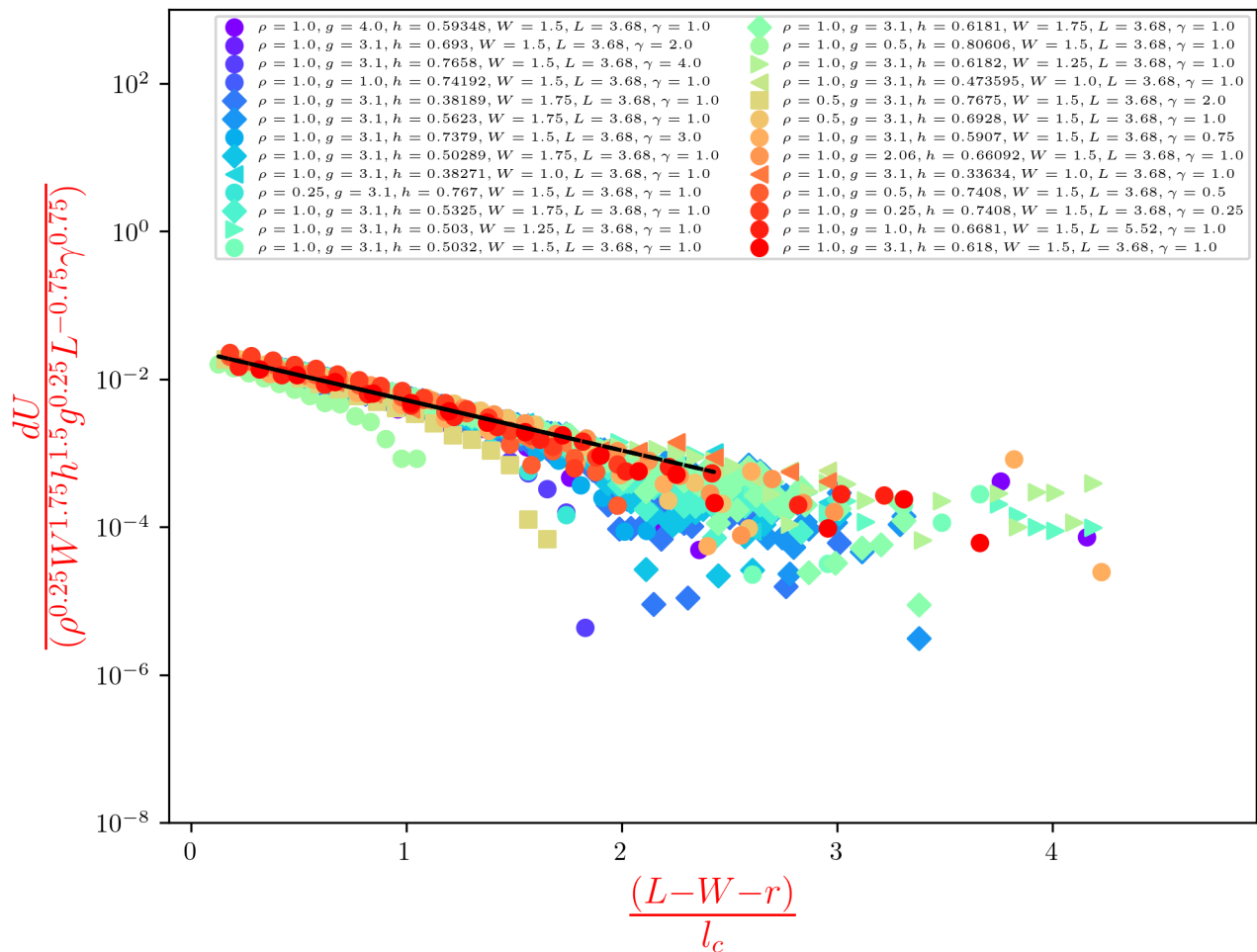


Figure 37: Data collapse across all relevant observables for this phenomenon.

We can fit this data to a function of the form

$$U'(x) = ce^{mx'}. \quad (52)$$

Thus,

$$\frac{dU(r)}{\rho^{0.25}W^{1.75}h^{1.5}g^{0.25}L^{-0.75}\gamma^{0.75}} = ce^{m\frac{(L-W-r)}{l_c}}. \quad (53)$$

$$dU(r) = c\rho^{0.25}W^{1.75}h^{1.5}g^{0.25}L^{-0.75}\gamma^{0.75}e^{m\frac{(L-W-r)}{l_c}}. \quad (54)$$

We map out the quantitative dependence of the system energy on the surface tension, density, and overflow-height of the liquid, the radius of the sheet, and the size of the dish. The denominator of Y-axis has the dimension of energy. Hence both X and Y axis are dimensionless axes demonstrating universality of this model. This equation not only shows that energy is lowest at the center as expected but also, quantify its dependence on all the observable of this system. Therefore, we developed complete empirical model for the unstretchable film predicting its dependence on all physical parameters relevant to this phenomena.

However, from our first section of this chapter it is clear that stretching play salient role in energy. Thus, we verify that by varying the stretching modulus of the sheet.

3.9.2 Stretchable film

Here we will study the effect of the stretching modulus on the system energy. Figure 37 shows the energy dependence on all other physical parameters affecting this system. Based on the model we see a power law dependence of these parameters to the energy. But we are not sure how the stretching modulus will affect the system energy.

To check their dependence of energy on young's modulus, we plot the coefficient A and B from the energy exponential function as a function of Y. The figure 38 shows an interesting phenomenon where we reduced stretching modulus systematically until we found this surprising trend at a particular stretching modulus, Y where the coefficient of the energy,

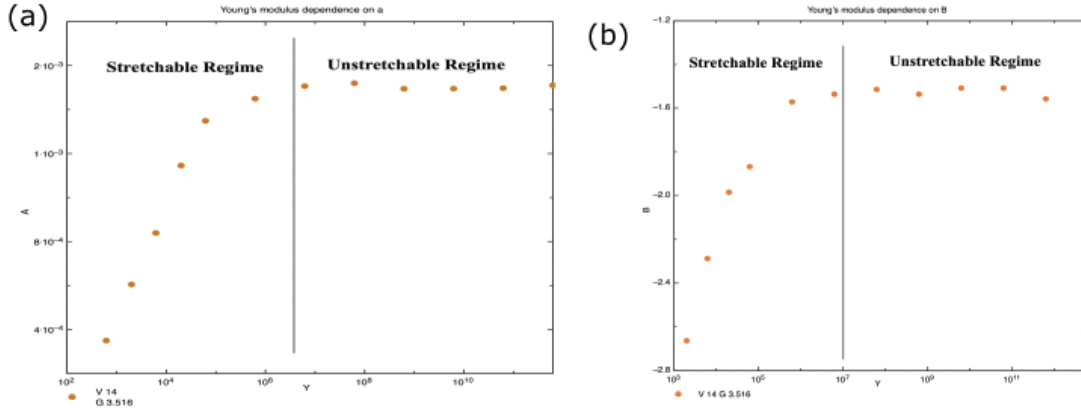


Figure 38: Energy coefficients from the equation $U(r) = A \exp Br$ are plotted against the stretching modulus Y . This shows that both A and B becomes constant on reaching a threshold Y .

A is no longer constant and reduces with the Y . This is interesting because the introduction of a small yet finite energy changes the energy in the system drastically. This gives rise to two separate regimes: a stretchable regime and an unstretchable regime.

We further checked if the observable of the system scales with the new “stretchable” regime. We vary the overfill height h and the gravity g for this system. Since A scales directly with the energy U ($U = A \exp Bx$) we use A to investigate the scaling exponents for Y . From figure 37, we already know the scaling exponents for energy in the “unstrechable” regime. Now we explore the scaling exponents for the “stretchable” regime. The scaling exponents for Y are found to be 0.5 with height and 1.5 with gravity. This collapse indicates universality of this phenomena.

4 Conclusion

4.1 Summary

This work investigated multi-scale pattern formation behaviours of thin-film under different settings and investigate its symmetry breaking phenomena.

In chapter 2, we studied symmetry breaking phenomena of crumples transitioning to

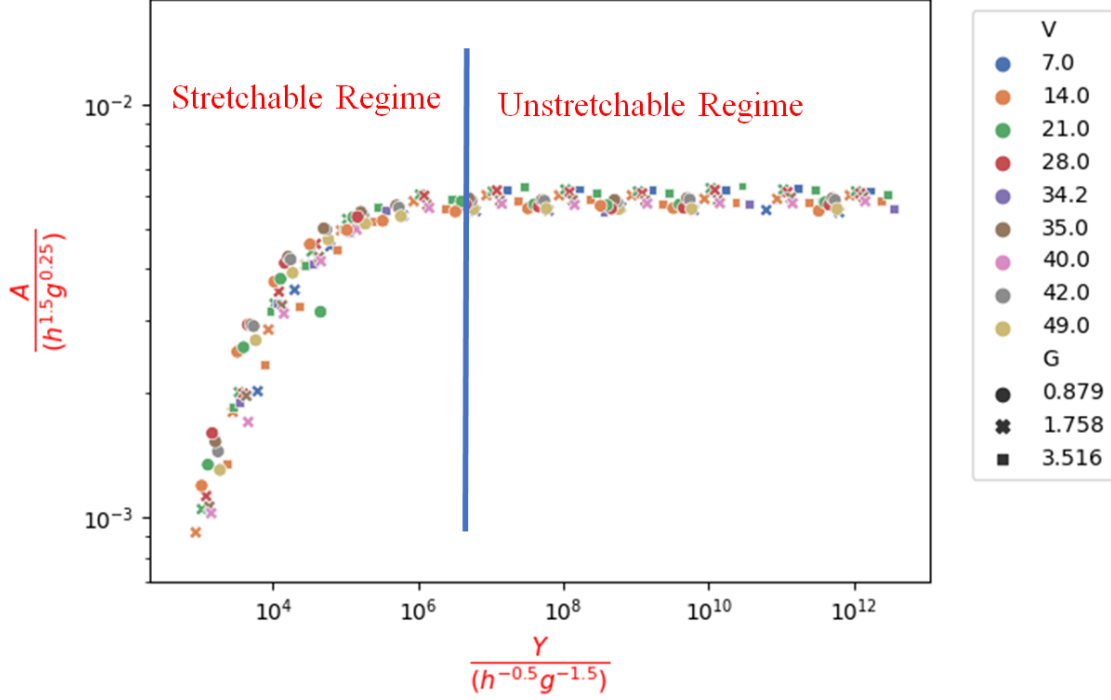


Figure 39: Data Collapse for all observable relevant to this phenomenon.

wrinkles in various geometries and length-scales. We have captured the universality of this phenomena through representing all these experiments in a phase diagram that can be represented by a threshold confinement factor α_{cr} . We also qualitatively studied the surface topography of crumples and wrinkles and show how localized high curvatures are embedded at the ends of crumples indicating stress focusing at lower pressure that eventually redistribute this stress over the membrane as it transition to wrinkles. We also found a scaling relationship for crumple length that can explain the length scale of crumples observed across three unique systems.

In the Chapter 3, we investigated thin film behaviour in a curvature mismatch setting. We compared the velocity obtained from our model to the experimentally derived velocity of the same system and have obtained good agreement. We have also identified how finite stretching can give rise to a very different energy with respect to velocity in an unstretchable film. We finally identified the power law dependence of various observable that play an important role in such systems. We have found the empirical law that govern films in such

system in the inextensible limit.

4.2 Future Directions

4.2.1 Behavior of d-cones under tensile stresses

King [21] observed the crumples with cusp-like structures at its end in his sheet on drop system evolve from wrinkled micro structures. On probing with profilometer he observed positive and negative gaussian curvature dipole focused at the cusp which made him suspect these structures to have d-cone like structures. However, he also observed that the stress is not strongly localized at the tips in his setup. He argued that radial tension is causing the stress to smoothen out in the cusp region. He predicted that with higher curvature of the drop, the stress will be more focused and these crumple structures will get sharper. However their experiment is unable to explore this due to experimental limitations.

In my experimental setting, I wanted to study the same. The advantage of my membrane system is our lateral tension is analogous to the radial tension in his setting, increases as the pressure in the membrane builds up. Hence our membranes can capture the onset of crumples that gradually smoothen out to smooth wrinkles as the lateral tension increases. We have studied the topography of the membrane using 3D scanner. This showed that the gaussian curvature at first is focused in the diamond shaped edges of the crumples. The preliminary results corroborate the observations described above by King [21]. The gaussian curvatures are initially sharply localized in the crumpled edges and as the pressure increases in the membrane the gaussian curvature starts delocalizing indicating that the stress is being distributed over the membrane.

Also, in our previous work [19], we have measured crumple length l_{cr} . From that we have an empirical formula measuring crumple length in various system settings. It is given by,

$$l_{cr} = l_{\parallel}^{0.4} R_{\parallel}^{0.6} (\sigma_{\parallel}/Y)^{0.3}$$

While this is an important piece of information that gives insight to the length of crumples, it still does not provide with the answer if crumples seen in my system has any relationship with the d-cone structures. To investigate this we need to look into the following: look closely at the Gaussian curvature at the stress focused points at lower pressures and obtain quantitative results to study the trends at the cusps, to investigate the length scale of these edges through curvature profile analysis and studying core length. [88]

We first investigate the length scale of the cusps at the crumpled edges. This regions are analogous to the crescent core region of d-cone.

4.2.1.1 Core length scaling

The core length [13] scaling for developable cone is given by eqn. 9 from sec. 1.0.2.1,

$$R_c \approx \left(\frac{E_b}{E_s} \right)^{\frac{1}{6}} \epsilon^{-p} R^{2/3};$$

The first term of this equation corresponds to the material properties, second part corresponds to the geometry of deformation and the last term relates to the length of moment arm of reaction force along the hoop of radius R.

First I identify the relevant parameters for my system. Based on gaussian curvature analysis, we know that the stress focusing occurs at the diamond-like edges of crumples which is comparable to the crescent core of D-cone which experiences the same. We measure core radius R_c of these edges for our system using ImageJ [52] to analyze the still images of crumples (see figure 40) I have measured the core radius of the crumples for varying membranes with thickness ranging from Square membranes of width, $D \ 10 < W < 31$ cm and thickness $15 < t < 222 \ \mu m$. The Young's modulus vary over a wide range ($2.0 < E < 1500$ MPa) as well for these experiments. Fig. 41 shows the data for R_c dependence on varying P . We observe in each experiment, the R_c reduces with increasing pressure. This is interesting observation since in a typical d-cone, the core radius radius reduces as the stress

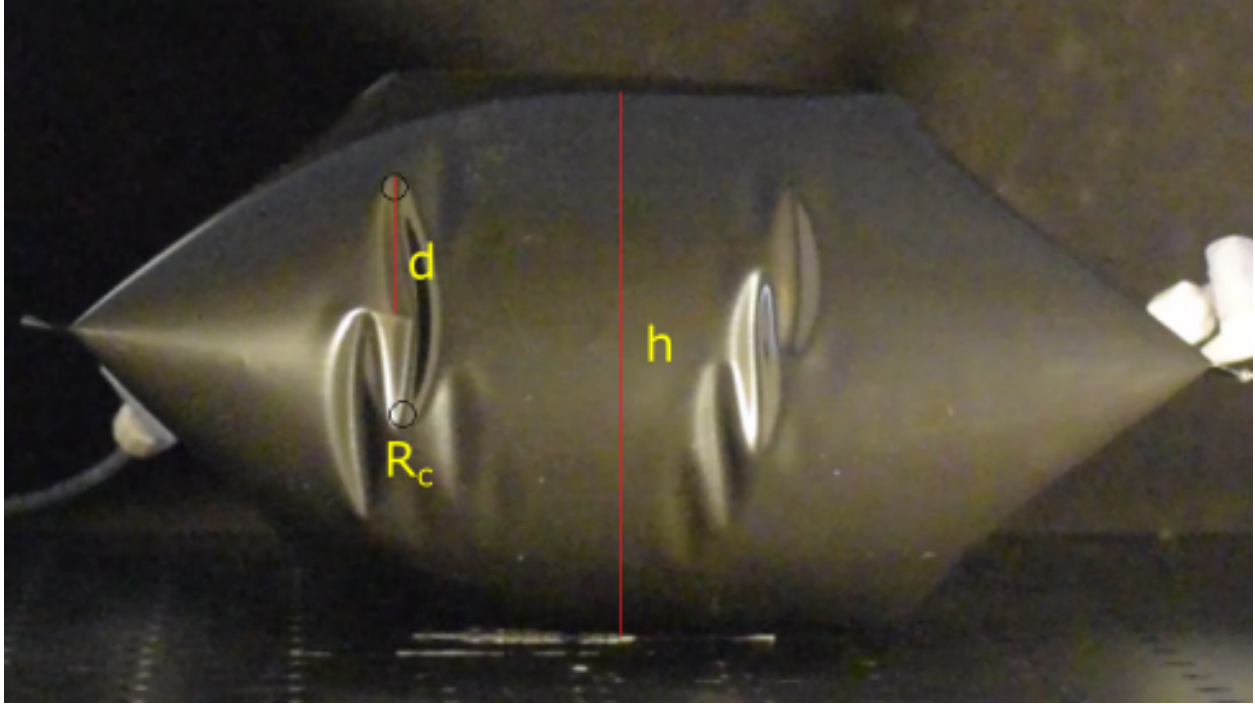


Figure 40: Introducing the crescent radius R_c that is being measured in this system to compare its scaling with a typical d-cone.

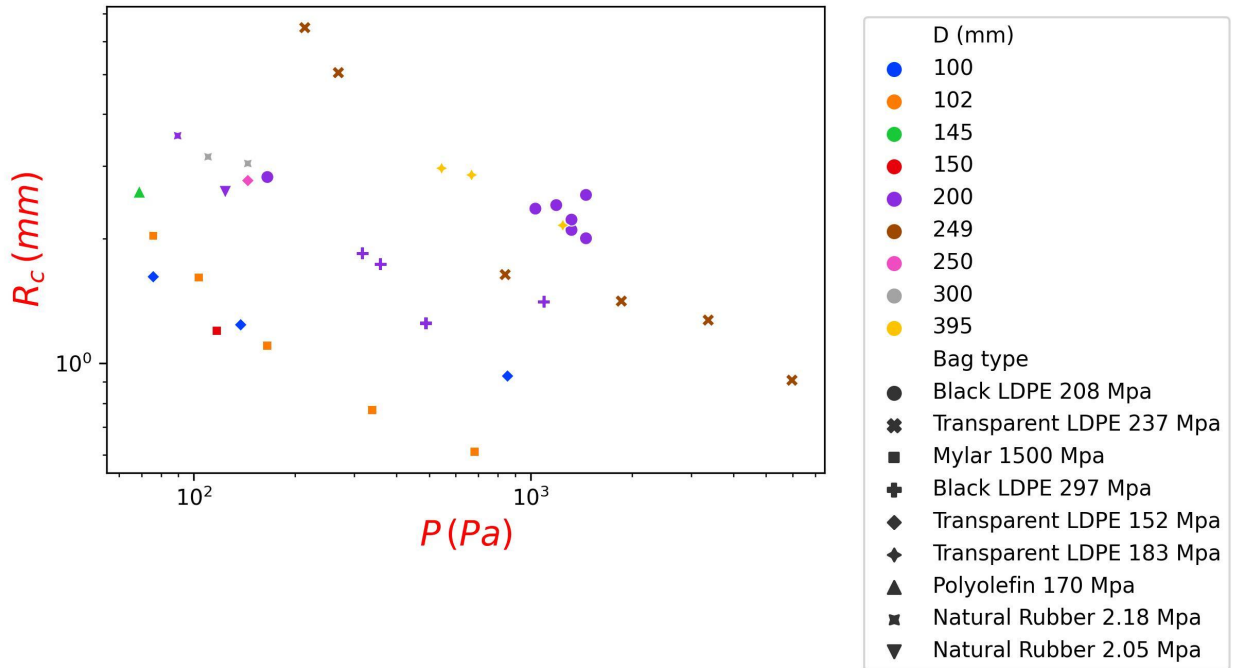


Figure 41: Cresecent radius R_c versus Pressure P .

localizes. But the opposite effect is observed here. But it is not surprising since unlike a typical d-cone, this membranes are under an increasing lateral tension.

We scale the y-axis with the dimension of the membrane and scale the x-axis with the strain on the membrane (PR_{\parallel}/Et) and the ratio of crumple length l_{cr} and the bag dimension D . From figure 42, we see that the data collapse pretty well when plotted with the new axes.

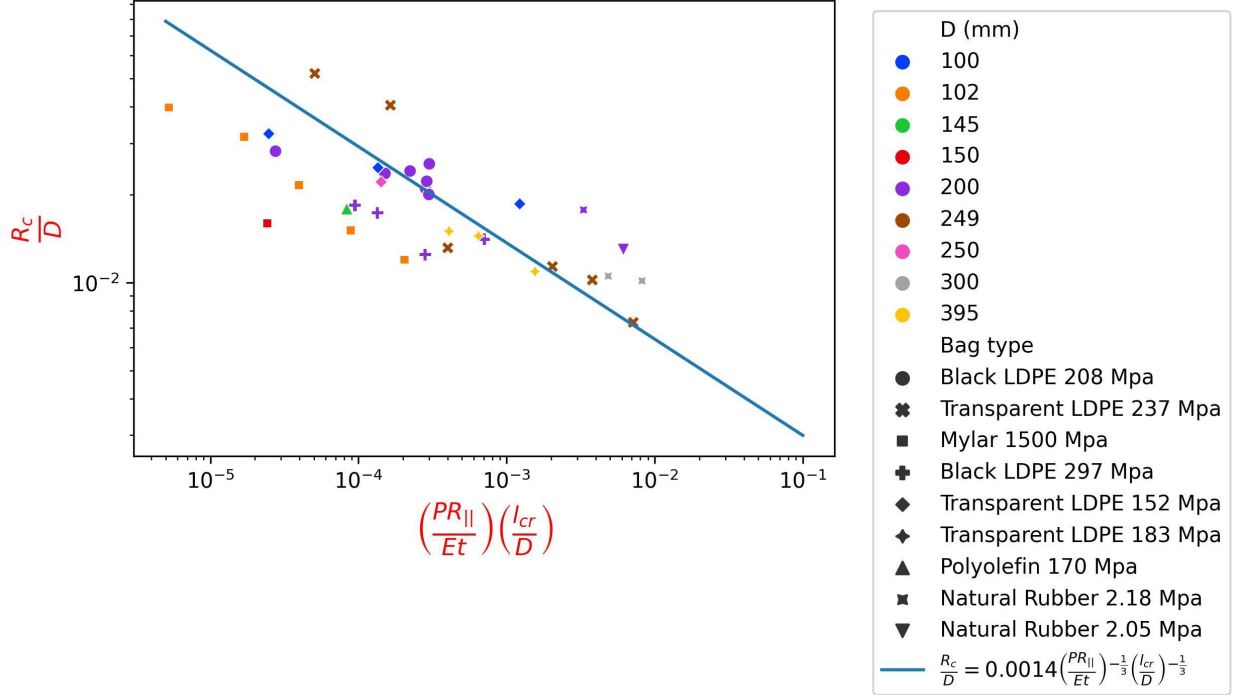


Figure 42: Scaled crescent radius $\frac{R_c}{D}$ versus scaled pressure $\left(\frac{PR_{\parallel}}{Et}\right) \left(\frac{l_{cr}}{D}\right)$.

This data can be fitted by the equation,

$$\frac{R_c}{D} = 0.0014 \left(\frac{PR_{\parallel}}{Et}\right)^{-\frac{1}{3}} \left(\frac{l_{cr}}{D}\right)^{-\frac{1}{3}} \quad (55)$$

The eqn. 55 can be rewritten as,

$$R_c = 0.0014 \left(\frac{Et}{PR_{\parallel}}\right)^{\frac{1}{3}} \left(\frac{l_{cr}}{D}\right)^{-\frac{1}{3}} D \quad (56)$$

Eqn. 56 gives an empirical scaling for the crescent core under applied stress.

4.2.2 Universal energy scaling for film on meniscus

While we are successful in building an empirical scaling equation for the system energy of thin floating film in the inextensible limit, some more work needs to be done to find the full picture for the systems with finitely stretchable film. So far, we have been successful in finding the dependence of thin film with gravity g and overflow height h (see sec. 3.9.2).

The final universal scaling energy will cover both inextensible and finitely stretchable system by eqn. 48,

$$U(r) = f_1(\alpha) \frac{\gamma}{\sqrt{\ell_c}} \frac{h^{1.5} W^{1.75}}{L^{0.75}} \exp(-f_2(\alpha)(L - W - r)/\ell_c) ,$$

where $\alpha = \frac{\gamma \sqrt{h}}{\ell_c^3} L^\delta W^\beta$ is a dimensionless “confinement” parameter. We are performing further simulation by only varying the length of the dish to isolate its dependence on the energy scaling. Once we obtain that, we can calculate the W scaling through dimensional analysis. Finally we will be able to derive the general scaling law for floating thin film system irrespective of stretchability of the film.

A Membranes: Fabrications and troubleshooting

The fabrication of membranes used in our experiments vary based on the materials. This appendix combines all of the methods along with the protocol to troubleshooting the problems arising from constructing membrane to inflating and performing the desired experiments.

A.1 Varying Shape of the membrane

The membrane shape was varied to study its effect on the deformations under applied stress.

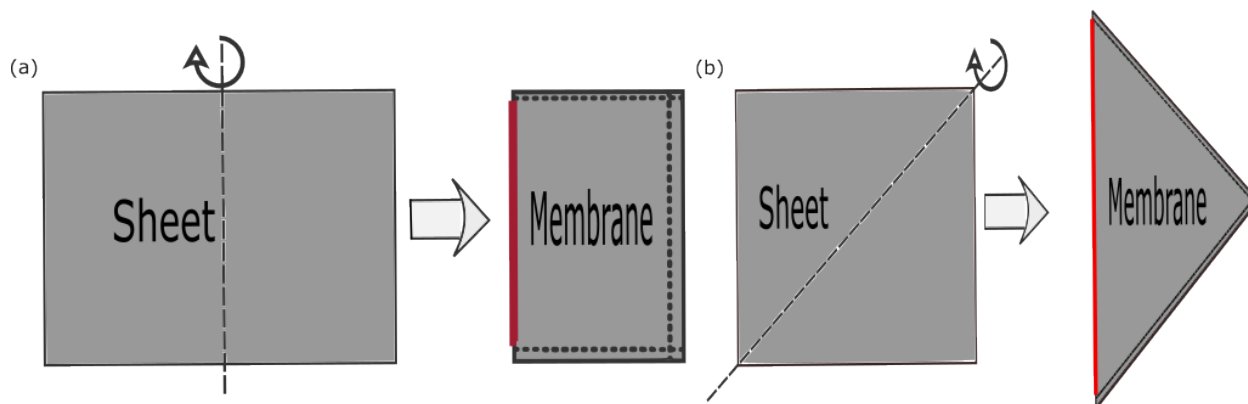


Figure 43: Cartoon showing the rectangular membrane construction out of a sheet. The dotted lines on the membrane denotes the seals. The red line denotes the surface used for conducting our experiments (a) Rectangular and square membrane construction (b) Triangular membrane construction.

A.1.1 Square and Rectangle

The square and rectangle are initial membrane shapes constructed for our experiment. First, we decide on the dimension of the membrane and the kind of material that we will be using for the said experiment. We cut a piece of the thin sheet from the roll that is approximately 1.5 times the dimension of the membrane. This is important since the excess material will be necessary to get an effective seal with a sizable border. We fold the material on itself along the latitudinal axis. A straight line along the breadth of the folded sheet is marked

by permanent marker. The sheet is sealed by heat impact seal along the straight line. The adjacent unsealed edge is measured and marked by the specified length dimension and sealed. Finally, the remaining edge along the breadth is marked and sealed along the specified dimension. The order of sealing is important here. If the last edge sealed is the edge along the length, chances of wrinkles forming at the sealed seam increases which in turn increases the chances of leak. If the membrane has a wide border, it is trimmed to approximately 0.5 inches on all sides to prevent any border effect on our result. After membrane is prepared, the dimension, material and thickness are written at the border.

A point to note here is the protocol to construct the membrane explained above is not universal. In particular, CHTP and natural rubber does not seal by the heat impact sealer since they have higher melting points than the temperature achievable by this tool. For these materials the protocol of folding and measuring remains same. However, CHTP and Natural rubber are sealed by epoxy adhesive and duct tape respectively. While working with these materials, we draw out the sides using ruler and a marker. When we use epoxy adhesive, we mix the epoxy resin and the hardener in 1 : 1 ratio well before using a stick to apply the adhesive along the marked lines. Then the sheet is folded along the lines and set aside to cure for about 15 minutes. The epoxy adhesive hardens very fast (≈ 4 minutes), which necessitate the sheet be scaled and ready for constructing the membrane. In order to fortify the edges, we also apply a layer of hot glue and let it rest and ready for creating the openings which will be discussed in section 4.3. For the natural rubber, we use duct tape to tape the edges.

A point that will apply to all membranes used in this experiment is: When the sheet is folded onto itself, care must be taken to not press down on the seal-free edge of the membrane to prevent introduction of any defects in this region.

A.1.2 Triangular

The method remains very similar to the section 4.2.1 except for the way the sheet is folded to obtain a triangular membrane. The initial thin sheet is folded diagonally (see figure 43b) and the same sealing protocol as described in section A.1.1 is followed.

A.1.3 Empanada

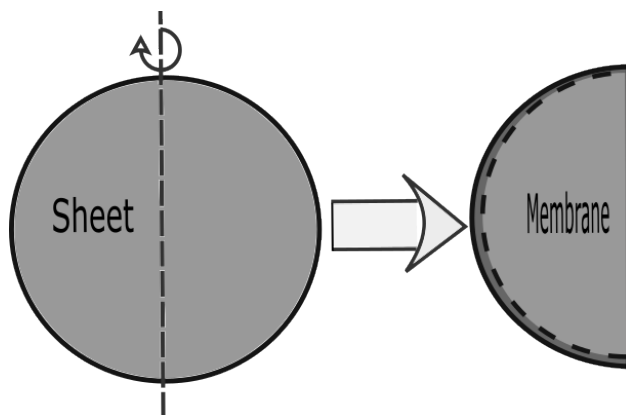


Figure 44: Cartoon showing the empanada shaped membrane construction out of a sheet. The dotted lines on the membrane denotes the seals. The red line denotes the surface used for conducting our experiments.

The method for sealing "Empanada" or a semi-circular membrane is different compared to the other shapes since its edge is rounded unlike the other shapes we have used in this experiment. First we cut a piece of thin sheet as per our specified need. We fold the sheet onto itself and used a compass to create a semi-circle of desired radius. It is very important not to press the needle onto the surfaces since it can puncture the surface and create a source for leak. Once the sheet is marked, we press the heat impact sealer in small discrete length along the marked edge.

A.1.4 Tetrahedral

The protocol is same as the triangular membrane until the final the edge needs to be sealed. Instead of simply sealing it along the remaining open edge, we pick the membrane by the

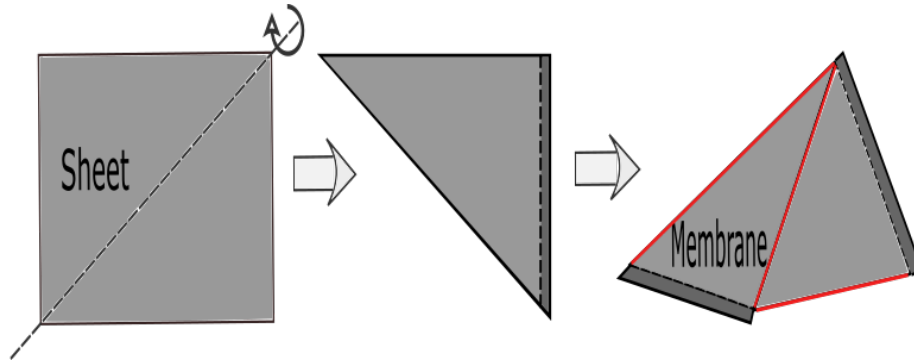


Figure 45: Cartoon showing the tetrahedral shaped membrane construction out of a sheet. The dotted lines on the membrane denotes the seals. The red line denotes the surface used for conducting our experiments.

sealed seam and press the membrane normally onto the seam and seal the edge such that the previous seam lies in the center of this seal.

A.2 Preparation of the openings in the membrane

After constructing the membranes we had to decide the best location to make openings in them to inflate them as well as measure the internal pressure instantaneously. We didn't make the opening adjacent to seal-free side of the membrane since that is where we will observe our desired transition. Hence we didn't want to disturb its boundary. Instead we chose to open the membrane on the opposing two corners since they are farthest from the observable region. We cut openings just barely big enough to insert the flexible pipes into it. This is very important since making opening larger than the pipe diameter increases the chances of leaking to a large degree. I found cutting the tip in an angle helped inserting the pipe in the holes comparable to the pipe diameter. Once the holes are cut we initially plugged the pipe and used the glue gun for most material (except for CHTP where we apply epoxy adhesive instead). However, I found adding a little glue to the tip before inserting it in the openings, gave us considerably less leakage which was observed using the method discussed in section 4.4.

Introducing holes in the rubber membranes, can be tricky after it is sealed with duct

tape. Hence when the membrane is made, we place the transparent elastic tube in between the overlapping membrane while it gets sealed. To ensure the region around tube is leak free, we apply hot glue to strengthen the seal.

A.3 Troubleshooting

To make sure that the membrane is not leaking, I performed a leak test by filling up a large beaker or a bowl with water and dip all the edges of the membrane especially the reinforced points (regions where the pipes has been inserted) after it has been inflated. If no bubble forms in this regions when placed under water, it confirms that the the membrane is leak-proof and ready for experiments. This check is particularly important while using this membranes for topographical studies since, 3D modelling requires this membrane to hold its pressure constant for over an hour while it is mounted on the 3D scanner and its surface topography is modelled.

A.4 Inflating membrane

At the nascent stage of this project we inflated membranes by orally blowing air through the pipe but that wasn't a long term solution since it was difficult to control the influx of air. We found an easier solution for inflating the membrane using the pressurized air cans. However, the membrane needs to be inflated quasi-statically to allow the microstructural deformations develop on the membrane gradually. This is a difficult process with air cans since influx of air in the system needs to be managed manually. Over time, I realized the best way of keeping the internal pressure of the membrane steady is by pressing the trigger very slightly maintaining a steady influx of air such that the inflation of these membranes occur very slowly. This still requires some practice especially if the intermediate deformation shapes needs to be measured.

A.5 Measuring Thickness

The materials used for this project comes from McMaster website where they typically have their thickness tabulated. However, since thickness plays an important role in the final calculations for our empirical model, we measure them in the lab using screw gauge for higher precision. A piece of the sample sheet is cut and folded 4 to 8 times on itself and this is placed between the anvil and the spindle of the screw gauge. The measured data is divided by the number of folds in the sheet to obtain the thickness of the sheet. This method is employed to reduce the inaccuracy in measuring lower dimensions. The error in its measurement is taken equal to the least count of the screw gauge which is useful for calculating the error bar for our model.

A.6 Measuring Young's Modulus

We have used tensile tester to measure the Young's modulus, Y for each material used in our system. We standardized the sample size to be 2" X 0.5" dimension strips. However, some of the same material strip curl up and are difficult to mount. Moreover, to prevent the strips from experiencing any plastic effect, we placed the prepared strips in between glass slides to prevent any creases. Initially when the samples were mounted, we found that the samples sometimes had some angular tension due to mounting error. To circumvent this issue, we keep the sample inside the glass while it is mounted. We insert the strip of the sample outside of glass in each clamps before removing the glass slides. This is done to prevent introduction of angular torsion. This gave accurate reproducible results used for our study.

A.7 Lighting

Lighting in these experiments plays an important part in the ability to see the surface deformations distinctly. Since most of the material used were opaque, having a lighted background didn't help in highlighting the microstructures. The experiments were run in

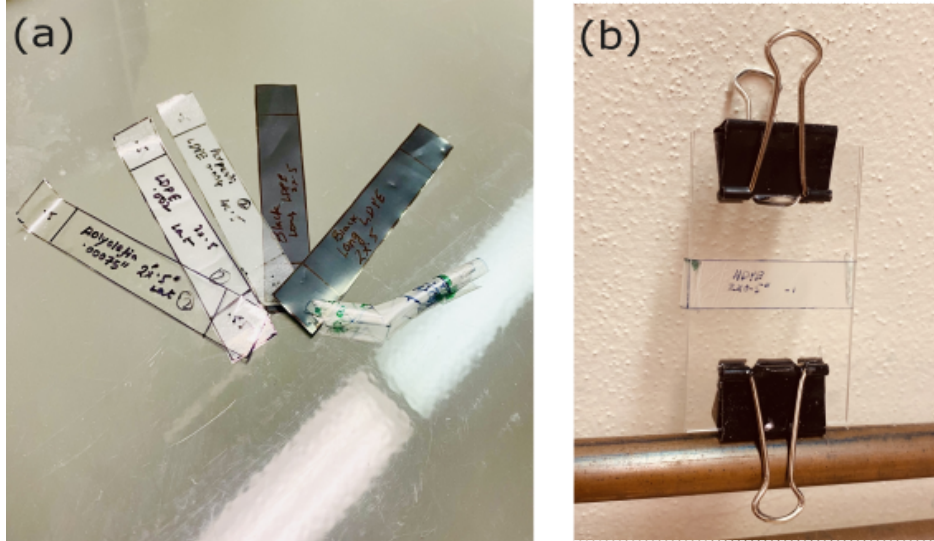


Figure 46: **Tensile testing samples:** (a) Prepared samples of various materials. You can notice how the sample on the left curls on itself making it difficult to mount (b) Sample is placed between glass slides to prevent creases and help in the mounting process.

dark room with two light source at 45° angle. One light source is a square LED studio panel light on a stand that was adjusted to the same level as the experiment. It is also fitted with a smooth pattern light diffuser panel to soften the LED light and reduce harsh shadows. On the other side, we fix a led light bulb on a stand. This bulb is adjusted such that the light is a little above the membrane at a diagonal position with the light falling directly on the surface of interest. This helps the light to reflect well from the microstructures on the surface.

A.8 Camera and Image Analysis

The camera used for the experiments is Nikon D5300 model. The camera is placed on a tripod on level with the experimental setup. The legs of the tripod are levelled. The camera is adjusted to best focus on the seamless edge placed at the front by modulating the aperture.

All the videos of the experiments are used for finding quantitative data. At first, we identify the point of transition for the membrane from wrinkle to crumple from the video. We save this frame and use Fiji software to extract the radius of curvature, R_\perp along the

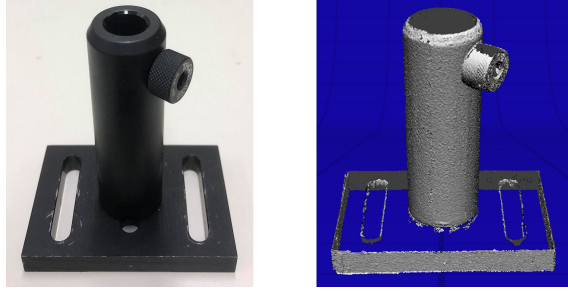


Figure 47: **Scanner Calibration:** Cylindrical post used as a sample object for calibration along with its scanned output

longitudinal axis and length of crumples l_{\perp} . Since the images don't have universal units, we determine the measurement by choosing an object in frame with known length as frame of reference for all the subsequent measurement. The frame of reference used in our experiment was the height of the digital dial screen (20 mm).

B A Guide to the 3D Scanning and analysis

3D scanning is performed using the Next Engine scanner model: . The scanner comprises of two parts: the scanning laser equipment and the mounting stage for the sample.

The scanner can do a complete scan of an object or a "bracket scan" that will only capture the object within 180° range. Since our region of interest is only one side of the membrane, we need only a bracket scan for our sample. To capture the best result bracket scan does the surface scanning in three steps and angles: with object placed perpendicularly from the scan and from two different angles from either sides.

We measured the dimensions of the post using vernier calipers. This data was then compared with the values calculated from the scanned image. We found that when the sample was placed at the distance of 9.5" from the scanner, the error was between 0.5–2.3%, showing high precision in its measurement. We calibrate the scanner and analysis code on the smooth metal cylinder, yields spatial fluctuations in the Gaussian curvature on the order of 0.01 cm^2 , which is one indicator of the measurement precision.

B.1 Data Cleanup and extraction

After the scan is completed, it gets automatically stitched together to form the complete scanned membrane. However, we preferred doing it manually since it gave better alignment among the three scans from different angles. In order to do that, we first unstitch the three scans and take two scans at a time and put pins at the matching point on both scans. We put at least three such pins on each scans relative to the others and manually stitch them together for the complete scan. After obtaining the complete scan, we trim the surface to remove points lying outside of membrane surface and excess materials that need to be deleted to clean the data for analysis. The unwanted points are selected using the trimming tool and deleted to obtain the final result.

After the data cleanup, we extract the data in “.xyz” format, which contain the three dimensional Cartesian coordinates of the scanned membrane.

B.2 Data Analysis

The data analysis is done by taking extracted coordinates to plot the height map at the crumple region to observe data using ProFit. We also investigate the Gaussian and Mean curvatures of our system. This was initially performed using the python code written by Z. Schrecengost in our group which I have since modified for other analysis discussed below. While our initial results with this code gave us good result, I wanted to crosscheck the results obtained from this program with other available methods. I have used a software called “Cloud Compare” [89]. The results are consistent with each other. However, gaussian curvature in “ Cloud Compare” is unsigned. Thus we stick to the python code for the curvature analysis.

C Surface Evolver

C.1 Wrinkling

Wrinkling occurs in the interfacial plastic film since it is energetically cheaper than stretching at a geometrically incompatible interface. In order to mimic this physical process, we use “relaxed_elastic”, one of the surface evolver method where the compression energy is made zero to encourage wrinkling.

Using the Cauchy-Green stress tensor,

$$C = \frac{1}{2}(FQ - I)$$

where Q is the inverse of the unstrained gram matrix and F is the strained gram matrix. The corresponding energy density is given by,

$$\left(\frac{1}{2(1+\nu)}(Tr(C^2)) + \frac{\nu * (TrC)^2}{(1 - (dim - 1) * \nu)} \right)$$

Where ν is the Poisson ratio for the thin film.

C.2 Choice of Poisson’s ratio

Thermodynamics restricts the permissible values of the Poisson’s ratio for an equilibrium isotropic 3D solid to lie between -1 and 0.5 . However, the default Poisson’s ratio in Surface evolver is set at 0.8 . This is permitted because we are working with a 2D elastic model, for which there is assumed to be no coupling between the x and z deformations (or between the y and z deformations) so that ν refers to the coupling of the x and y deformations only. For example, if such a solid is incompressible, it will have a “planar” Poisson’s ratio of $\nu = 1$.

Other values of ν are permitted as well. Hooke’s law in two dimensions can be written

as:

$$\sigma_{ij} = \frac{Y}{(1 + \nu)} \left(\epsilon_{ij} + \frac{\nu}{(1 - \nu)} (\epsilon_{xx} + \epsilon_{yy}) \delta_{ij} \right) \quad (57)$$

where $i, j \in x, y$. This relation is well behaved for any $-1 < \nu < 1$.

A large portion of our simulations probe the inextensible limit, by using extremely large values of $Y/\gamma \sim 10^{12}$. For those simulations, we used the default planar Poisson's ratio value of $\nu = 0.8$. In this limit, the numerical value of the Poisson's ratio is inconsequential, since the material undergoes negligible stretching deformations. In particular, all terms in Eq. 57 involving ϵ_{ij} vanish in the limit that $\sigma_{ij}/Y \rightarrow 0$, regardless of the value of ν .

In other simulations, we sought to model the behaviors under finite stretching. Here, the Poisson's ratio becomes relevant and needs to be chosen to model the deformation of the material under finite tensile stresses. The Poisson's ratio of polystyrene film used in the experiments is 0.34. Hence, we chose that as our planar Poisson's ratio in our Surface Evolver simulations that model the finite-stretching case.

C.3 Gradient Descent

Surface Evolver uses iterative method to optimize the energy by calculating the gradient of energy and consequently moving each vertex towards the direction of the negative gradient times the multiplier factor called "scale". A typical gradient descent iteration in surface evolver first calculates the force vector at each vertex obtained from the gradient of the total energy including the vertex with constraints, saves the current vertex position, finds the optimal scale factor that need to be multiplied by the direction of motion that is used to displace each vertex. All the constraints are then enforced and any vertices violating that will be projected to the constrains. Finally, the new energies, volumes are calculated are calculated and printed. These steps are repeated as necessary. But this alone would be enough to prove convergence since this is a first order method.

However, gradient descent is not very time efficient and it can keep zig-zaging in the

same energy valley without reaching the optimal energy. This is improved by implementing conjugate gradient descent in our optimization.

C.4 Adding Gravity

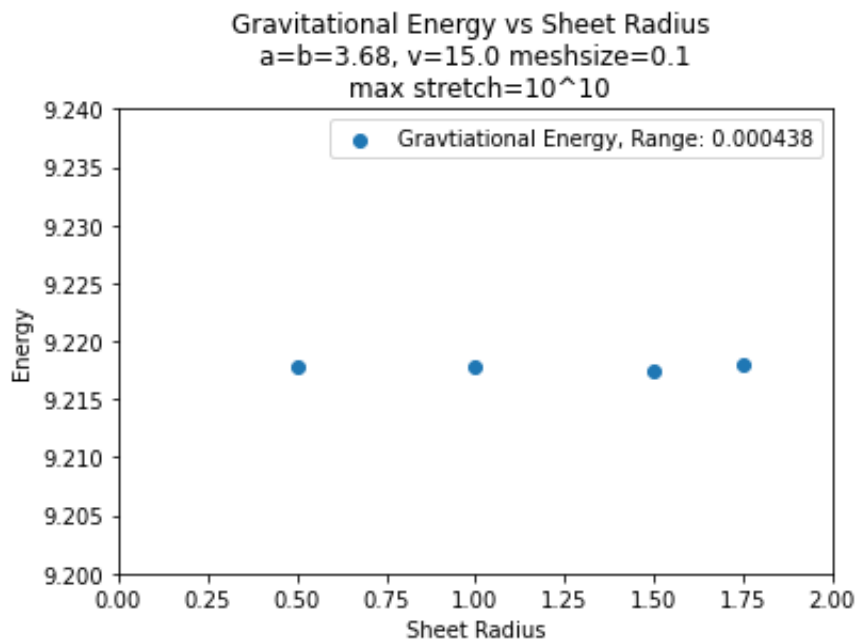


Figure 48: **Systematic check:** Comparing gravitational energy of systems with varying sheet size. The sheet is located on the central flat portion of the liquid, so that it should not change the height profile of the liquid as we vary its radius, and the gravitational energy should not change. The results validate this check.

We model the experiment conducted by Ripp. et al., by adding density to the Body of liquid in the system. The force of gravity is enforced through a density parameter that applies to all meshing facets that belong to the droplet of water.

$$U_g = \iint_{body\ surface} G \rho \frac{z^2}{2} \vec{k} \cdot \vec{dS}$$

Gravity can be added to surface evolver with the command “*gravity constant*” followed by the assigned value of gravity. The other way to add gravity is by the command “*gravity method*”. Both these methods worked identically hence we chose to go with the command “*gravity constant*”

to standardize the protocol.

To ensure that the volume under the sheet is considered dense by the model, we perform a control test where we vary the sheet size while holding other parameters constant. If the volume under the sheet is in fact considered dense, then this change should not affect the gravitational energy of the system. While the sheet size might affect the gross shape of the droplet, which might force some of the water to a higher or lower height, the difference in energy should not be significant compared to the cylinder of volume below the sheet.

C.5 The Ansatz Problem and Volume iteration (Voliter)

Initial model uses an ansatz for the gross shape of the droplet describing it as the cap of a sphere. This ansatz is a perfectly reasonable approximation for the behaviour of a droplet not experiencing any gravitational pull.

The introduction of gravity to this model produced some serious problems in simulation. The sheet mesh would often fail with strange non-physical bumps and ridges would appear in the shape. The spherical cap ansatz is simply non-compatible with a system with gravity. The height profile in this cases looked nonphysical. In order to counter the non-physical height profile, we took off the previous ansatz that raises the liquid to a certain height before optimizing thereby making the liquid start from zero height. It showed some promise since the trend looked physical(the total energy increased as the sheet went to the edge) and the bump vanished. However, we could not raise the system over a certain height volume (>20) without it failing to optimize the system. It also failed with lower mesh sizes (<0.2) as well. We speculated that since the volume increases from to 0 to the max volume, surface evolver is unable to handle the surface variation beyond a threshold final volume. We speculated, that the volume need to be increased in steps.

We found that there is a command in surface evolver 'B' that can also change the volume in gradual step. However, this also didn't solve the problem and caused mesh failures, ridges, bumps. Therefore, to handle this, we came up with new way of implementing the volume

increase called “Volume Iteration”. “Volume iteration” algorithm increases the volume in steps by breaking the total volume from zero to final value at a constant increment. Initially, the surface with the film on it at zero volume is used as input file for energy optimization. This surface is optimized using SE. After SE generates the final mesh output, we extract the vertices, edges and facets of the final zero volume surface to create a new SE input file with the next volume and this process is repeated until the system reaches its final volume.

This gave us physical results that was used in the second chapter of this thesis.

C.6 Height profile study and comparison with the experiment

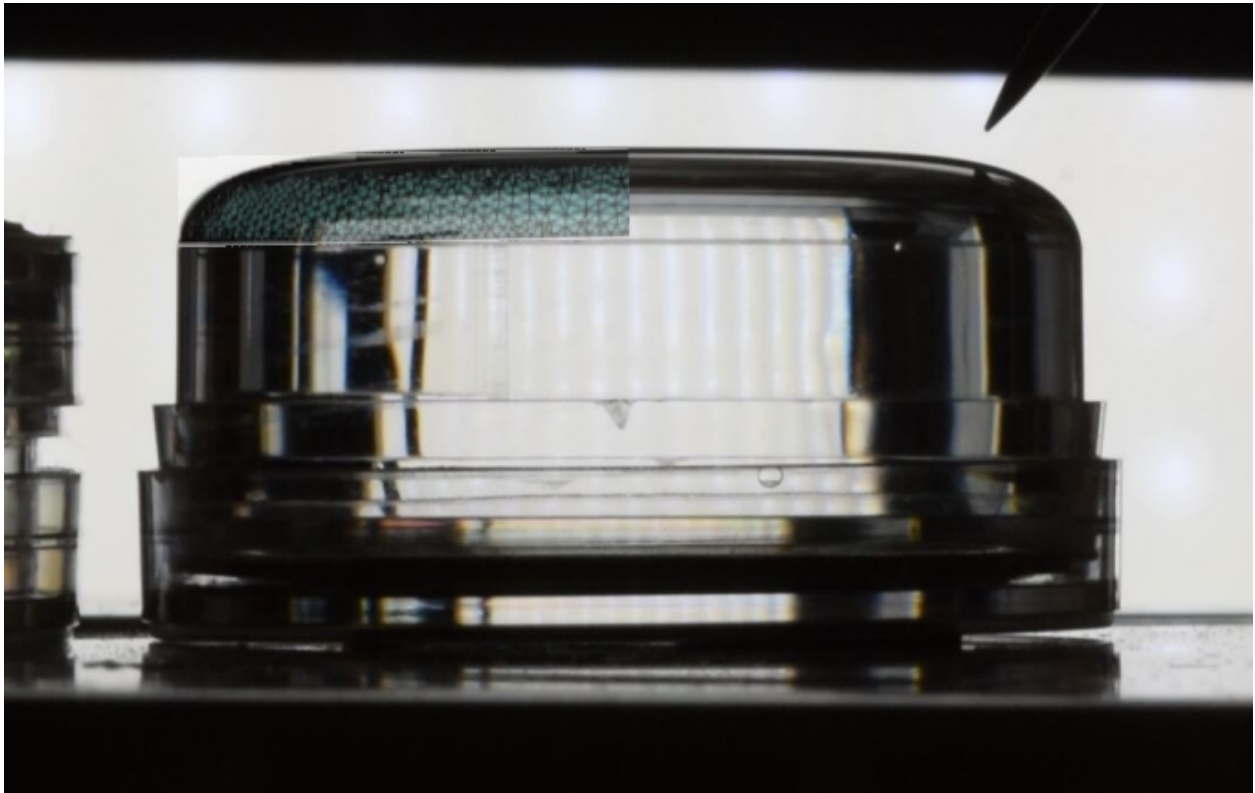


Figure 49: **Height Profile Matching:** Simulating the model with the non-dimensionalized parameters from the experiment and superimposing it on the liquid drop to test qualitative profile matching.

We also performed a qualitative test on the height profile of the liquid to ensure our simulation model is able to create a realistic liquid profile when provided with the experimen-

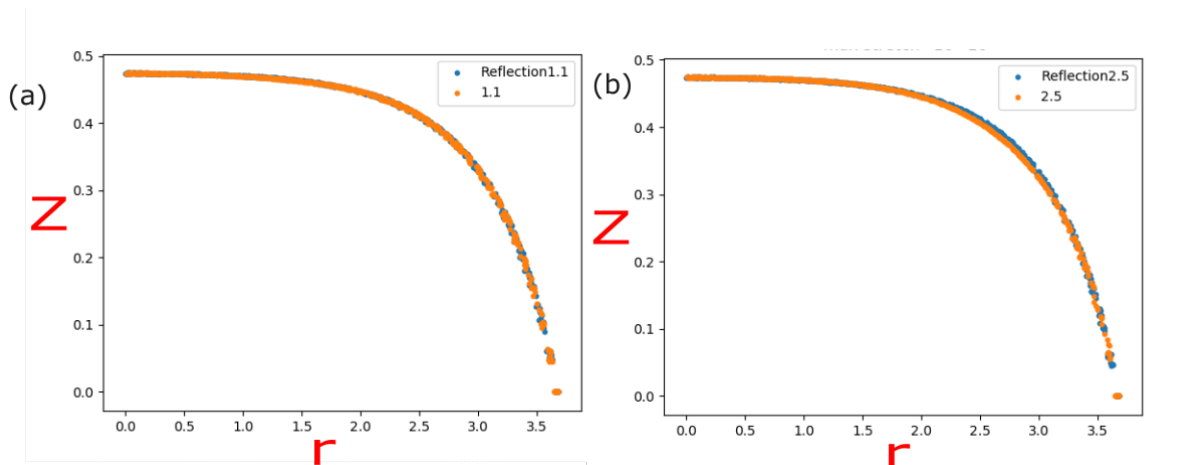


Figure 50: **Height Profile reflection:** The left side of the height profile is reflected on the right side. (a) Height profile when the film is at 1.1 from center. (b) Height profile when the film is at 2.5 from center.

tally derived parameters. Figure 49 confirms that our simulated liquid bath superimposes quite well with the experimental system's side view.

We also made sure that the height profile didn't have any unphysical behaviour when the sheet is placed at different position on the liquid surface. We check that by overlapping the left side of the height profile with the right. Fig. 50 shows that they look physical. We can also see in fig. 50 that as the film is displaced towards the edge, the profile changes due to the increase in curvature mismatch as expected.

References

- [1] K. Garcia, C. Kroenke, and P. Bayly, [Philosophical Transactions of the Royal Society B: Biological Sciences](#) **373**, 20170321 (2018).
- [2] T. Tallinen, J. Y. Chung, F. Rousseau, N. Girard, J. Lefèvre, and L. Mahadevan, [Nature Physics](#) **12**, 588 (2016).
- [3] Robert Kunzig, “[How google’s balloons surprised their creator,](#)” (2021), [Online; accessed November 11, 2022].
- [4] Robert Kunzig, “[The physics of ... wrinkles,](#)” (2003), [Online; accessed November 8, 2022].
- [5] P.-Y. Chen, J. Sodhi, Y. Qiu, T. M. Valentin, R. S. Steinberg, Z. Wang, R. H. Hurt, and I. Y. Wong, [Advanced materials](#) **28**, 3564 (2016).
- [6] E. T. Efaz, M. M. Rhaman, S. A. Imam, K. L. Bashar, F. Kabir, M. E. Mourtaza, S. N. Sakib, and F. A. Mozahid, [Engineering Research Express](#) **3**, 032001 (2021).
- [7] S. Karki, H. Kim, S.-J. Na, D. Shin, K. Jo, and J. Lee, [Asian Journal of Pharmaceutical Sciences](#) **11**, 559 (2016).
- [8] Josie F. Turner, “[The 5 most wrinkly dog breeds,](#)” (2019), [Online; accessed November 8, 2022].
- [9] H. Vandeparre, M. Piñeirua, F. Brau, B. Roman, J. Bico, C. Gay, W. Bao, C. N. Lau, P. M. Reis, and P. Damman, [Physical Review Letters](#) **106** (2011), 10.1103/physrevlett.106.224301.
- [10] E. Cerda and L. Mahadevan, [Physical review letters](#) **90**, 074302 (2003).
- [11] D. Long, W. Li, W. Qiao, J. Miyawaki, S.-H. Yoon, I. Mochida, and L. Ling, [Nanoscale](#) **3**, 3652 (2011).

- [12] Bushnell, [AIAA Journal](#) **19** (1981).
- [13] E. Cerda, S. Chaieb, F. Melo, and L. Mahadevan, [Nature](#) **401**, 46 (1999).
- [14] E. Cerda and L. Mahadevan, [Physical Review Letters](#) **80**, 2358 (1998).
- [15] S. Chaieb, F. Melo, and J.-C. Géminard, [Physical review letters](#) **80**, 2354 (1998).
- [16] T. Liang and T. A. Witten, [Physical Review E](#) **71**, 016612 (2005).
- [17] F. B.-W. Pierre-Gilles Gennes and D. Quéré, [Capillarity and Wetting Phenomena](#) (Springer New York, NY, 2004).
- [18] D. Vella and L. Mahadevan, [American Journal of Physics](#) **73**, 817 (2005).
- [19] Y. Timounay, R. De, J. L. Stelzel, Z. S. Schrecengost, M. M. Ripp, and J. D. Paulsen, [Phys. Rev. X](#) **10**, 021008 (2020).
- [20] H. King, R. D. Schroll, B. Davidovitch, and N. Menon, [Proceedings of the National Academy of Sciences](#) **109**, 9716 (2012).
- [21] H. King, [Open Access Dissertations](#) **692** (2013).
- [22] E. Sharon, B. Roman, M. Marder, G.-S. Shin, and H. L. Swinney, [Nature](#) **419**, 579 (2002).
- [23] Y. Klein, E. Efrati, and E. Sharon, [Science](#) **315**, 1116 (2007).
- [24] J. Gemmer, E. Sharon, T. Shearman, and S. C. Venkataramani, [EPL \(Europhysics Letters\)](#) **114**, 24003 (2016).
- [25] A. Lobkovsky, S. Gentges, H. Li, D. Morse, and T. A. Witten, [Science](#) **270**, 1482 (1995).
- [26] E. Cerda and L. Mahadevan, [Physical Review Letters](#) **80**, 2358 (1998).
- [27] D. L. Blair and A. Kudrolli, [Physical Review Letters](#) **94**, 166107 (2005).

- [28] A. D. Cambou and N. Menon, [Proceedings of the National Academy of Sciences](#) **108**, 14741 (2011).
- [29] J. Rodriguez-Hernandez, [Progress in Polymer Science](#) **42**, 1 (2015).
- [30] Q. Wang and X. Zhao, [MRS Bulletin](#) **41**, 115 (2016).
- [31] T. Tallinen, J. Åström, and J. Timonen, [Nature Materials](#) **8**, 25 (2009).
- [32] B. J. Gurmessa and A. B. Croll, [Physical Review Letters](#) **110**, 074301 (2013).
- [33] O. Gottesman, E. Efrati, and S. M. Rubinstein, [Nature Communications](#) **6** (2015).
- [34] N. Bowden, S. Brittain, A. G. Evans, J. W. Hutchinson, and G. M. Whitesides, [Nature](#) **393**, 146 (1998).
- [35] B. Davidovitch, R. D. Schroll, D. Vella, M. Adda-Bedia, and E. A. Cerda, [Proceedings of the National Academy of Sciences](#) (2011).
- [36] P. Bella and R. V. Kohn, [Phil. Trans. R. Soc. A](#) **375**, 20160157 (2017).
- [37] E. Hohlfeld and B. Davidovitch, [Physical Review E](#) **91**, 012407 (2015).
- [38] D. Vella, J. Huang, N. Menon, T. P. Russell, and B. Davidovitch, [Physical Review Letters](#) **114**, 014301 (2015).
- [39] D. Vella, H. Ebrahimi, A. Vaziri, and B. Davidovitch, [EPL \(Europhysics Letters\)](#) **112**, 24007 (2015).
- [40] J. D. Paulsen, E. Hohlfeld, H. King, J. Huang, Z. Qiu, T. P. Russell, N. Menon, D. Vella, and B. Davidovitch, [Proceedings of the National Academy of Sciences](#) **113**, 1144 (2016).
- [41] B. Davidovitch, Y. Sun, and G. M. Grason, [Proceedings of the National Academy of Sciences](#) **116**, 1483 (2019).
- [42] I. Tobasco, [Archive for Rational Mechanics and Analysis](#) **239**, 1211 (2021).

- [43] E. M. Kramer and T. A. Witten, [Physical Review Letters](#) **78**, 1303 (1997).
- [44] T. A. Witten, [Reviews of Modern Physics](#) **79**, 643 (2007).
- [45] D. Vella, J. Bico, A. Boudaoud, B. Roman, and P. M. Reis, [Proceedings of the National Academy of Sciences](#) **106**, 10901 (2009).
- [46] P. M. Reis, F. Corson, A. Boudaoud, and B. Roman, [Physical Review Letters](#) **103**, 045501 (2009).
- [47] P. Kim, M. Abkarian, and H. A. Stone, [Nature Materials](#) **10**, 952 (2011).
- [48] B. Li, Y.-P. Cao, X.-Q. Feng, and H. Gao, [Soft Matter](#) **8**, 5728 (2012).
- [49] F. Brau, P. Damman, H. Diamant, and T. A. Witten, [Soft Matter](#) **9**, 8177 (2013).
- [50] J. Huang, M. Juszkievicz, W. H. De Jeu, E. Cerda, T. Emrick, N. Menon, and T. P. Russell, [Science](#) **317**, 650 (2007).
- [51] D. Vella and B. Davidovitch, [Physical Review E](#) **98**, 013003 (2018).
- [52] C. A. Schneider, W. S. Rasband, and K. W. Eliceiri, [Nature methods](#) **9**, 671 (2012).
- [53] M. D. Abràmoff, P. J. Magalhães, and S. J. Ram, [Biophotonics international](#) **11**, 36 (2004).
- [54] E. W. Weisstein, (2002).
- [55] W. H. Paulsen, [Am. Math. Mon.](#) **101**, 953 (1994).
- [56] M. A. Deakin, [B. Aust. Math. Soc.](#) **80**, 506 (2009).
- [57] R. Barsotti and S. S. Ligarò, [Comput. Mech.](#) **53**, 1001 (2014).
- [58] R. Vetter, N. Stoop, F. K. Wittel, and H. J. Herrmann, [J. Phys. Conf. Ser.](#) **487**, 012012 (2014).

- [59] E. Siéfert, E. Reyssat, J. Bico, and B. Roman, [Proceedings of the National Academy of Sciences](#) **116**, 16692 (2019).
- [60] A. N. Pressley, *Elementary differential geometry* (Springer Science & Business Media, 2010).
- [61] J. Chopin and A. Kudrolli, [Soft Matter](#) **12**, 4457 (2016).
- [62] S. Chaïeb, F. Melo, and J.-C. Gémard, [Physical Review Letters](#) **80**, 2354 (1998).
- [63] A. Boudaoud, P. Patricio, Y. Couder, and M. B. Amar, [Nature](#) **407**, 718 (2000).
- [64] L. Walsh, R. Meza, and E. Hamm, [Journal of Physics D: Applied Physics](#) **44**, 232002 (2011).
- [65] T. v. Karman, [Journal of the Aeronautical Sciences](#) **8**, 303 (1941).
- [66] E. Viot, T. Kreilos, T. M. Schneider, and S. M. Rubinstein, [Physical review letters](#) **119**, 224101 (2017).
- [67] M. Taffetani and D. Vella, [Philosophical Transactions of the Royal Society A: Mathematical, Physical and Engineering Sciences](#) **375**, 20160330 (2017).
- [68] O. Gottesman, E. Vouga, S. M. Rubinstein, and L. Mahadevan, [EPL \(Europhysics Letters\)](#) **124**, 14005 (2018).
- [69] H. Aharoni, D. V. Todorova, O. Albarrán, L. Goehring, R. D. Kamien, and E. Katifori, [Nature communications](#) **8**, 15809 (2017).
- [70] O. Tovkach, J. Chen, M. M. Ripp, T. Zhang, J. D. Paulsen, and B. Davidovitch, [Proceedings of the National Academy of Sciences](#) (2020).
- [71] W. H. Horton and S. C. Durham, [International Journal of Solids and Structures](#) **1**, 59 (1965).

- [72] K. Seffen and S. Stott, *Journal of Applied Mechanics* **81**, 061001 (2014).
- [73] I. Tobasco, *Communications on Pure and Applied Mathematics* **71**, 304 (2018).
- [74] J. Y. Chung, A. J. Nolte, and C. M. Stafford, *Advanced Materials* **23**, 349 (2011).
- [75] E. P. Chan, E. J. Smith, R. C. Hayward, and A. J. Crosby, *Advanced Materials* **20**, 711 (2008).
- [76] J. Zang, S. Ryu, N. Pugno, Q. Wang, Q. Tu, M. J. Buehler, and X. Zhao, *Nature materials* **12**, 321 (2013).
- [77] K. Khare, J. Zhou, and S. Yang, *Langmuir* **25**, 12794 (2009).
- [78] D. L. Hu and J. W. Bush, *Nature* **437**, 733 (2005).
- [79] G. Xie, P. Li, P. Y. Kim, P.-Y. Gu, B. A. Helms, P. D. Ashby, L. Jiang, and T. P. Russell, *Nature chemistry* **14**, 208—215 (2022).
- [80] Y. Hara, M. Saiki, T. Suzuki, and K. Kikuchi, *Chemistry Letters* **43**, 938 (2014).
- [81] D. Kumar, J. D. Paulsen, T. P. Russell, and N. Menon, *Science* **359**, 775 (2018).
- [82] J. D. Paulsen, V. Démery, C. D. Santangelo, T. P. Russell, B. Davidovitch, and N. Menon, *Nature materials* **14**, 1206 (2015).
- [83] M. F. Reynolds, K. L. McGill, M. A. Wang, H. Gao, F. Mujid, K. Kang, J. Park, M. Z. Miskin, I. Cohen, and P. L. McEuen, *Nano letters* **19**, 6221 (2019).
- [84] J. D. Paulsen, V. Démery, K. B. Toga, Z. Qiu, T. P. Russell, B. Davidovitch, and N. Menon, *Physical Review Letters* **118**, 048004 (2017).
- [85] K. A. Brakke, *Experimental Mathematics* **1**, 141 (1992).
- [86] A. Dörr, S. Hardt, H. Masoud, and H. A. Stone, *Journal of Fluid Mechanics* **790**, 607 (2016).

- [87] J. F. Trahan, [Journal of Fluids Engineering](#) (2006).
- [88] T. Liang, [Physical Review E](#) **77**, 056602 (2008).
- [89] D. Girardeau-Montaut, [“CloudCompare - open source project,”](#) Accessed: 2022-11-8.

D Curriculum Vitae

Raj De

Syracuse NY, 13210

rde101@syr.edu | +1-(315)-949-8690 | [raj-de](#)

Education

- **Ph.D. Physics** 2016-2023
Syracuse University, Syracuse NY, 13210
- **M.S. Applied Physics** 2014-2016
Indian Institute of Technology(IIT), Dhanbad, India
- **B.S. Physics** 2010-2014
University of Calcutta, Kolkata, India

Research Experience

- **Curvature driven propulsion in floating thin film** 2020
Syracuse University, Graduate research, PI: Dr. Joseph Paulsen
 - Applied analytical mesh model optimizing energetic of floating thin film by **gradient descent** method. Applied interface surface triangulation and meshing packages through python and C to implement different soft matter experiments in collaboration with experimental researchers to evaluate the important physical parameters and non-dimensionalize their values from experiments to be implemented in the simulation model to investigate the underlying energetic principle.

- Implemented data fitting techniques using **SciPy** for exponential basis functions. Applied **Multivariate Linear Regression** machine learning model to predict exponents for multiple physical parameters that are varied in the simulation model to determine their influence in varying the energy of the system.

- **Crumples as a Generic Stress-Focusing Instability in Confined Sheets**

2019

Syracuse University, Graduate research, PI: Dr. Joseph Paulsen

- Developed model experiments studying geometric frustration on thin films under tensile stress. Worked at the intersection of experimental and computational projects and optimized data collection techniques.
- 3D modelling of novel structures and preliminary data cleaning and extraction of the point cloud data from the model. Image analysis to extract relevant data for surface topography. Estimation of Gaussian and Mean curvatures by local quadratic surface fitting to point cloud data obtained from the 3D model.

- **Hydrogen Storage in Boron-Based Cluster**

2015-2016

Syracuse University, Graduate research, PI: Dr. Sridhar Sahu

- Investigated the application of Boron Clusters for storage of molecular Hydrogen with quantum mechanical modelling method called Density Functional Theory (DFT) with computations performed in Gaussian software.

- **Mono Disperse Group III (Gallium and Indium) Doped Zinc Oxide and Tin Doped Cadmium Oxide as An Alternative TCO Coating**

2014

Syracuse University, Graduate research, PI: Dr. S. K. De

- Synthesized colloidal nanocrystals by hot injection method and studied the structural variation on varying concentration of the dopant and plasmon resonance.
- Characterized optical and electrical features of nanocrystals by Transmission Electron Microscopy (TEM), Scanning Electron Microscope (SEM), X-Ray Diffraction (XRD), Infrared spectroscopy and UV-Vis absorption .

- **Determination of Magnetic Susceptibility by Quincke’s Method 2013**

Maulana Azad College, Undergraduate Research Project under the supervision of Prof. Babul Kanti Datta, Prof. Subhas Chandra Kar, and Prof. Debashis Sen.

- Determined the magnetic susceptibility for $MnSO_4.H_2O$ salt using Quincke’s method. The mean molar susceptibility of $MnSO_4.H_2O$ salt obtained from this experiment was found comparable with the recently measured value.

Teaching, Mentorship, and Outreach

- **Outreach**

2018-2020

The Society for the Promotion of Indian Classical Music And Culture Amongst Youth

- Organized Classical Indian music and cultural events as President of the Graduate Student Organization.
- Promoted diversity and awareness amongst Syracuse University students and Syracuse Community at large through participating in University wide events like Involvement Fair(2019).

International Festival

- Organized and lead SPICMACAY to represent Indian culture at the First International Festival hosted by Center for International Services. 2019

- **Graduate Mentor**

Syracuse Area High school student

- Mentored student giving first hand research experience through simulating their first computational model. Summer 2022

Research for Undergraduate Mentor

- Mentored an undergraduate working to setup 3D scanner studying topography of crumples. Summer 2019

- **Graduate Teaching Assistant/ Grading Assistant**

Syracuse University

- Quantum Mechanics II Fall 2020
- Solar Energy Science and Architectures Fall 2017
- General Physics Laboratory 2016-2017

Professional and Academic Memberships

- **Bioinspired Graduate and Postdoctoral Development Program** 2019-2022

Syracuse University

- Graduate Participant

- **American Physical Society** 2019-2022

- Student member

Awards & Fellowships

- **Summer Dissertation Fellowship** 2022

Syracuse University

– Graduate Fellow

- **3 Minute Thesis Defense** 2022

Syracuse University

– Finalist

- **Merit Scholarship** 2016

Indian Institute of Technology (Indian School of Mines)

– Graduate student

Publications

R. De, M. Ripp, S. Hejazine, J. Paulsen; *Geometric Incompatibility Drives Thin Floating Film Migration*, in preparation

Y. Timounay, **R. De**, J. Stelzel, Z. Schrecengost, M. Ripp, J. Paulsen; *Crumples as a generic stress-focusing instability in confined sheets*, *Physical Review X*, April 2020

Shubham Dutta, Aranyo Mitra, **Raj De**, Arka Sardar, Sayan Ghosh and Tanmoy Maiti. *Determination of Magnetic Susceptibility by Quincke's Method*, *MAC Science Journal*, Vol. 1, 143-151, 2013

Presentations

Oral

- **R. De**, J. Paulsen; *Turning Sharp Crumples into Smooth Wrinkles in a Mylar Balloon*, Three minute Presentation, Syracuse University, Syracuse, NY 2022

- R. De, M. Ripp, S. Hejazine, J. Paulsen; *Geometry Driven Propulsion of Floating films: Part 2*, American Physical Society: Division of Fluid Dynamics; Phoenix, AZ 2021
- R. De, Y. Timonay, J. Paulsen; *Geometric Stiffening and Stress Focusing in Inflated Membranes: Threshold and Morphology*, American Physical Society: Division of Fluid Dynamics; Boston, MA 2019

Poster

- R. De, J. Paulsen; *The Curvature Driven Propulsion Of Interfacial Films* 2022
Bioinspired Institute Inaugural Annual Symposium, Syracuse, NY
- R. De, S. Hejazine, M. Ripp and J. D. Paulsen; *Simulating the curvature driven propulsion of interfacial films Poster: Stevenson Biomaterials*, Syracuse University, NY 2021
- R. De, Yousra, and Joseph D. Paulsen; *Stress Focusing in Inflated Membranes: Threshold and Morphology*, Bioinspired Institute Kick-off Event, Syracuse, NY 2019

Professional Development

- Summer school on “Soft Solids and Complex fluids”, The University of Massachusetts Amherst, Amherst, Massachusetts, 2019.
- Winter school program on "Condensed Matter Physics", Indian Statistical Institute (ISI), Kolkata, 2016.